Contrast Media & Molecular Imaging

The Application of Functional Imaging in the Diagnosis of Tumors

Lead Guest Editor: Xuelei Ma
Guest Editors: Xiawei Wei and Shasha Li

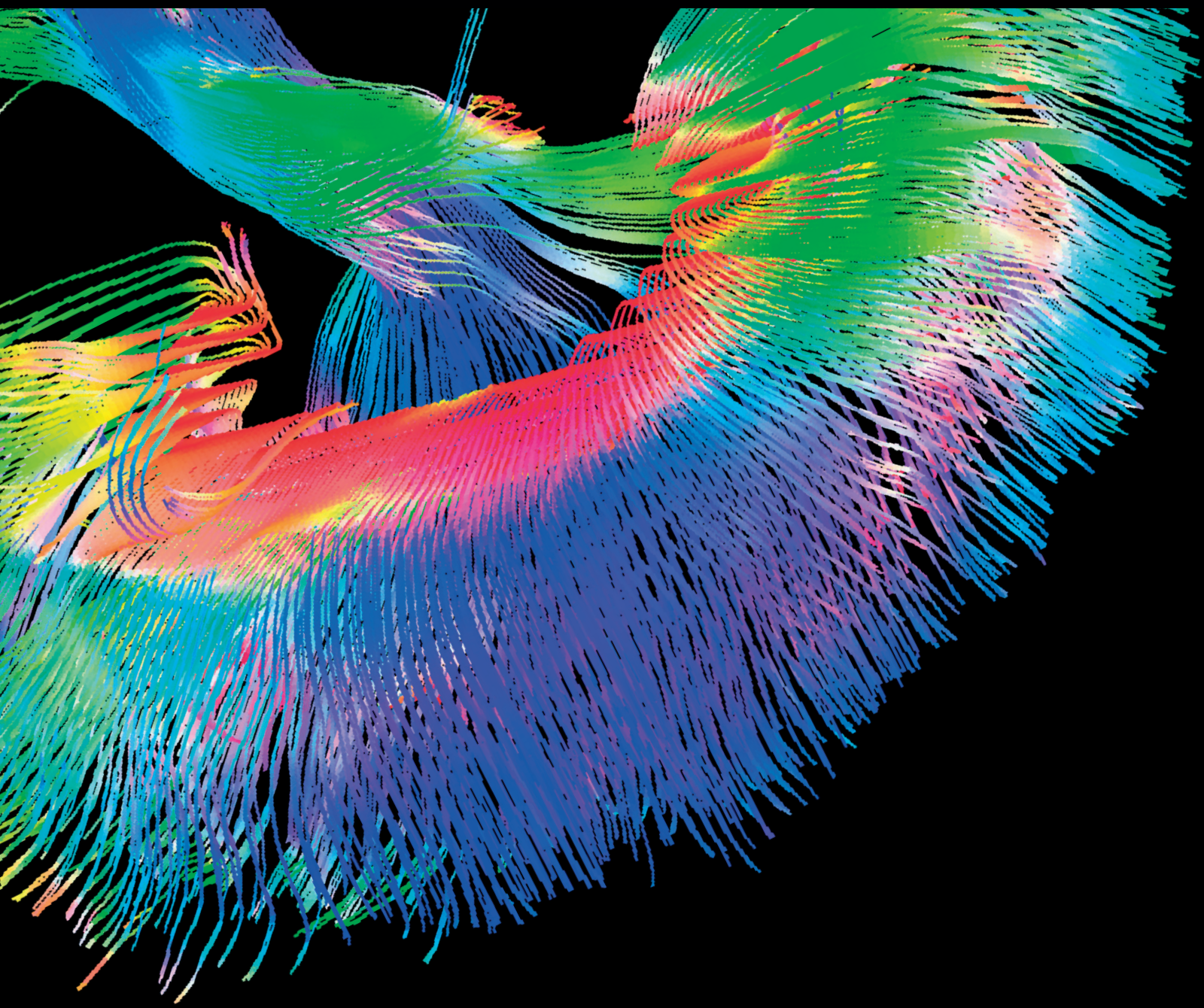

The Application of Functional Imaging in the Diagnosis of Tumors

Contrast Media & Molecular Imaging

The Application of Functional Imaging in the Diagnosis of Tumors

Lead Guest Editor: Xuelei Ma
Guest Editors: Xiawei Wei and Shasha Li

Editorial Board

Contents

Hindawi
Contrast Media & Molecular Imaging
Volume 2017, Article ID 3608912, 1 page
https://doi.org/10.1155/2017/3608912

Editorial

The Application of Functional Imaging in the Diagnosis of Tumors

Xuelei Ma,[1] Xiawei Wei,[2] and Shasha Li[3]

[1]*State Key Laboratory of Biotherapy and Cancer Center, West China Hospital, Sichuan University and Collaborative Innovation Center for Biotherapy, Chengdu, China*
[2]*Lab of Aging Research and Nanotoxicology, State Key Laboratory of Biotherapy and Cancer Center, West China Hospital, Sichuan University, Chengdu, China*
[3]*MGH/HST Athinoula A. Martinos Center for Biomedical Imaging, Massachusetts General Hospital, Harvard Medical School, 149 13th Street, Charlestown, MA 02129, USA*

Correspondence should be addressed to Xuelei Ma; drmaxuelei@gmail.com

Received 21 November 2017; Accepted 21 November 2017; Published 12 December 2017

In this special issue, the studies will give a more detailed description of functional imaging through several characteristic tumors. And the researches will find out more reliable evaluation background and more effectively potential targets through in-depth research on various functional imaging, such as PET/CT, PET/MRI, and ultrasound, which will contribute to the improvement of clinical value of functional imaging.

After long-term research, L. Domachevsky et al. further confirmed that the area under the portal vein was the most reliable site for evaluating the tumor background on PET/MRI. However, considering the range of FDG changes in the studies, the clinical difference in the area under the portal vein was expected to be confirmed.

In terms of nuclear medicine, various types of PET/CT and MRI are widely used in oncology. The review performed by C. L. Wright et al. showed that digital PET can improve the detectability of lesions in both tumor and nonneoplastic diseases and enhance the precision and accuracy of diagnosis and treatment compared with conventional PET.

Specifically, in N. Withofs et al.'s study, the overall detection rate of multiple myeloma by $FPRGD_2$ PET/CT is lower than that of [^{18}F]NaF/[^{18}F]FDG PET/CT, but it might be useful in detecting bone marrow infiltration disease. Therefore, whether there is clinical and prognostic relevance of $FPRGD_2$-positive patients remains to be further researched.

Somatostatin receptor-2- (SSTR2-) positive patients with neuroblastoma showed higher uptake of ^{68}Ga-DOTA-TATE and were more sensitive to ^{177}Lu-DOTA-TATE according to L. Zhang et al.'s research, which makes SSTR2 be a potential therapeutic target of neuroblastoma. D. Spiegelberg and J. Nilvebrant also discussed CD44v6, which is widely expressed in head and neck tumors and plays a similar role to that of SSTR2 in neuroblastoma.

Ultrasound is more widely used in clinical practice. The study by W. Ling et al. further confirmed the diagnostic possibility of rare Xp11 translocation renal cell carcinoma (RCC) by ultrasound. However, the bias due to small samples has to be considered, and we expect that the future studies will compensate for this shortcoming.

Functional imaging can be applied extensively in different types of tumors. Therefore, the continuous exploration and innovation are essential for enhancing clinical values in the future diagnosis and treatment, using either ultrasound or various imaging.

Xuelei Ma
Xiawei Wei
Shasha Li

Hindawi
Contrast Media & Molecular Imaging
Volume 2017, Article ID 2958357, 5 pages
https://doi.org/10.1155/2017/2958357

Research Article

Ultrasonographic Findings of Renal Cell Carcinomas Associated with Xp11.2 Translocation/TFE3 Gene Fusion

Wenwu Ling,[1] Xuelei Ma,[2] Yan Luo,[1] Linyan Chen,[2] Huiyao Wang,[3] Xiaoling Wang,[4] Ni Chen,[5] Hao Zeng,[6] Yongzhong Li,[1] and Diming Cai[1]

[1]*Department of Ultrasound, West China Hospital, Sichuan University, Chengdu, China*
[2]*State Key Laboratory of Biotherapy and Cancer Center, West China Hospital, Sichuan University and Collaborative Innovation Center, Chengdu, China*
[3]*Department of Psychiatry, West China Hospital, Sichuan University, Chengdu, China*
[4]*Department of Operations Management, West China Hospital, Sichuan University, Chengdu, China*
[5]*Department of Pathology, West China Hospital, Sichuan University, Chengdu, China*
[6]*Department of Urology, West China Hospital, Sichuan University, Chengdu, China*

Correspondence should be addressed to Diming Cai; doccai@163.com

Received 25 February 2017; Revised 13 July 2017; Accepted 25 October 2017; Published 23 November 2017

Academic Editor: Anne Roivainen

Objective. This study was to investigate the features of renal carcinomas associated with Xp11.2 translocations/TFE3 gene fusions (Xp11.2-RCC) on conventional ultrasound (US) and contrast-enhanced ultrasound (CEUS). *Methods*. US and CEUS features of twenty-two cases with histopathologically proven Xp11.2-RCC were retrospectively reviewed. *Results*. 22 patients (11 males, 11 females) were included in this study, with a mean age of 28.3 ± 20.4 years. Eight tumors (36.3%, 8/22) were in left kidney, and 14 tumors (63.7%, 14/22) were in right kidney. All tumors (100%, 22/22) were mixed echogenicity type. 13 tumors (59.1%, 13/22) presented small dotted calcifications. The boundary of 14 tumors (63.6%, 14/22) was sharp and the other 8 tumors' (36.4%, 8/22) boundary was blurry. By CEUS, in early phase, the solid element of all tumors showed obvious enhancement. In delayed phase, 13 tumors showed hypoenhancement, seven tumors showed isoenhancement, and 2 tumors showed hyperenhancement. There were irregular nonenhancement areas in all tumors inside. *Conclusions*. By US and CEUS, when children and adolescents were found to have hyperechoic mixed tumor in kidney with sharp margin and calcification, and the tumors showed obvious enhancement and hypoenhancement with irregular nonenhancement areas in the tumor in early phase and delayed phase, respectively, Xp11.2-RCC should be suspected.

1. Introduction

Renal cell carcinoma associated with Xp11.2 translocation/TFE 3 gene fusion (Xp11.2-RCC) is a rare subtype of RCC that is now accepted as a distinct entity according to the 2016 World Health Organization renal tumor classification [1]. In the clinical works, cases of Xp11.2-RCC were found by postoperation of pathology, confirmed now and then. In the literatures, the medical imaging of Xp11.2-RCC was converged by computer tomography (CT) or magnetic resonance imaging (MRI) [2–5]. Xp11.2-RCC is typically presented as asymptomatic, painless renal mass and is often identified accidentally by abdominal imaging [6]. Ultrasound is the most widely used in abdominal examination because it is cheap and convenient with no radiation exposure. But few cases had been diagnosed by US and CEUS in the literatures. Are there any features of Xp11.2-RCC by US and CEUS? We designed this retrospective study to answer the question.

2. Materials and Methods

2.1. Patient Data. This study was conducted in accordance with the declaration of Helsinki. This study was conducted with approval from the Ethics Committee of West China Hospital, Sichuan University. We retrospectively reviewed the results of US and CEUS examination of 22 patients (11 males,

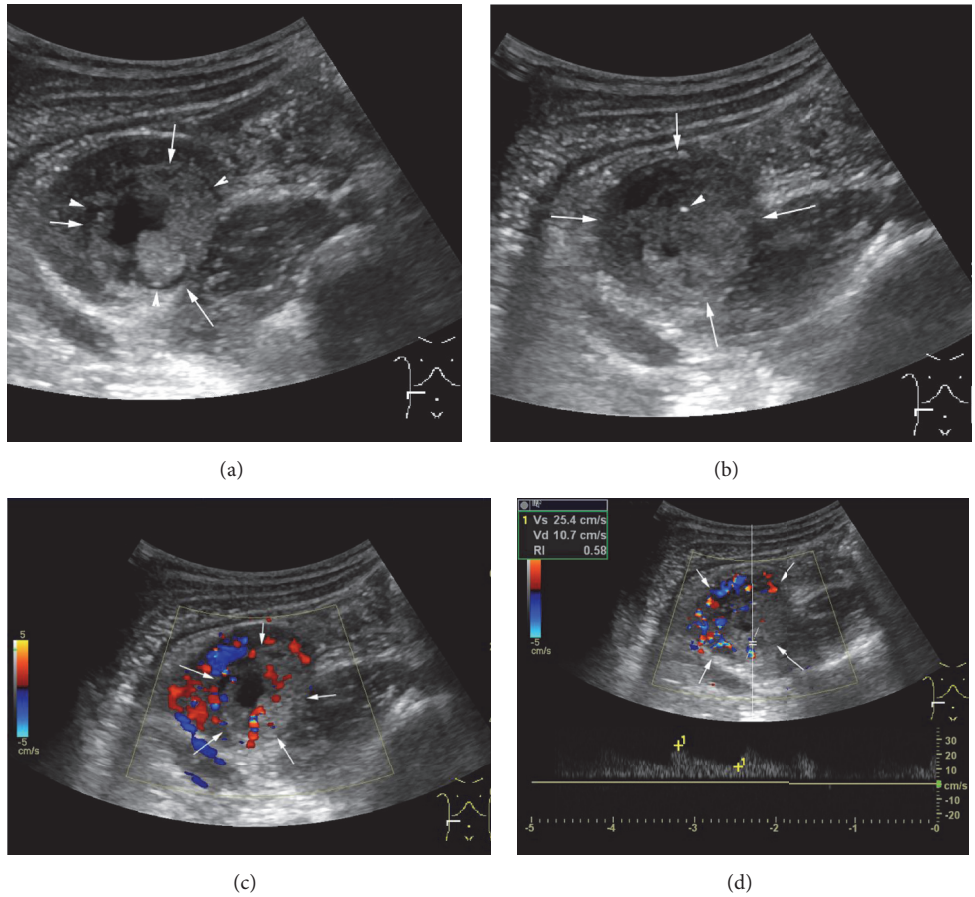

Figure 1: Case 1: male, 12 years old; a hyperechoic mixed mass was found in his right renal of lower part in the renal medulla. (a) Cyst-solid mass with size of 3.2 × 2.1 cm was found (arrow) and an annular hypoechoic halo sign surrounding the tumor was displayed (arrow head). (b) Spot calcification (arrow head) was found inside the tumor (arrow). (c) By CDFI mode, the solid component was found by multibranch threadiness color Doppler signal. (d) By PW mode, the solid component was detected by low blood flow resistance indexes (RI = 0.58).

11 females, mean age: 28.3 ± 20.4 years, range: 6 to 63 years) with 22 tumors of Xp11.2-RCC who were admitted to our hospital between January 2009 and January 2017. And all cases were confirmed by pathology postoperatively. The tumors were diagnosed by pathology not only on morphology itself but also on immunophenotype and molecular genetics findings (fluorescence in situ hybridization, FISH; reverse transcriptase polymerase chain reaction, RT-PCR; or next-generation sequencing, NGS).

2.2. US Examination. US and CEUS were performed with a Philips IU22 scanner (Philips Medical Solutions, Mountain View, CA, USA) with a 1–5-MHz convex transducer or LOGIQ E9 (GE Healthcare, Milwaukee, WI, United States) ultrasound system with a C2–5 MHz probe. The US systems were equipped with harmonic contrast pulse sequencing apparatus. The contrast agent used was SonoVue (BraccoSpa, Milan, Italy) and the suspension contained stabilized sulfur hexafluoride microbubbles. The examinations were performed by two sonologists (Cai DM, Ling WW) who had >5 years of experience in renal CEUS. After conventional US, CEUS was performed. Then, CEUS was started at a low mechanical index (PHILIPS MI: 0.06; GE MI: 0.12). SonoVue suspension (2.4 mL) was administered as a bolus injection through the antecubital vein, followed by a flush with 5 mL saline solution. Each study involved active monitoring of the lesion of interest and surrounding areas in the early phase (range, 0 s to 30 s), late phase (range, 60 s to 120 s), and delayed phase (>120 s).

2.3. Image Analysis. The location, size, shape, boundary, and inner echogenicity of the lesions were observed and recorded by US. The origins of the tumors were evaluated whether they possibly originated from the renal cortex or renal medullary tissue or are indistinct. By CDFI and PW mode, the blood flow was observed and recorded. The renal veins of affected side were evaluated whether there is embolism, even with inferior vena cava (IVC). The enhancement pattern and enhancement level in different phases of CEUS imaging were reviewed. The degree of enhancement was divided into nonenhancement, hypoenhancement, isoenhancement, and hyperenhancement, according to the enhancement level of the lesion compared with that of the surrounding normal renal parenchyma. Contrast enhancement patterns were recorded by two physicians (Cai DM, Ling WW).

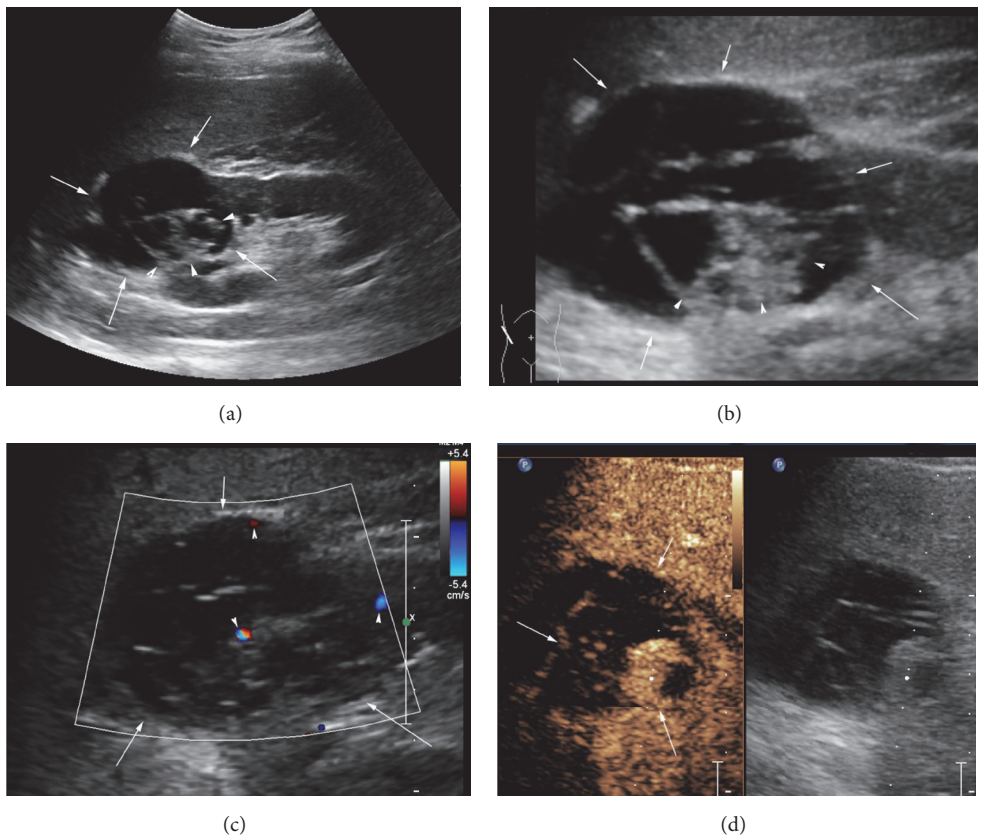

Figure 2: Case 2: male, 48 years old; a multilocular cystic was found in his right renal upper pole. (a) An multilocular cystic with size of 6.0 × 5.1 × 5.8 cm was found (arrow) and irregular thick walls inside the tumor was displayed (arrow head). (b) By partial enlarged view, the multilocular cystic was displayed in detail (arrow) and the irregular thick wall (arrow head). (c) By color Doppler flow imaging (CDFI) mode, the cystic thick walls (arrow), the subcapsular of tumor, and the nodule inside tumor were detected by spot color Doppler signal. (d) By CEUS, the nodule inside the tumor showed hyperenhancement and the thick walls showed isoenhancement in the early phase (arrow).

3. Results

3.1. US Findings. In total, all tumors were found by US. Eight tumors (36.3%, 8/22) were in left kidney and 14 tumors (63.7%, 14/22) were in the right. The range size of the tumors was 2.7 × 2.8 cm–13 × 8 cm. 14 tumors (63.7%, 14/22) were of solid-cyst mixed type, 5 tumors (22.7%, 5/22) were of multilocular cysts, and 3 tumors (13.6%, 3/22) were solid. 13 tumors (59%, 13/22) displayed hyperechogenicity, 6 tumors (18.2%, 6/22) were hypoechoic, and 5 tumors (22.7%, 5/22) were multilocular cystic. 13 tumors (59.1%, 13/22) presented small dotted calcifications. The boundary of 14 tumors (63.6%, 14/22) was sharp and the other 8 tumors' (36.4%, 8/22) boundary was blurry. 13 tumors (59.1%, 13/22) had close relations with renal medulla and the others (40.9%, 9/22) were indistinctive huge tumors of which the origins could not be confirmed. That was to say that renal cortex and renal medulla were all involved in the tumors (Figure 1). Thrombosis was found in the left renal vein in only one case (4.5%, 1/22).

3.2. CEUS Findings. 22 tumors were all detected on CEUS. In early phase (range, 0 s to 30 s), the solid element of the tumors showed obvious enhancement compared to the renal parenchyma. In the late phase (range, 60 s to 120 s), 7 tumors of solid element showed hyperenhancement, 8 tumors showed isoenhancement, and 7 tumors showed hypoenhancement. In delayed phase (>120 s), 13 tumors showed hypoenhancement, 7 tumors showed isoenhancement, and 2 tumors showed hyperenhancement. Irregular areas with no-enhancement and the washout of contrast agents were found in each tumor (Figure 2).

3.3. Pathological Findings. The histopathologic appearance was that the tumor cells were polygonal of a papillary carcinoma with clear cells and cells with granular eosinophilic cytoplasm. These cells displayed nuclear immunoreactivity for TFE3 protein in all 22 cases, which supported the diagnosis of Xp11.2-RCC (Figure 3). To avoid the misdiagnosis, FISH assays were implemented in the tumors. The signals of tumors were split by FISH assays, and all tumors showed positive results.

4. Discussion

Xp11.2-RCC is a rare subtype of RCC that usually affects children and adolescents in reports [1, 7–9]. In our study, 14 patients (63.6%) were younger than 30 years old. It was

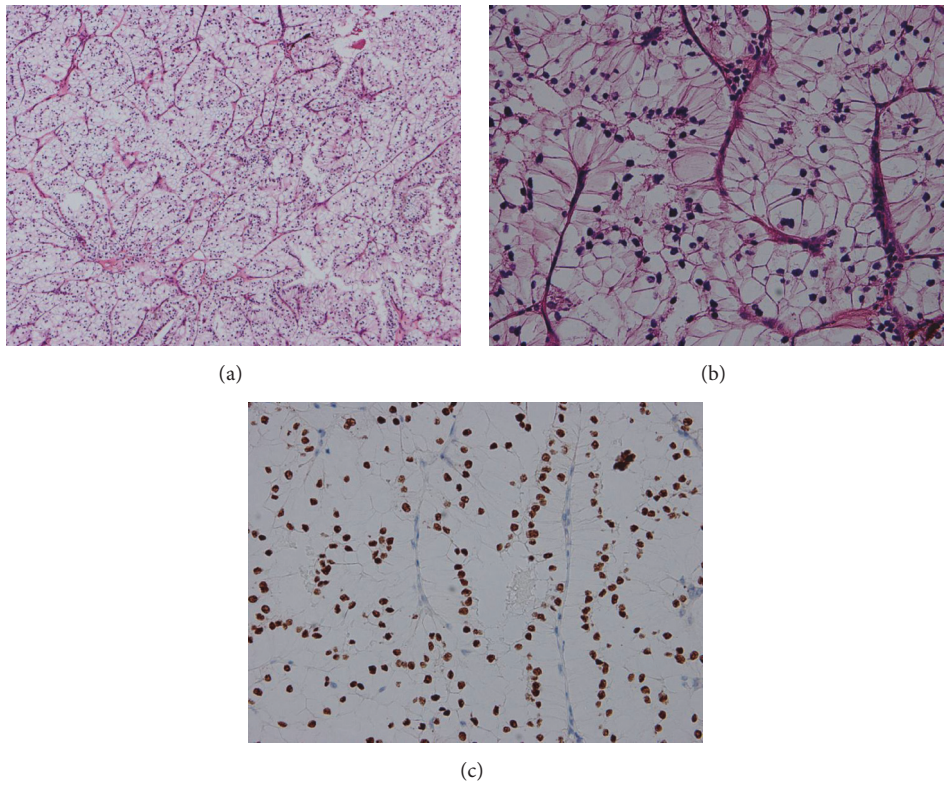

(a) (b)

(c)

Figure 3: Pathological findings. (a) The tumor cells were polygonal of a papillary carcinoma with clear cells and cells with granular eosinophilic cytoplasm (a) (HE staining, 100x magnification) and (b) (HE staining, 400x magnification). (c) The tumor cells in the kidney were visualized by immunohistochemistry staining for TFE3 which revealed positive staining of the nuclei.

consistent with previous reports [10]. In our study, the ratio of males to females was 1 : 1 (11 : 11), consistent with the previous report of no gender difference [11], different from the male predominance reported by Dang et al. [12].

The clinical symptoms of these carcinomas are not clear yet. In our study, the symptoms in 31.8% (7/12) of the patients were nonspecific, and the other 68.2% (15/22) were detected incidentally. Adult-onset Xp11.2-RCC, unlike those with onset during childhood, demonstrated more aggressive clinical courses [13–15]. In our study, 11 cases (50%) were over 20 years old. One adult-onset patient was 61 years old with left renal vein thrombus. A 15-year-old patient, loss of consciousness, was admitted to our emergency department 1 month after nephrectomy. This patient was diagnosed with metastatic renal tumor of spinal canal by CT. And the patient refused further treatment and his prognosis was misadventure.

To date, the imaging features of Xp11.2-RCC by ultrasonography have not been reported and few studies reported its CT or MRI features. Because these tumor cases are very few around the world, we retrospectively analyzed the imaging features by US of Xp11.2-RCC using a relatively large sample. These merits helped to reveal the general imaging features. (1) The tumor may be originated from the proximal or distal nephron. In our study, 13 tumors (59.1%, 13/22) (diameter $\leqslant$ 5 cm) were found in the renal proximal. When it is large, the neoplasm invaded the surrounding tissue and bulged with kidney contours. And this imaging feature was different from the clear cell renal cell carcinoma (CCRCC) which is the most common malignancy in kidney. It is well known that CCRCC originated from the renal cortex tissue. And this character may be a criterion in differential diagnosis between the two tumors by US. (2) Xp11.2-RCC may be cystic-solid mixed mass, with irregular solid and liquid interphase component in the tumor. And in our study, 14 tumors (63.7%, 14/22) were of solid-cyst mixed type, 5 tumors (22.7%, 5/22) were solid, and 3 tumors (13.6%, 3/22) were multilocular cysts where some nodules were found at the internal face of cysts by US. This feature was related to the tumor pathological change, with hemorrhage, necrosis, or cystic changes inside the tumor [16, 17]. (3) Calcification may be found in the internal tumor of Xp11.2-RCC. In our study, punctate calcification was found in 13 internal tumors (59.1%, 13/22). The calcifications were confirmed by pathology. In them, two tumors were spot calcification and the others were irregular. Calcification cannot diagnose the rare malignancy directly, but in the type of RCC, calcification could be found [3]. (4) The tumors may be detected with rich color Doppler signals in the solid component of tumor by CDFI mode. The features of this may be connected with tumor's pathological basis. In previous report, the tissue of solid component in the tumor was found with plenty of blood capillary and arteriovenous shunting [3]. (5) The margins of tumors may be sharp. In our study, 14 (63.6%, 14/22) tumors' margin was sharp by US. The other

margin was blurry. By CEUS mode, 17 (72.3%, 17/22) tumors' margin was sharp. According to the operation records, 17 tumors (72.3%, 17/22) have pseudocapsule which made the resection easy and whole. Because of the pseudocapsule, the tumor's margin was sharp. This was consistent with the literature reported previously in that the pseudocapsules were found in tumor with fibrous connective tissue by pathology [18].

This study had several limitations. Because Xp11.2-RCC is an uncommon RCC subtype, small sample size will lead to selection bias.

As concluded by US, when children and adolescents were found to have hyperechoic mixed tumor in kidney, with sharp margin, close relation with renal medulla, rich CDFI signal, calcification, and Xp11.2-RCC should be suspected. By CEUS, in the early phase when the tumors showed obvious enhancement and in delayed phase when tumors showed hypoenhancement with irregular areas inside the tumor with nonenhancement, Xp11.2-RCC should be suspected.

Conflicts of Interest

The authors declare that there are no conflicts of interest regarding the publication of this paper.

Authors' Contributions

Wenwu Ling and Xuelei Ma contributed equally to this work.

Acknowledgments

This work was supported by the National Natural Science Foundation of China (no. 81501488), Science and Technology Department of Sichuan Province (nos. 2017JY0267 and 2015SZ0142), and Chengdu Science and Technology Bureau (no. 2014-HM01-00021-SF).

References

[1] H. Moch, A. L. Cubilla, P. A. Humphrey, V. E. Reuter, and T. M. Ulbright, "The 2016 WHO classification of tumours of the urinary system and male genital organs—part a: renal, penile, and testicular tumours," *European Urology*, vol. 70, no. 1, pp. 93–105, 2016.

[2] K. Liu, P. Xie, W. Peng, and Z. Zhou, "Renal carcinomas associated with Xp11.2 translocations/TFE3 gene fusions: findings on MRI and computed tomography imaging," *Journal of Magnetic Resonance Imaging*, vol. 40, no. 2, pp. 440–447, 2014.

[3] W. Wang, J. Ding, Y. Li et al., "Magnetic resonance imaging and computed tomography characteristics of renal cell carcinoma associated with Xp11.2 translocation/TFE3 gene fusion," *PLoS ONE*, vol. 9, no. 6, Article ID e99990, 2014.

[4] S. Woo, S. Y. Kim, M. S. Lee et al., "MDCT findings of renal cell carcinoma associated with Xp11.2 translocation and TFE3 gene fusion and papillary renal cell carcinoma," *American Journal of Roentgenology*, vol. 204, no. 3, pp. 542–549, 2015.

[5] J. He, W. Gan, S. Liu, K. Zhou, G. Zhang, and H. Guo, "Dynamic computed tomographic features of adult renal cell carcinoma associated with Xp11.2 translocation/TFE3 gene fusions: comparison with clear cell renal cell carcinoma," *Journal of Computer Assisted Tomography*, vol. 39, no. 5, pp. 730–736, 2015.

[6] P. Ahluwalia, B. Nair, and G. Kumar, "Renal cell carcinoma associated with Xp11.2 translocation/TFE3 gene fusion: a rare case report with review of the literature," *Case Reports in Urology*, vol. 2013, Article ID 810590, 4 pages, 2013.

[7] P. Argani and M. Ladanyi, "The evolving story of renal translocation carcinomas," *American Journal of Clinical Pathology*, vol. 126, no. 3, pp. 332–334, 2006.

[8] P. Argani and M. Ladanyi, "Translocation carcinomas of the kidney," *Clinics in Laboratory Medicine*, vol. 25, no. 2, pp. 363–378, 2005.

[9] P. Argani, M. Laé, B. Hutchinson et al., "Renal carcinomas with the t(6;11)(p21;q12): clinicopathologic features and demonstration of the specific alpha-TFEB gene fusion by immunohistochemistry, RT-PCR, and DNA PCR," *The American Journal of Surgical Pathology*, vol. 29, no. 2, pp. 230–240, 2005.

[10] Q. Rao, J.-Y. Chen, J.-D. Wang et al., "Renal cell carcinoma in children and young adults: Clinicopathological, immunohistochemical, and VHL gene analysis of 46 cases with follow-up," *International Journal of Surgical Pathology*, vol. 19, no. 2, pp. 170–179, 2011.

[11] A. Wu, L. P. Kunju, L. Cheng, and R. B. Shah, "Renal cell carcinoma in children and young adults: analysis of clinicopathological, immunohistochemical and molecular characteristics with an emphasis on the spectrum of Xp11.2 translocation-associated and unusual clear cell subtypes," *Histopathology*, vol. 53, no. 5, pp. 533–544, 2008.

[12] T. T. Dang, E. Ziv, S. Weinstein, M. V. Meng, Z. Wang, and F. V. Coakley, "Computed tomography and magnetic resonance imaging of adult renal cell carcinoma associated with Xp11.2 translocation," *Journal of Computer Assisted Tomography*, vol. 36, no. 6, pp. 669–674, 2012.

[13] N. Kuroda, M. Tamura, Y. Tanaka et al., "Adult-onset renal cell carcinoma associated with Xp11.2 translocations/TFE3 gene fusion with smooth muscle stroma and abnormal vessels," *Pathology International*, vol. 59, no. 7, pp. 486–491, 2009.

[14] P. Argani, S. Olgac, S. K. Tickoo et al., "Xp11 Translocation renal cell carcinoma in adults: expanded clinical, pathologic, and genetic spectrum," *The American Journal of Surgical Pathology*, vol. 31, no. 8, pp. 1149–1160, 2007.

[15] T. Aoyagi, N. Shinohara, K. Kubota-Chikai, N. Kuroda, and K. Nonomura, "Long-term survival in a patient with node-positive adult-onset Xp11.2 translocation renal cell carcinoma," *Urologia Internationalis*, vol. 86, no. 4, pp. 487–490, 2011.

[16] G. Altinok, M. M. Kattar, A. Mohamed, J. Poulik, D. Grignon, and R. Rabah, "Pediatric renal carcinoma associated with Xp11.2 translocations/TFE3 gene fusions and clinicopathologic associations," *Pediatric and Developmental Pathology*, vol. 8, no. 2, pp. 168–180, 2005.

[17] H. B. Armah and A. V. Parwani, "Xp11.2 translocation renal cell carcinoma," *Archives of Pathology & Laboratory Medicine*, vol. 134, no. 1, pp. 124–129, 2010.

[18] X. M. Cheng, J. He, W. D. Gan et al., "Pseudocapsule of renal cell carcinoma associated with Xp11.2 translocation/TFE3 gene fusion: A clue for tumor enucleation?" *Int J Clin Exp Pathol*, vol. 8, no. 5, pp. 5403–5410, 2015.

Hindawi
Contrast Media & Molecular Imaging
Volume 2017, Article ID 9481276, 10 pages
https://doi.org/10.1155/2017/9481276

Research Article

Correlation of Somatostatin Receptor-2 Expression with Gallium-68-DOTA-TATE Uptake in Neuroblastoma Xenograft Models

Libo Zhang,[1] Douglass C. Vines,[2] Deborah A. Scollard,[2] Trevor McKee,[2] Teesha Komal,[2] Milan Ganguly,[2] Trevor Do,[2] Bing Wu,[1] Natasha Alexander,[1] Reza Vali,[1] Amer Shammas,[1] Travis Besanger,[3] and Sylvain Baruchel[1]

[1]*The Hospital for Sick Children, Toronto, ON, Canada*
[2]*The STTARR Innovation Centre, University Health Network, Toronto, ON, Canada*
[3]*The Center for Probe Development and Commercialization, Hamilton, ON, Canada*

Correspondence should be addressed to Sylvain Baruchel; sylvain.baruchel@sickkids.ca

Received 1 March 2017; Revised 18 June 2017; Accepted 9 July 2017; Published 8 August 2017

Academic Editor: Xuelei Ma

Peptide-receptor imaging and therapy with radiolabeled somatostatin analogs such as ^{68}Ga-DOTA-TATE and ^{177}Lu-DOTA-TATE have become an effective treatment option for SSTR-positive neuroendocrine tumors. The purpose of this study was to evaluate the correlation of somatostatin receptor-2 (SSTR2) expression with ^{68}Ga-DOTA-TATE uptake and ^{177}Lu-DOTA-TATE therapy in neuroblastoma (NB) xenograft models. We demonstrated variable SSTR2 expression profiles in eight NB cell lines. From micro-PET imaging and autoradiography, a higher uptake of ^{68}Ga-DOTA-TATE was observed in SSTR2 high-expressing NB xenografts (CHLA-15) compared to SSTR2 low-expressing NB xenografts (SK-N-BE(2)). Combined autoradiography-immunohistochemistry revealed histological colocalization of SSTR2 and ^{68}Ga-DOTA-TATE uptake in CHLA-15 tumors. With a low dose of ^{177}Lu-DOTA-TATE (20 MBq/animal), tumor growth inhibition was achieved in the CHLA-15 high SSTR2 expressing xenograft model. Although, *in vitro*, NB cells showed variable expression levels of norepinephrine transporter (NET), a molecular target for ^{131}I-MIBG therapy, low ^{123}I-MIBG uptake was observed in all selected NB xenografts. In conclusion, SSTR2 expression levels are associated with ^{68}Ga-DOTA-TATE uptake and antitumor efficacy of ^{177}Lu-DOTA-TATE. ^{68}Ga-DOTA-TATE PET is superior to ^{123}I-MIBG SPECT imaging in detecting NB tumors in our model. Radiolabeled DOTA-TATE can be used as an agent for NB tumor imaging to potentially discriminate tumors eligible for ^{177}Lu-DOTA-TATE therapy.

1. Introduction

Neuroblastoma (NB) is the most common extracranial childhood malignancy, responsible for 15% of all childhood cancer deaths [1]. Despite intensive treatment protocols including multimodal therapy with hematopoietic stem cell transplantation and immunotherapy, three-year disease-free survival is only about 60% for metastatic disease compared to 95% for localized tumors [2, 3].

Somatostatin receptors (SSTRs) are expressed at relatively low levels in most organs. They are moderately expressed in the brain, gastrointestinal tract, pancreas, kidney, and spleen. In contrast, SSTRs, especially SSTR2, have been shown to be highly expressed in various human tumors including pancreatic, small cell lung, and carcinoid tumors, as well as paraganglioma, pheochromocytoma, and neuroblastoma [4]. Georgantzi et al. demonstrated variable frequencies of somatostatin receptor (SSTR1-5) expression in 5 NB cell lines and 11 NB patient tumor biopsy samples [5], making molecular imaging and radionuclide therapy with somatostatin-based nuclear probes an attractive therapeutic option in appropriately selected patient populations [6].

DOTA-TATE is the somatostatin (cyclic peptide hormone) analog of Tyr3-octreotate (TATE) coupled with the

macrocyclic chelator 1,4,7,10-tetraazacyclododecane,1,4,7,10-tetraacetic acid (DOTA). DOTA-TATE is SSTR2 selective with a higher SSTR2 affinity (~0.2 nM) *in vitro* comparing to two other commonly used somatostatin analogs [^{68}Ga-DOTA^{0}-Tyr^{3}]octreotide (DOTA-TOC) and [DOTA^{0}, 1NaI^{3}]octreotide (DOTA-NOC) [7]. Peptide-receptor imaging and therapy with radiolabeled somatostatin analogs are an established and effective treatment option for adult patients with SSTR-positive neuroendocrine tumors [4]. DOTA-TOC and DOTA-TATE can also be radiolabeled with ^{90}Y or ^{177}Lu for targeted β^{-}-particle radionuclide therapy of neuroendocrine tumors. In a recent phase I trial, the safety and efficacy of ^{90}Y-DOTA-TOC therapy were demonstrated in 17 children and young adults with refractory SSTR-positive neuroendocrine tumors including NB [8]. The first study of ^{177}Lu-DOTA-TATE treatment in 35 patients with gastroenteropancreatic neuroendocrine tumors was published in 2003 where an objective response of 38% was achieved [9]. In a 2008 evaluation of 310 adult patients with neuroendocrine tumors, an overall response of 30% was reported [10]. More recently, a pilot clinical study demonstrated that ^{68}Ga-DOTA-TATE PET could be used to image children with relapsed or primary refractory high-risk NB, and ^{68}Ga-DOTA-TATE PET could be used to identify potential candidates for ^{177}Lu-DOTA-TATE treatment [11]. In this study, 6 out of 8 children demonstrated high uptake of ^{68}Ga-DOTA-TATE and proceeded to treatment. Patients received 2 or 3 administrations of ^{177}Lu-DOTA-TATE (0.3 GBq/kg; 8.1 mCi/kg per dose) at a median interval of 9 weeks and a median administered activity of 7.3 GBq. Five of these patients had the stable disease as assessed using the Response Evaluation Criteria in Solid Tumors (RECIST). This study, while limited in the number of patients studied, provided proof-of-principle that children with NB can be imaged and treated with somatostatin receptor-targeted agents. More interestingly, this study demonstrated that 1 patient (out of a series of 6 patients) whose disease was negative for ^{123}I-MIBG nevertheless demonstrated marked uptake of ^{68}Ga-DOTA-TATE.

The primary purpose of this study is to evaluate the uptake of ^{68}Ga-DOTA-TATE in NB xenograft models and correlate this uptake with the expression levels of SSTR2 and, therefore, identify biomarkers which can predict the therapeutic effects of ^{177}Lu-DOTA-TATE.

2. Materials and Methods

2.1. Materials and Reagents. Gallium-68 and lutetium-177 radiolabeled DOTA-TATE were supplied by the Centre for Probe Development and Commercialization (CPDC, Hamilton, ON, Canada). ^{68}Ga-DOTA-TATE was produced with the specific activity of 41.2 ± 9.9 GBq/μmol and with the radiochemical purity of >97% at all cases. NET antibody (NET17-1) was purchased from MAb Technologies (Stone Mountain, GA), and SSTR2 antibody (ab134152) was obtained from Abcam (Cambridge, MA). Triton X-100, ethylenediaminetetraacetic acid (EDTA), and sodium dodecyl sulfate (SDS) were purchased from Sigma Chemical Company (St Louis, MO).

2.2. Cells and Cell Culture. Eight NB cell lines (NUB-7, SK-N-BE(2), BE(2)C, LAN-5, SH-SY5Y, CHLA-15, CHLA-20, and CHLA-90) were selected to represent a panel of cell lines with different biological and genetic backgrounds of NB (Table 1). NUB-7, LAN-5, SK-N-BE(2), BE(2)C, and SH-SY5Y neuroblastoma cells were kindly provided by Dr. Herman Yeger (The Hospital for Sick Children, Toronto, ON, Canada). CHLA-15, CHLA-20, and CHLA-90 were obtained from the Children's Oncology Group Cell Culture and Xenograft Repository (http://www.cogcell.org/) under a signed and approved Material Transfer Agreement. Cell line authentication was performed using short tandem repeats (STR) DNA profiling (Promega's GenePrint® 10 System) [12] conducted by the Genetic Analysis Facility at the Centre for Applied Genomics of The Hospital for Sick Children. The DNA (STR) profile for all cell lines was matched to the profile listed in the Children's Oncology Group (COG) STR Database (http://strdb.cogcell.org/). CHLA-15, CHLA-20, and CHLA-90 neuroblastoma cells were cultured in Iscove's modified Dulbecco's medium supplemented with 3 mM L-glutamine, 5 μg/mL insulin, 5 μg/mL transferrin, and 5 ng/mL selenous acid (ITS Culture Supplement; Collaborative Biomedical Products, Bedford, MA) and 20% fetal bovine serum (FBS). NUB-7, LAN-5, SK-N-BE(2), BE(2)C, and SH-SY5Y neuroblastoma cells were cultured in α-MEM supplemented with 10% FBS.

2.3. RT-PCR. Total cellular RNA was prepared using Qiagen RNeasy mini kit (Qiagen, Valencia, CA) according to the manufacturers' instruction. Residual DNA was eliminated using the Qiagen RNase-Free DNase Set. cDNAs were synthesized from 2 μg of RNA with the Superscript II™ Reverse Transcriptase (Invitrogen). PCR was performed using 1 μL of cDNA in the PCR buffer supplemented with 0.2 mM of dNTP, 2.5 units of Taq polymerase (Biorad and ThermoFisher Scientific), and 0.5 μM of each sense and antisense primer. The following primers were used: SSTR2 forward 5′-GGTGAAGTCCTCTGGAATCC-3′ and reverse 5′-CCATTGCCAGTAGACAGAGC-3′; NET forward 5′-CTCAAGGAGGCCACGGTATGGATCG-3′ and reverse 5′-ACCTGGAAGTCATCAGCCAGTCCGG-3′; GAPDH forward 5′-CTGTCCAGTTAATTTCTGACC-3′ and reverse 5′-CTTTGTACATGGTATTCACCAC-3′. PCR products were run on a 1.5% agarose (Invitrogen) with a 100 bp marker (Thermo Fisher Scientific) and stained with ethidium bromide. Gel pictures were taken using the AlphaImager™ 2200 (Alpha Innotech, Kasendorf, Germany).

2.4. Western Blot. The protein lysates were analyzed by Western blot for SSTR2 and norepinephrine transporter (NET). Briefly, cells were lysed in lysis buffer and denatured. Samples were separated using 10% Bis-Tris precast gels (Invitrogen), followed by transfer to a PDVF membrane. After blocking, all membranes were incubated overnight at 4°C in TBST (Tris-buffered saline, 0.1% Tween 20) buffer containing the primary antibodies. Primary antibody complexes were then detected

Table 1: Neuroblastoma cell lines used in this study.

Cell line	Site	Stage	Patient age	Phase of therapy	MYCN amp	p53 mutant
CHLA-15	Tumor	4	>1	DX	N	WT
CHLA-20	Tumor	4	1.5	PD-Ind	N	WT
CHLA-90	BM	4	8.5	PD-Auto-BMT	N	Mut
LAN-5	BM	Unknown	0.4	Unknown	A	WT
NUB-7	LN	4s/4	0.7	Unknown	A	WT
SH-SY5Y	BM	4	4	PD-Ind	N	WT
BE(2)C	BM	4	2.2	PD-Ind	A	Mut
SK-N-BE(2)	BM	4	2.2	PD-Ind	A	Mut

BM = bone marrow; B = bone; L = liver; P = pulmonary; LN = lymph node; DX = at diagnosis; PD-Ind = progressive disease on induction chemotherapy; BMT = bone marrow transplantation; PD-Auto-BMT = relapsed after myeloablative chemo-radiotherapy followed by bone marrow transplantation; WT =wild type; Mut = mutant; N = nonamplified; A = amplified.

using horseradish peroxidase- (HRP-) conjugated secondary antibodies. Protein bands were revealed with SuperSignal™ West Pico Chemiluminescent Substrate (Thermo Fisher Scientific). NET protein expression in CHLA-15, SK-N-BE(2), and BE(2)C xenografts was quantified densitometrically using ImageJ software (NIH, USA) and normalized with respect to the corresponding expression of β-actin.

2.5. Tissue Preparation for Western Blot. Xenograft tumors were snap frozen in liquid nitrogen immediately after harvesting and stored at −80°C until ready for processing. Tumor tissue samples were homogenized in a RIPA buffer (150 mM NaCl, 50 mM Tris-HCl, 0.5 mM EDTA, 1% Triton X-100, and 0.1% SDS) plus complete protease inhibitor cocktail (Complete Protease Inhibitor Tablets; Boehringer Mannheim, Ingelheim am Rhein, Germany). Homogenates were then centrifuged at 100,000 ×g for 45 minutes at 4°C. The supernatants were assayed for protein content, aliquoted, and stored at −80°C. 25 μg of lysate was subjected to future protein analysis by SDS-PAGE and Western blot analysis.

2.6. Mouse Xenograft Models. All animal studies were approved by Animal Care Committee at the Hospital for Sick Children and at the University Health Network (Toronto, ON, Canada). Four- to 6-week-old, female, nonobese diabetic, severe combined immunodeficiency (NOD/SCID) mice were purchased from Jackson Laboratory (Bar Harbor, ME). CHLA-15, SK-N-BE(2) and BE(2)C cells were used to establish murine models. Briefly, tumor cells were washed three times with Hanks' Balanced Salt Solution (HBSS) before injection. Cell suspensions were mixed 1 : 1 with Growth Factor Reduced Matrigel Matrix (BD Bioscience, Mississauga, ON, Canada). Subcutaneous xenografts were developed by injecting 1×10^6 tumor cells subcutaneously into the dorsal upper flank of NOD/SCID mice.

2.7. Micro-PET/CT Mouse Imaging. Animals were prepared for imaging such that when the tumor xenografts reach a diameter of approximately 1 cm, the mice were anesthetized with 2% isoflurane in the medical air (1.0 L/min) and injected intravenously (IV) via the tail vein [13] with 11.7 MBq ± 2.5 MBq of ^{68}Ga-DOTA-TATE. Images were acquired on a Focus 220 micro-PET scanner (Siemens Preclinical Solutions, Knoxville, TN) at 1 hour after injection using a Minerve imaging bed (Esternay, France) to maintain body temperature at 37°C. Images were reconstructed in a 256 × 256 matrix and a zoom of 6.5 using an ordered subset expectation maximization (OSEM), followed by a maximum a posteriori probability reconstruction algorithm with no attenuation correction. Quantification was performed by volume-of-interest (VOI) analysis using Inveon Research Workplace (IRW) software (Siemens). Tumor volume was obtained by summing multiple 2-dimensional regions of interest from consecutive tomographic planes encompassing the entire tumor volume on fused PET-CT slices. Tumor uptake was expressed as the mean ± SD percentage injected dose per gram (%ID/g).

Immediately after small-animal PET, the Minerve imaging bed with the mouse was transferred to an eXplore Locus Ultra Preclinical CT scanner (GE Healthcare, London, ON, Canada). The micro-CT scan of the mouse was acquired with routine acquisition parameters (80 kV, 70 mA, 16 sec per rotation). PET and CT images were coregistered using IRW software. The micro-CT scan was used for anatomic referencing and for delineating the aforementioned VOIs.

To verify the accuracy of %ID values, a 10 mL specimen of ^{68}Ga with known radioactivity was scanned on the micro-PET. The image-derived concentration was compared with the concentration calculated from the same radioactivity measured by the radioisotope dose calibrator (Model CRC® -15R, Capintec Inc., Ramsay, NJ). The difference in the two concentrations was less than 10%.

2.8. ^{123}I-MIBG SPECT/CT Imaging. 1×10^6 NB tumor cells were injected subcutaneously into the shoulder area of NOD/SCID mice. When tumor xenografts grew to an approximate diameter of 1 cm or more, each mouse was injected with 17.5 MBq ± 2.3 MBq of ^{123}I-MIBG into a lateral tail vein. Five to six hours after injection, both CT and SPECT imaging were performed using a preclinical nanoSPECT/CT system (Bioscan, Washington, DC). For imaging, mice were anesthetized with 1.5% isoflurane and medical air at 1.0 L/min. For anatomical reference, the cone-beam CT scan was acquired first at 45 kVp and 177 μA. Image slices were reconstructed in a 176 × 176 matrix with a fast filtered

back-projection algorithm using InVivoScope® 1.43 software (Bioscan, USA).

For the SPECT scan, a 20% window was set around the 159 keV principal gamma-photon of I-123. In this multiplexed multipinhole SPECT system, the 1.4 mm nine-pinhole mouse "standard" collimators were attached to each of the four detector heads consisting of NaI(Tl) crystals. Photons were acquired for about 150 s/projection and 24 projections per detector head in a 256 × 256 matrix for a total imaging time ranging from 60 to 75 minutes. SPECT data were reconstructed by ordered subset expectation maximization (OSEM) methods with four subsets of data undergoing 9 iterations each using InVivoScope® 1.43. The CT and SPECT slices were then coregistered. Image analysis and volume-of-interest (VOI) quantification were performed using VivoQuant® 2.5 (Mediso/inviCRO, Boston, MA). The activity concentration in the VOI for the whole tumor was divided by the activity concentration in the VOI for the hind limb muscle in order to calculate the tumor-to-muscle ratio (T/M).

2.9. Autoradiography. After the ^{68}Ga-DOTA-TATE PET/CT and ^{123}I-MIBG SPECT/CT studies, CHLA-15, SK-N-BE(2), and BE(2)C xenografts were harvested, cut in half, embedded in Tissue-Tek® optimum cutting temperature (OCT) compound (Tissue-Tek, Sakura, Torrance, CA), along with a piece of forelimb muscle as control, and frozen on liquid nitrogen vapor. Frozen blocks were transferred to the STTARR correlative pathology lab on dry ice, and serial frozen sections of alternating 5 μm (for immunohistochemistry) and 50 μm thickness (for autoradiography) were cut, placed on glass slides, and left to dry for 20 minutes. After sections were completely dry, the 50 μm sections were placed in a custom-built 16-slide holder that held the frozen sections in close proximity to a storage phosphor screen (Cyclone Plus Storage Phosphor System, Perkin Elmer, Shelton, CT, USA), with a layer of plastic wrap separating them. In some instances, a piece of filter paper with serial dilutions of radiotracer was included in the cassette for use as a standard and to check the linearity of the film. This cassette was maintained at −20°C for a period of time equating to 10 half-lives of activity. The timing of tumor resection and contact with phosphor screen were recorded for all cases. Following completion of 10 half-lives of decay, the phosphor screen was removed from the cassette and developed on the Cyclone Plus imaging system at 600 dpi resolution, with a written record of slide locations on the screen. Image quantification was performed in ImageJ software, in which regions of interest (ROIs) were drawn around each tumor and corresponding piece of muscle tissue, and mean phosphor intensity was recorded in each region. A ROI corresponding to background signal was also recorded, taken from the region of screen not containing any slides or tissue. Mean tumor-to-muscle ratios were calculated by division of mean per-pixel intensity in tumor (subtracting background) divided by mean per-pixel muscle intensity, subtracting background.

2.10. SSTR2 Immunohistochemistry. SSTR2 immunofluorescence staining was performed on 5 μm thick frozen sections. Tissue sections were fixed for 10 minutes in acetone and allowed to air dry for 5 minutes. Endogenous biotin, biotin receptors, and avidin sites were blocked with the Avidin/Biotin Blocking Kit (SP-2001, Vector Laboratories, Burlingame, CA). The tissue sections were incubated with rabbit anti-SSTR2 antibody (1 : 100; ab9550, Abcam) for 1 hour at room temperature. Detection of the rabbit antibodies was performed by incubation with Texas Red goat anti-rabbit IgG antibody (1 : 200; TI-1000, Vector Laboratories) for 30 minutes. For the positive control of SSTR immunohistochemistry, normal pancreas islets were used. Negative controls were done by omitting the specific primary antibodies and processed in the same way. The tissue sections were washed and then mounted with Vectashield mounting medium with DAPI (H-1200, Vector Laboratories). Whole-slide scanned immunofluorescence images were acquired on a TissueScope 4000 (Huron Technologies, Waterloo ON, Canada) at 1 μm/pixel resolution. Coregistration of autoradiography with immunofluorescence was performed by upsampling the autoradiography image (600 dpi, which equates to 42 μm/pixel resolution) of the 50 μm adjacent section to match the immunofluorescence image (imaged at 1 μm/pixel resolution), followed by rigid registration using a customized MATLAB script.

2.11. In Vivo Treatment with ^{177}Lu-DOTA-TATE. Drug treatment commenced when the tumor sizes reached 0.5 cm in diameter. Animals were randomized into two groups, each with 7 animals: the control group and the ^{177}Lu-DOTA-TATE treatment group. A single dose of ^{177}Lu-DOTA-TATE (20 MBq) [14] was administered as treatment. Control mice received the same volume of saline. Tumor growth was monitored by measuring tumor dimensions using a digital caliper. Tumor volume was calculated as $\text{width}^2 \times \text{length} \times 0.5$. When tumor volume reached 3 cm^3, mice were sacrificed, and tumors were dissected and weighed. Tumor growth curves consisting of the tumor volumes at different time points were plotted. During the study, the mice were observed daily for possible adverse effects due to treatments. Morbidity signs of ill health such as ruffled/thinning fur, abnormal behaviors, or local erosion from the tumor, were observed. Animal body weight was also monitored for general toxicity.

2.12. Statistical Analysis. Data from different experiments were presented as mean ± SD. Two-tailed, unpaired Student's t-tests were performed to compare the uptake values obtained from SPECT/CT imaging and tumor growth in two different groups. T/M ratios of ^{123}I-MIBG uptake and of ^{123}I-MIBG autoradiography in different groups were analyzed by one-way analysis of variance (ANOVA) and Tukey's test. Comparison of NET expression between different groups was analyzed by the nonparametric Kruskal-Wallis test with Dunn's multiple comparison tests. Statistical significance was achieved with a two-sided $P < 0.05$. All statistics were generated using GraphPad Prism software version 6.

3. Results

3.1. Variable Expression Levels of SSTR2 and NET in Neuroblastoma (NB) Tumor Cell Lines. The expression of

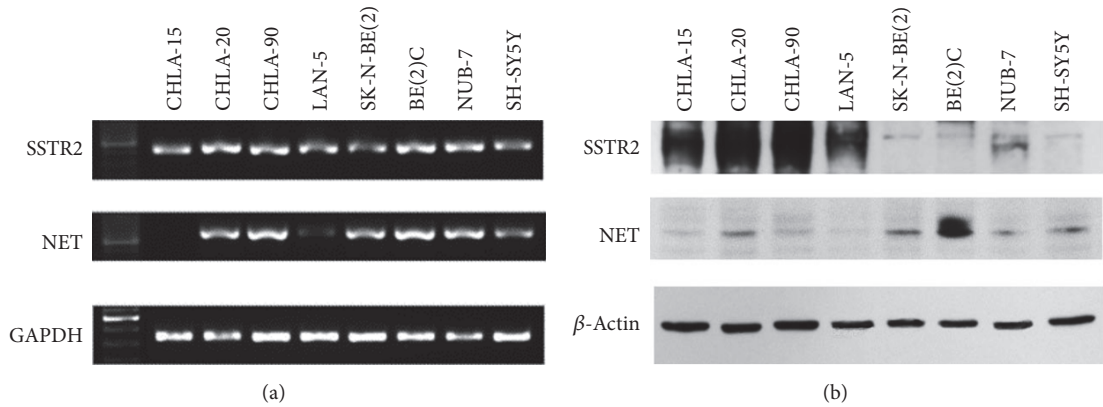

Figure 1: mRNA expression level and Western blotting analyses of SSTR2 and NET. (a) RNA was isolated from different neuroblastoma cell lines, converted into cDNA, followed by RT-PCR with SSTR2 and NET specific primers. The GAPDH gene was used as a reference gene. (b) Protein lysates were prepared from different neuroblastoma cell lines. Protein samples were separated by polyacrylamide gel electrophoresis. Expression of SSTR2 and NET proteins was visualized using specific antibodies. β-Actin was used as internal loading control.

somatostatin receptors (SSTR2) and NET in NB cell lines was determined using RT-PCR (Figure 1(a)) and Western blot (Figure 1(b)). Although different NB cell lines showed similar SSTR2 mRNA expression levels (Figure 1(a)), marked variation of SSTR2 protein expression was observed (Figure 1(b)). In some NB cell lines such as CHLA-15, CHLA-20, CHLA-90, and LAN-5, a prominent SSTR2 expression was detected, whereas, in others, a low level of SSTR2 expression was identified (Figure 1(b)). A similar variation was observed for the expression of NET, a primary transporter responsible for specific active cellular uptake of MIBG [15] (Figures 1(a) and 1(b)). Interestingly, some high SSTR2-expressing cell lines, CHLA-15, CHLA-90, and LAN-5, showed low expression levels of NET, which makes SSTR2 a potential alternative molecular target for NB imaging or treatment, especially for MIBG nonacid tumors.

In addition, SSTR2 or NET expression did not appear to be correlated with MYCN amplification or p53 mutation status. In some cell lines, two bands were detected using the monoclonal SSTR2 antibody (ab134152, Abcam), which is consistent with a previous report in which two bands were also detected in IMR-32 neuroblastoma cell lysates [16].

3.2. Uptake of ^{68}Ga-DOTA-TATE Correlates with SSTRT2 Expression in NB Xenografts. DOTA-TATE has a high affinity for SSTR2 *in vitro*. In order to assess the relationship between ^{68}Ga-DOTA-TATE uptake and SSTR2 expression, we selected a high SSTR2-expressing NB cell line, CHLA-15, and a low SSTR2-expressing cell line, SK-N-BE(2), for *in vivo* PET/CT tumor imaging. Tumor uptake was expressed as Standardized Uptake Value (SUV). As shown in Figures 2(a)–2(c), we observed a significant difference in the uptake of ^{68}Ga-DOTA-TATE between CHLA-15 and SK-N-BE(2) xenografts. The mean tumor uptake value of ^{68}Ga-DOTA-TATE was significantly higher in the CHLA-15 xenografts ($0.79 \pm 0.10\%$ ID/g; $P = 0.0003$), compared to SK-N-BE(2) tumors ($0.13 \pm 0.02\%$ ID/g; $P < 0.01$).

3.3. Histological Colocalization of SSTR2 and ^{68}Ga-DOTA-TATE Uptake. To further evaluate the relationship between SSTR2 expression and ^{68}Ga-DOTA-TATE uptake, we performed SSTR2 immunostaining and *ex vivo* autoradiography with CHLA-15 and SK-N-BE(2) xenograft sections. Consistent with the PET results, CHLA-15 tumors showed significantly higher accumulation of ^{68}Ga-DOTA-TATE as compared to SK-N-BE(2) tumors (Figures 3(a) and 3(b)). We also observed spatial heterogeneity for both SSTR2 expression (Figure 3(c)) and ^{68}Ga-DOTA-TATE accumulation (Figures 3(a) and 3(d)). When we merged the SSTR2 fluorescent staining and autoradiography images, we observed intratumoral colocalization of SSTR2 expression and ^{68}Ga-DOTA-TATE uptake (Figure 3(d)). Tumor regions with a high number of SSTR2-positive cells corresponded to focal areas of increased radioactivity. In SK-N-BE(2) tumors, both SSTR2 expression and ^{68}Ga-DOTA-TATE autoradiography signals were too weak to be detected (Figure 3(e)).

3.4. Therapeutic Effects of ^{177}Lu-DOTA-TATE on the CHLA-15 Xenograft Model. To verify the therapeutic effects of targeting SSTR2 with ^{177}Lu-DOTA-TATE, we treated CHLA-15 tumor-bearing mice with ^{177}Lu-DOTA-TATE at the dose of 20 MBq/animal. After 12 days, we started to observe significant tumor growth inhibition in the CHLA-15 xenograft model compared to control tumors ($P < 0.05$) (Figure 4(a)). From the slope of tumor growth curve, Lu-177-DOTA-TATE treated tumors regained tumor growth rate after day 12, which indicates that single dose Lu-177-DOTA-TATE may not achieve long-lasting antitumor effects. No overall toxicity with respect to body weight loss was observed at the dose of 20 MBq/animal (Figure 4(b)).

3.5. ^{123}I-MIBG Uptake by NB Xenografts Not Related to Their NET Expression In Vitro. To compare the effectiveness between ^{68}Ga-DOTA-TATE PET and ^{123}I-MIBG SPECT in our preclinical models, we further assessed ^{123}I-MIBG uptake

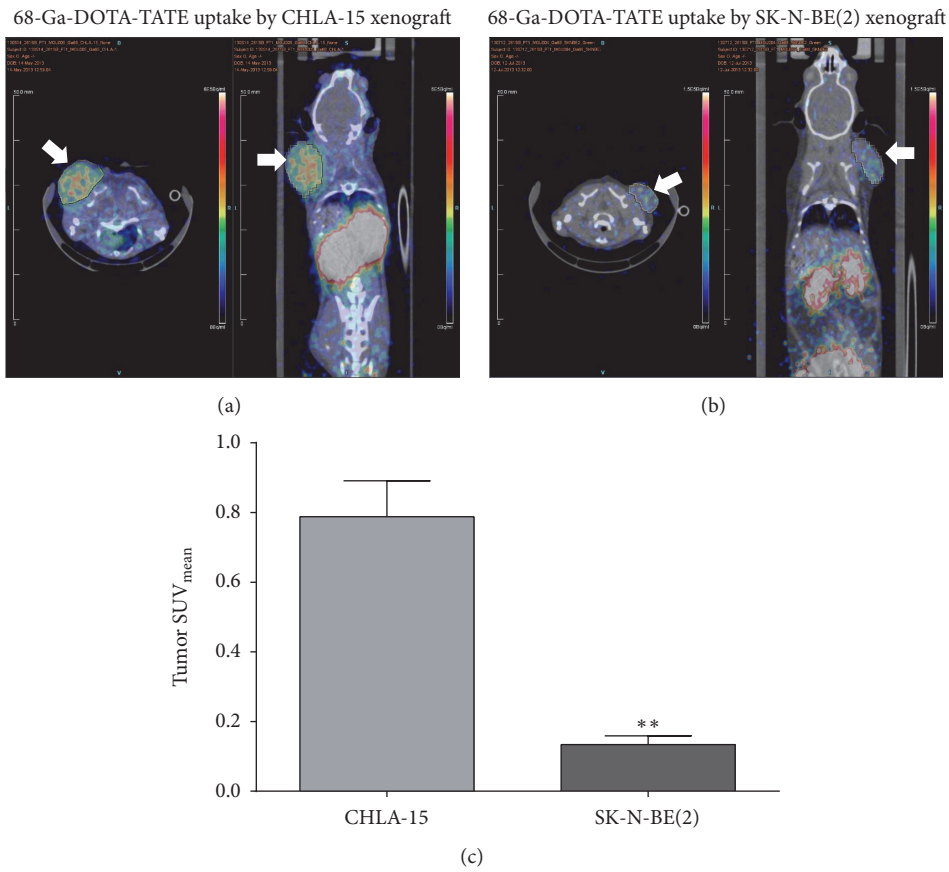

Figure 2: Representative micro-PET/CT images at 1 hour after injection of 10 MBq of ^{68}Ga-DOTA-TATE in the CHLA-15 (a) and SK-N-BE(2) (b) tumor-bearing NOD/SCID mice. Images were presented in the axial (left) and coronal (right) orientations. The white arrows denote localized tumor on the shoulder. (c) Standardized Uptake Values (SUV) in CHLA-15 and SK-N-BE(2) xenografts were calculated using the formula: SUV = $C_{PET}(T)$/(Injected dose/Bodyweight). The difference was significant between CHLA-5 and SK-N-BE(2) tumors ($^{**}P < 0.01$). Two-tailed unpaired t-tests were performed to compare the SUV$_{mean}$ values obtained.

in three neuroblastoma xenograft models, including NB cells expressed high, intermediate, and low amount of SSTR2 protein *in vitro*, BE(2)C, SK-N-BE(2), and CHLA-15 cells, respectively. As shown by ^{123}I-MIBG SPECT (Figures 5(a) and 5(b)) and ^{123}I-MIBG autoradiography (Figure 5(c)), uneven marginal uptake of ^{123}I-MIBG was observed in all three BE(2)C, SK-N-BE(2), and CHLA-15 xenograft tumors. Also, *in vivo* ^{123}I-MIBG uptake is not related to *in vitro* NET expression levels in three selected NB cell lines. Although BE(2)C cells had a relatively higher NET expression *in vitro*, their *in vivo* ^{123}I-MIBG uptake is at the similar level as the background, with the T/M ratio of 1.13 ± 0.13. We were not able to detect positive signals from NET immunohistochemistry staining with harvested NB xenografts. In order to compare the NET expression *in vivo*, we ran a Western blot of NET with homogenized tumor samples (Figure 5(d)). We did not, however, observe a significant difference of NET expression between CHLA-15, SK-N-BE(2), and BE(2)C xenografts, which indicates a possible change of NET expression profile due to *in vitro* cell culture (Figure 5(e)).

4. Discussion

Neuroblastoma is an extremely heterogeneous disease, both biologically and clinically, comprising tumor cells with very different molecular features. Somatostatin receptors (SSTRs) are variably expressed in neuroblastoma cell lines and tumors, as demonstrated by autoradiography, Western blot, immunohistochemistry, and RT-PCR techniques [17–19]. In this study, we selected a panel of NBL cells lines with different biological and genetic backgrounds (Table 1). We detected SSTR2 mRNA in most of the selected cell lines, but only 4 out of 8 cell lines express high levels of SSTR2 protein, including CHLA-15, CHLA-20, CHLA-90, and LAN-5 cells. In addition, expression of SSTR2 was not related to the p53 mutation and MYCN amplification status. Since the commercially available NB cell lines are mostly derived from stage IV patient samples, we are currently conducting a large-scale Children's Oncology Group biological study (COG ANBL14B3) with both high-risk and non-high-risk NB patient specimens to investigate the relationship between SSTR2 expression and clinical features.

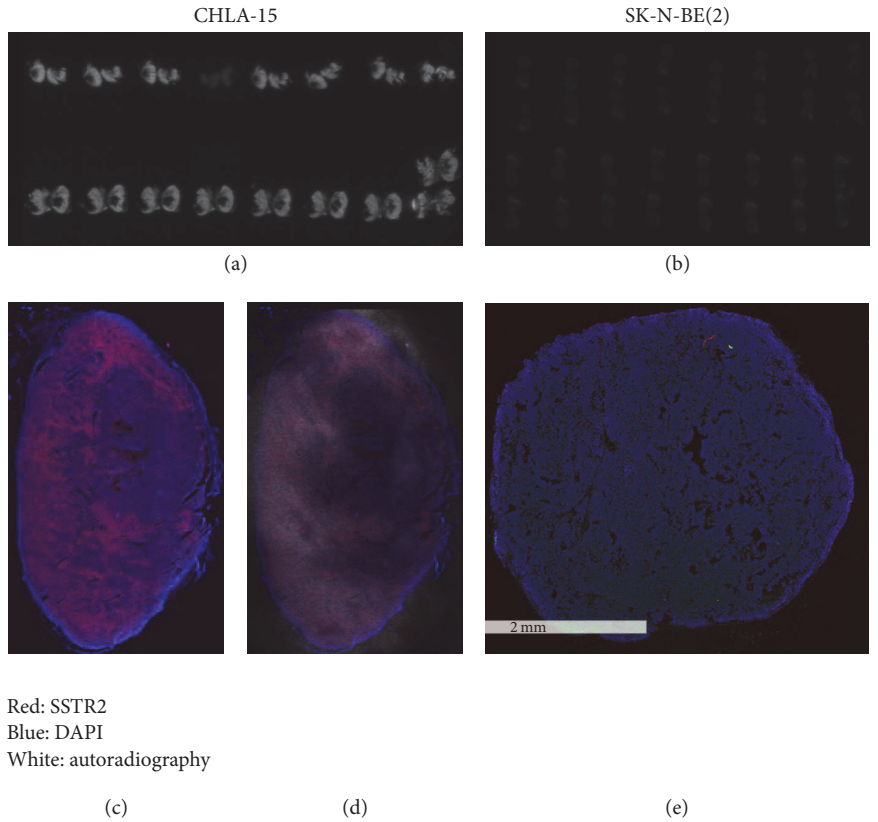

FIGURE 3: Colocalization of SSTR2 and autoradiography on CHLA-15 xenografts. CHLA-15 and SK-N-BE(2) tumors were removed immediately after PET/CT imaging. The spatial distribution of the ^{68}Ga-DOTA-TATE uptake was visualized by autoradiography (white signal) in the serial sections of CHLA-15 (a) and SK-N-BE(2) (b) tumors. (c) Representative CHLA-15 tumor section was stained for SSTR2 (red fluorescence) and DAPI (blue fluorescence). (d) The merging image of SSTR2 immunostaining and autoradiograph of the same CHLA-15 tumor section. (e) A representative SK-N-BE(2) tumor section stained for SSTR2 (red fluorescence) and DAPI (blue fluorescence).

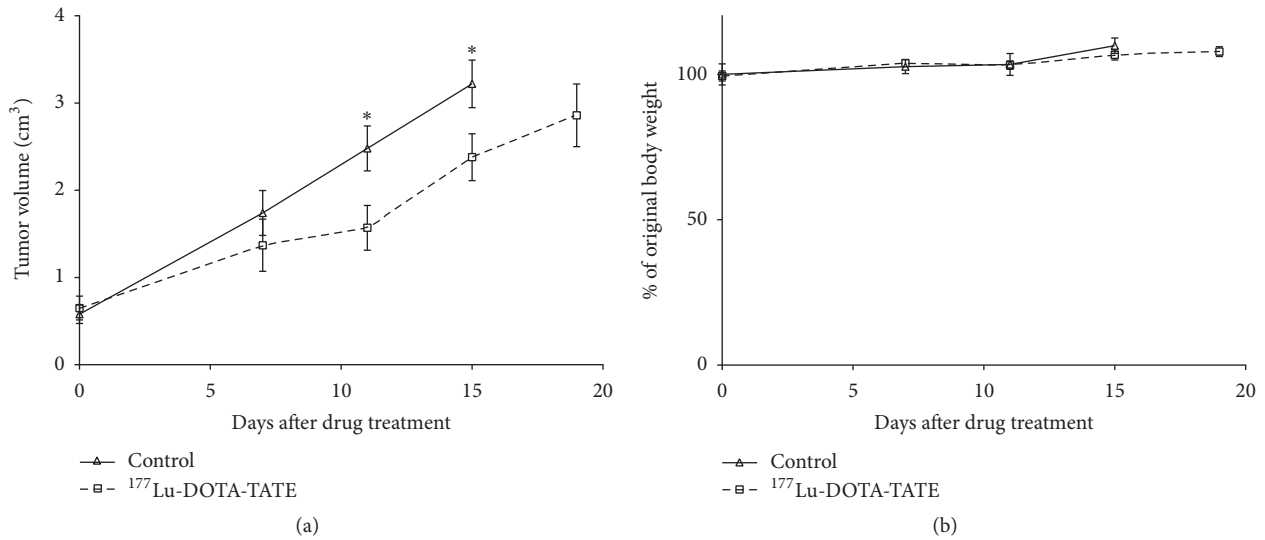

FIGURE 4: Antitumoral effects of ^{177}Lu-DOTA-TATE in the CHLA-15 neuroblastoma model. (a) Mice ($n = 7$) with subcutaneous CHLA-15 xenografts were treated with one dose of 20 MBq of ^{177}Lu-DOTA-TATE. Control mice ($n = 7$) received saline. Tumor volume was measured and plotted as shown. Values are stated as mean ± SE; $^*P < 0.05$. (b) Animal body weight was monitored in CHLA-15 tumor-bearing mice with/without ^{177}Lu-DOTA-TATE treatment.

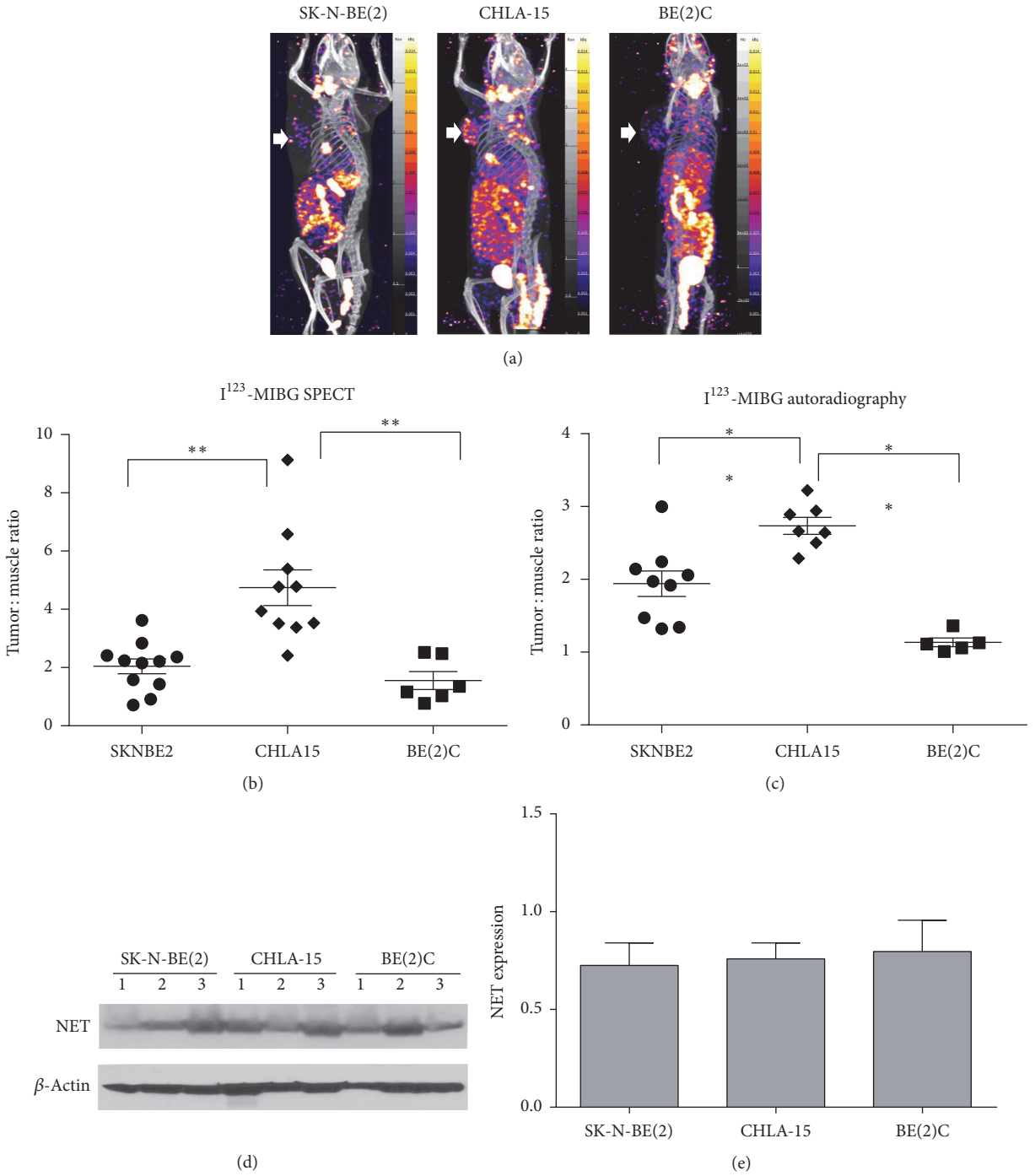

Figure 5: (a) Example images of ^{123}I-MIBG SPECT/CT in the SK-N-BE(2), CHLA-15, and BE(2)C xenograft models. The white arrows denote localized tumor on the shoulder. (b) Scatter plots of the tumor-to-muscle (T/M) ratios of ^{123}I-MIBG uptake in the SK-N-BE(2), CHLA-15, and BE(2)C xenograft models derived from SPECT/CT imaging. One-way analysis of variance (ANOVA) with Tukey's test was used for statistical analysis. $^{*}P < 0.05$; $^{**}P < 0.01$. (c) Scatter plots of the tumor-to-muscle (T/M) ratio of ^{123}I-MIBG autoradiography in the SK-N-BE(2), CHLA-15, and BE(2)C xenograft models. One-way ANOVA with Tukey's test was used for statistical analysis. $^{*}P < 0.05$; $^{**}P < 0.01$. (d) Western Blot of NET with homogenized CHLA-15, SK-N-BE(2), and BE(2)C xenografts. Three tumors were randomly selected from three groups for Western blot analysis. (e) Quantitative analysis of NET protein expression in CHLA-15, SK-N-BE(2), and BE(2)C xenografts. NET protein expression in Western blot images was quantified densitometrically using ImageJ software (NIH, USA) and normalized with respect to the corresponding expression of β-actin. Comparison of NET expression between different groups was analyzed by the nonparametric Kruskal-Wallis analysis with Dunn's multiple comparison tests. No significant difference of NET expression was observed between CHLA-15, SK-N-BE(2), and BE(2)C xenografts.

Peptide-receptor imaging and therapy with radiolabeled somatostatin analogs are an established and effective treatment option for adult patients with SSTR-positive neuroendocrine tumors [4]. ^{111}In-[diethylenetriaminepentaacetic acid (DTPA)]octreotide (Octreoscan; Mallinckrodt), a somatostatin analog, has been used for more than 15 years in the diagnosis and staging of SSTR-positive tumors. Nevertheless, it has a restricted ability to identify lesions smaller than 1 cm and to obtain a good spatial resolution, even when using SPECT rather than planar imaging [20]. In recent years, new PET-based radiopharmaceuticals targeting somatostatin receptors have been developed to address these issues. Several studies have demonstrated that ^{68}Ga-labeled DOTA-TOC or DOTA-TATE PET combined with CT has distinctly higher sensitivity and improved spatial resolution for the detection of SSTR-positive neuroendocrine tumors compared to scintigraphy with conventional SPECT imaging using Octreoscan [4, 21]. In this study, we successfully imaged ^{68}Ga-DOTA-TATE uptake in SSTR2-positive neuroblastoma xenografts with micro-PET/CT. We also observed intensive ^{68}Ga-DOTA-TATE uptake in MIBG-low-avidity CHLA-15 xenografts.

^{131}I-MIBG has been used over the past 15 years in multimodal therapy as a radiotherapeutic agent in relapsed and refractory NB patients [22]. However, only 30–40% of children with chemotherapy-refractory disease respond to ^{131}I-MIBG, and the responses are usually only transient [22–24]. In this study, we observed low ^{131}I-MIBG avidity in all selected NB cell lines. Although BE(2)C cells showed relatively elevated NET expression *in vitro*, we were not able to detect positive NET immunostaining with harvested BE(2)C xenografts. Western blot of NET with homogenized tumor samples showed similar NET expression levels between CHLA-15, SK-N-BE(2), and BE(2)C xenografts, which indicates a possible change of NET expression profile *in vivo*. We also demonstrated the complementary role of somatostatin receptor imaging in detecting additional sites of neuroendocrine tumors that were not visualized with ^{123}I-MIBG scintigraphy. Several clinical studies also confirmed discordant uptake patterns of MIBG and somatostatin receptor expression in some NB tumors [25]. Kroiss et al. [26], for example, described that somatostatin receptor imaging with ^{68}Ga-DOTA-TOC PET was able to detect the sites of disease in 2/4 patients with NB which were not visible by ^{123}I-MIBG. Numerous other studies in patients with neuroendocrine tumors have similarly demonstrated the complementary role of somatostatin receptor imaging in detecting additional sites of disease that were not visualized with ^{123}I-MIBG scintigraphy [27]. In this study, we observed discordant expression of NET and SSTR2 expression in NB-cell lines. CHLA-15 has a lower level of NET expression but higher SSTR2 expression compared to SK-N-BE(2) cells. *In vivo* PET/CT imaging demonstrated high ^{68}Ga-DOTA-TATE uptake in CHLA-15 xenografts compared to SK-N-BE(2) tumors. Consequently, somatostatin receptor expression and DOTA-TATE imaging could serve as an adjunct to existing diagnostic and therapeutic methods. They may provide valuable information for the pretherapeutic staging of the disease and impact patient outcomes.

One of the major goals of our study is to understand how the molecular expression of SSTR2 determined the responses of radioactively labeled DOTA-TATE. DOTA-TATE can also be radiolabeled with ^{177}Lu for targeted β^--particle radiotherapy. ^{177}Lu has a similar physical half-life as ^{131}I. ^{177}Lu emits a medium-energy β^--particle resulting in localized energy deposition; thus the targeted tissue receives low-dose-rate radiation exposure. Mouse studies of solid tumor xenografts found ^{177}Lu to be superior to other radiolanthanides in effecting tumor control with pretargeted therapy [28]. We demonstrated the antitumor effect of ^{177}Lu-DOTA-TATE on CHLA-15 xenografts which have high SSTR2 expression and elevated uptake of ^{68}Ga-DOTA-TATE. These characteristics may be valuable in future clinical trials: both ^{68}Ga-DOTA-TATE PET imaging and SSTR2 protein profile could serve as indicators for ^{177}Lu-DOTA-TATE treatment response. This avenue needs to be evaluated further in clinical scenarios.

5. Conclusions

This study has allowed us to demonstrate the association between SSTR2 expression and ^{68}Ga-DOTA-TATE uptake, which potentially leads to the antitumor activity of ^{177}Lu-DOTA-TATE in NB preclinical models. Histological colocalization of SSTR2 and ^{68}Ga-DOTA-TATE was also observed in our study. SSTR2 expression therefore could be used as a potential biomarker for predicting drug response to ^{177}Lu-DOTA-TATE radiotherapy. Moreover, in our model, we demonstrated that ^{68}Ga-DOTA-TATE PET is superior to ^{123}I-MIBG SPECT imaging in detecting NB xenograft tumors. The absence of significant difference of NET expression between various NB xenografts models and discordant *in vitro* and *in vivo* NET expression represent a limitation of our study which will require further investigation.

The ongoing COG study looking at the prevalence of SSTR2/NET expression in high-risk NB patients may allow us to identify a subset of patients who could benefit from this new SSRT2 targeted radiotherapeutic modality, in particular for the small number of patients demonstrating MIBG-nonavid tumors.

Conflicts of Interest

No potential conflicts of interest were disclosed by the authors.

Acknowledgments

This work was supported by CJ Memorial Fund, NuMedKids Fund, SickKids Foundation, and James Birrell Neuroblastoma Research Fund. The authors would like to acknowledge the Spatio-Temporal Targeting and Amplification of Radiation Response (STTARR) program and its affiliated funding agencies.

References

[1] R. Howman-Giles, P. J. Shaw, R. F. Uren, and D. K. V. Chung, "Neuroblastoma and Other Neuroendocrine Tumors," *Seminars in Nuclear Medicine*, vol. 37, no. 4, pp. 286–302, 2007.

[2] H. Mugishima, "Current status of molecular biology and treatment strategy for neuroblastoma," *International Journal of Clinical Oncology*, vol. 17, no. 3, p. 189, 2012.

[3] I. Ora and A. Eggert, "Progress in treatment and risk stratification of neuroblastoma: impact on future clinical and basic research," *Seminars in Cancer Biology*, vol. 21, no. 4, pp. 217–228, 2011.

[4] H. R. Maecke and J. C. Reubi, "Somatostatin receptors as targets for nuclear medicine imaging and radionuclide treatment," *Journal of Nuclear Medicine*, vol. 52, no. 6, pp. 841–844, 2011.

[5] K. Georgantzi, A. V. Tsolakis, M. Stridsberg, Å. Jakobson, R. Christofferson, and E. T. Janson, "Differentiated expression of somatostatin receptor subtypes in experimental models and clinical neuroblastoma," *Pediatric Blood and Cancer*, vol. 56, no. 4, pp. 584–589, 2011.

[6] F. D. Pashankar, M. S. O'Dorisio, and Y. Menda, "MIBG and somatostatin receptor analogs in children: current concepts on diagnostic and therapeutic use," *Journal of Nuclear Medicine*, vol. 46, no. 1, 2005.

[7] J. C. Reubi, J.-C. Schär, B. Waser et al., "Affinity profiles for human somatostatin receptor subtypes SST1-SST5 of somatostatin radiotracers selected for scintigraphic and radiotherapeutic use," *European Journal of Nuclear Medicine*, vol. 27, no. 3, pp. 273–282, 2000.

[8] Y. Menda, M. S. O'Dorisio, S. Kao et al., "Phase I trial of 90Y-DOTATOC therapy in children and young adults with refractory solid tumors that express somatostatin receptors," *Journal of Nuclear Medicine*, vol. 51, no. 10, pp. 1524–1531, 2010.

[9] D. J. Kwekkeboom, W. H. Bakker, B. L. Kam et al., "Treatment of patients with gastro-entero-pancreatic (GEP) tumours with the novel radiolabelled somatostatin analogue [177Lu-DOTA0,Tyr3]octreotate," *European Journal of Nuclear Medicine and Molecular Imaging*, vol. 30, no. 3, pp. 417–422, 2003.

[10] D. J. Kwekkeboom, W. W. de Herder, B. L. Kam et al., "Treatment with the radiolabeled somatostatin analog [177Lu-DOTA0,Tyr3]octreotate: toxicity, efficacy, and survival," *Journal of Clinical Oncology*, vol. 26, no. 13, pp. 2124–2130, 2008.

[11] J. E. Gains, J. B. Bomanji, N. L. Fersht et al., "177Lu-DOTATATE molecular radiotherapy for childhood neuroblastoma," *Journal of Nuclear Medicine*, vol. 52, no. 7, pp. 1041–1047, 2011.

[12] J. R. Masters, J. A. Thomson, B. Daly-Burns et al., "Short tandem repeat profiling provides an international reference standard for human cell lines," *Proceedings of the National Academy of Sciences of the United States of America*, vol. 98, no. 14, pp. 8012–8017, 2001.

[13] D. C. Vines, D. E. Green, G. Kudo, and H. Keller, "Evaluation of mouse tail-vein injections both qualitatively and quantitatively on small-animal PET tail scans," *Journal of Nuclear Medicine Technology*, vol. 39, no. 4, pp. 264–270, 2011.

[14] C. B. Johnbeck, M. M. Jensen, C. H. Nielsen, A. M. F. Hag, U. Knigge, and A. Kjaer, " ^{18}F-FDG and ^{18}F-FLT-PET imaging for monitoring everolimus effect on tumor-growth in neuroendocrine tumors: studies in human tumor xenografts in mice," *PLoS ONE*, vol. 9, no. 3, Article ID e91387, 2014.

[15] K. A. Streby, N. Shah, M. A. Ranalli, A. Kunkler, and T. P. Cripe, "Nothing but NET: A review of norepinephrine transporter expression and efficacy of 131I-mIBG therapy," *Pediatric Blood and Cancer*, vol. 62, no. 1, pp. 5–11, 2015.

[16] L.-C. Sun, L. V. Mackey, J. Luo, J. A. Fuselier, and D. H. Coy, "Targeted chemotherapy using a cytotoxic somatostatin conjugate to inhibit tumor growth and metastasis in nude mice," *Clinical Medicine: Oncology*, vol. 2, pp. 491–499, 2008.

[17] M. Maggi, E. Baldi, G. Finetti et al., "Identification, characterization, and biological activity of somatostatin receptors in human neuroblastoma cell lines," *Cancer Research*, vol. 54, no. 1, pp. 124–133, 1994.

[18] C. L. Moertel, J.-C. Reubi, B. S. Scheithauer, D. J. Schaid, and L. K. Kvols, "Expression of somatostatin receptors in childhood neuroblastoma," *American Journal of Clinical Pathology*, vol. 102, no. 6, pp. 752–756, 1994.

[19] C. C. Raggi, M. Maggi, D. Renzi et al., "Quantitative determination of sst2 gene expression in neuroblastoma tumor predicts patient outcome," *Journal of Clinical Endocrinology and Metabolism*, vol. 85, no. 10, pp. 3866–3873, 2000.

[20] A. Al-Nahhas, Z. Win, T. Szyszko, A. Singh, S. Khan, and D. Rubello, "What can gallium-68 PET add to receptor and molecular imaging?" *European Journal of Nuclear Medicine and Molecular Imaging*, vol. 34, no. 12, pp. 1897–1901, 2007.

[21] P. F. Rambaldi, V. Cuccurullo, V. Briganti, and L. Mansi, "The present and future role of ^{111}In Pentetreotide in the PET era," *Quarterly Journal of Nuclear Medicine and Molecular Imaging*, vol. 49, no. 3, pp. 225–235, 2005.

[22] S. G. DuBois and K. K. Matthay, "Radiolabeled metaiodobenzylguanidine for the treatment of neuroblastoma," *Nuclear Medicine and Biology*, vol. 35, no. 1, pp. S35–S48, 2008.

[23] J. P. Howard, J. M. Maris, L. S. Kersun et al., "Tumor response and toxicity with multiple infusions of high dose 131I-MIBG for refractory neuroblastoma," *Pediatric Blood and Cancer*, vol. 44, no. 3, pp. 232–239, 2005.

[24] R. J. Hutchinson, J. C. Sisson, B. Shapiro et al., "131-I-metaiodobenzylguanidine treatment in patients with refractory advanced neuroblastoma," *The American Journal of Clinical Oncology: Cancer Clinical Trials*, vol. 15, no. 3, pp. 226–232, 1992.

[25] A. Quigley, J. Buscombe, G. Gopinath, M. Caplin, and A. Hilson, "In-vivo characterisation of the functional aspects of carcinoid tumors by imaging somatostatin receptors and amine uptake," *Journal of nuclear medicine*, p. 74P, 2003, SOC NUCLEAR MEDICINE INC 1850 SAMUEL MORSE DR, RESTON, VA 20190-5316 USA.

[26] A. Kroiss, D. Putzer, C. Uprimny et al., "Functional imaging in phaeochromocytoma and neuroblastoma with 68Ga-DOTA-Tyr3-octreotide positron emission tomography and 123I-metaiodobenzylguanidine," *European Journal of Nuclear Medicine and Molecular Imaging*, vol. 38, no. 5, pp. 865–873, 2011.

[27] K. P. Koopmans, P. L. Jager, I. P. Kema, M. N. Kerstens, F. Albersy, and R. P. F. Dullaart, "111In-octreotide is superior to 123I- metaiodobenzylguanidine for scintigraphic detection of head and neck paragangliomas," *Journal of Nuclear Medicine*, vol. 49, no. 8, pp. 1232–1237, 2008.

[28] H. Mohsin, F. Jia, J. N. Bryan et al., "Comparison of pretargeted and conventional CC49 radioimmunotherapy using 149Pm, 166Ho, and 177Lu," *Bioconjugate Chemistry*, vol. 22, no. 12, pp. 2444–2452, 2011.

Hindawi
Contrast Media & Molecular Imaging
Volume 2017, Article ID 6162845, 7 pages
https://doi.org/10.1155/2017/6162845

Clinical Study

A First Report on [^{18}F]FPRGD$_2$ PET/CT Imaging in Multiple Myeloma

Nadia Withofs,[1] François Cousin,[1] Bernard De Prijck,[2] Christophe Bonnet,[2] Roland Hustinx,[1] Sanjiv S. Gambhir,[3] Yves Beguin,[2] and Jo Caers[2]

[1]*CHU of Liege, Nuclear Medicine and Oncological Imaging Division, Medical Physics Department, Liege, Belgium*
[2]*CHU of Liege, Department of Clinical Hematology, Liege, Belgium*
[3]*Molecular Imaging Program at Stanford (MIPS), Radiology Department, Stanford University, Stanford, CA, USA*

Correspondence should be addressed to Jo Caers; jo.caers@chu.ulg.ac.be

Received 19 March 2017; Revised 15 May 2017; Accepted 13 June 2017; Published 27 July 2017

Academic Editor: Xuelei Ma

An observational study was set up to assess the feasibility of [^{18}F]FPRGD$_2$ PET/CT for imaging patients with multiple myeloma (MM) and to compare its detection rate with low dose CT alone and combined [^{18}F]NaF/[^{18}F]FDG PET/CT images. Four patients (2 newly diagnosed patients and 2 with relapsed MM) were included and underwent whole-body PET/CT after injection of [^{18}F]FPRGD$_2$. The obtained images were compared with results of low dose CT and already available results of a combined [^{18}F]NaF/[^{18}F]FDG PET/CT. In total, 81 focal lesions (FLs) were detected with PET/CT and an underlying bone destruction or fracture was seen in 72 (89%) or 8 (10%) FLs, respectively. Fewer FLs (54%) were detected by [^{18}F]FPRGD$_2$ PET/CT compared to low dose CT (98%) or [^{18}F]NaF/[^{18}F]FDG PET/CT (70%) and all FLs detected with [^{18}F]FPRGD$_2$ PET were associated with an underlying bone lesion. In one newly diagnosed patient, more [^{18}F]FPRGD$_2$ positive lesions were seen than [^{18}F]NaF/[^{18}F]FDG positive lesions. This study suggests that [^{18}F]FPRGD$_2$ PET/CT might be less useful for the detection of myeloma lesions in patients with advanced disease as all FLs with [^{18}F]FPRGD$_2$ uptake were already detected with CT alone.

1. Background

The introduction of efficient and less toxic treatments caused a paradigm shift in the management of multiple myeloma (MM) towards an earlier diagnosis and treatment [1, 2]. To detect early signs of bone disease and to identify those patients for whom treatment is needed, highly sensitive imaging techniques are required. Positron emission tomography combined with computed tomography (PET/CT) using [^{18}F]fluorodeoxyglucose ([^{18}F]FDG) has already proven to be a sensitive technique for the detection of metabolically active MM lesions and was recently incorporated in the diagnostic work-up of MM by the International Myeloma Working Group (IMWG) accordingly [3].

Alternatively, the ^{18}F-FB-mini-PEG-E[c(RGDyK)]$_2$ ([^{18}F]FPRGD$_2$), a validated radiopharmaceutical with high binding affinity for integrin $\alpha_v\beta_3$, seems attractive for the detection of MM lesions [4–8]. The RGD-based radiopharmaceuticals were initially developed to accelerate the development of therapies targeting integrin $\alpha_v\beta_3$ [9]. The high expression of integrin $\alpha_v\beta_3$ by activated endothelial cells during angiogenesis aroused keen interest in RGD-based radiopharmaceuticals for imaging of tumor angiogenesis [10, 11]. Nevertheless, the integrin $\alpha_v\beta_3$ is not solely expressed by activated endothelial cells; it can be overexpressed by many types of cancer cells, regulating cell survival, metastases, and drug resistance [12]. In the case of myeloma, the integrin $\alpha_v\beta_3$ is expressed by activated endothelial cells but it can also be overexpressed by myeloma tumor cells and other cell types of the tumor microenvironment such as osteoclasts [13–17]. Our group previously studied the use of [^{18}F]FPRGD$_2$ in rectal and renal cancers, where a correlation between integrin $\alpha_v\beta_3$ expression and tracer uptake was shown [7, 8]. Since multiple players within the myeloma microenvironment express the integrin $\alpha_v\beta_3$, we hypothesized that [^{18}F]FPRGD$_2$ PET/CT could be an

effective imaging technique for the detection of myeloma lesions.

The combination of [^{18}F]NaF and [^{18}F]FDG for PET/CT is another strategy to improve the detection of bone metastases and was first introduced by Iagaru et al. [18, 19]. The rationale for the use of both [^{18}F]NaF, allowing the detection of bone metastases with bone formation, and [^{18}F]FDG, enabling the detection of metastases with increased rate of glucose metabolism, was to improve the sensitivity for detecting metastatic lesions. A prospective clinical trial evaluating combined [^{18}F]NaF and [^{18}F]FDG for PET/CT in patients with MM is currently under investigation (EudraCT 2013-004807-38), aiming at comparing its capacity to detect MM lesions with the capacities of magnetic resonance imaging, CT alone, and whole-body X-rays [20].

The current observational study was set up to assess the feasibility of [^{18}F]FPRGD$_2$ PET/CT to identify myeloma lesions. Secondarily, the detection rate of [^{18}F]FPRGD$_2$ PET/CT was compared to CT alone. Additionally, [^{18}F]FPRGD$_2$ PET/CT images were compared to combined [^{18}F]NaF/[^{18}F]FDG PET/CT images, available for those patients that were also included in the above-mentioned trial [20].

2. Materials and Methods

Patients with newly diagnosed or relapsed MM were prospectively included. This study was registered as EudraCT #2013-004807-38 and was approved by the Ethics Committee of the academic hospital (CHU of Liege). All subjects provided written informed consent for this study.

The radiosynthesis of [^{18}F]FPRGD$_2$ was performed as previously reported and in compliance with current good manufacturing practice regulations [5, 7]. The mean (±standard deviation) injected mass of the active pharmaceutical ingredient was 11.1 μg (±1.6 μg) [7].

Every patient underwent whole-body (WB) scans, from vertex to toes, using [^{18}F]FPRGD$_2$ PET/CT and combined [^{18}F]NaF/[^{18}F]FDG PET/CT (median delay between scans: 4 days; range: 3–5 d). PET/CT scans were acquired in a Gemini TF scanner after injection of 296 ± 9 MBq [^{18}F]FPRGD$_2$ (median uptake time: 62 min) or 133 ± 6 MBq [^{18}F]NaF and 242 ± 27 MBq [^{18}F]FDG (median delay between [^{18}F]FDG and [^{18}F]NaF injections: 2 min and uptake time: 66 min). All patients fasted for 6 h prior to radiopharmaceutical injection (glycemia < 120 μg/ml in all patients). A low dose CT (3 mm slice thickness; 120 kV and 50 to 80 mAs depending on patient's weight) followed by the PET emission scan of 90 seconds per bed position was performed.

The PET/CT images were reviewed by 2 experienced nuclear medicine physicians and 2 radiologists to detect focal lesions (FLs) and/or diffuse bone marrow involvement. Areas of tracers' uptake corresponding to degenerative changes were excluded. Focal areas of increased uptake, regardless of the presence of bone abnormality on CT images, and hypoactive FLs with underlying bone destruction on CT images and suspected of being associated with myeloma lesions were considered PET MM FLs. The FLs were classified according to their location in 7 regions of the body: pelvis, skull, superior limbs, inferior limbs, spine, ribs, and one location including the sternum, scapula, and clavicles. A 1.2 ml volume of interest was drawn in the focal area of radiopharmaceutical's uptake to estimate the maximum standardized uptake value (SUV_{max}). The maximum diameter of the osteolytic lesions, when present, was also measured. The results are presented as means ± standard deviation (SD).

Table 1: Patients' characteristics (n = 4).

Feature	n
Median age (range)	
65 (51–79) years	4
Sex	
Female	1
Male	3
Mean ± SD BMPC infiltration (%)	
48 ± 29%	4
Ig isotype	
IgG	4
ISS stage at diagnosis	
I	1
III	3
Relapsed MM	
Time from diagnosis	
40 & 58 months	2
Time from last treatment	
35 & 52 months	
Prior treatment	
Thalidomide-dexamethasone/ASCT	1
Melphalan-prednisone-thalidomide	1
No prior bisphosphonates therapy	4

Ig = immunoglobulin; BMPC = bone marrow plasma cell; ASCT = autologous stem cell transplantation.

3. Results

Four patients with MM were included, n = 2 with newly diagnosed MM and n = 2 with relapsed MM (Table 1). Based on the low dose CT images, the pattern of bone marrow involvement was focal (n = 2) or combined diffuse and focal (n = 2). Per patient, ≤3 FL (n = 2) or >10 FLs (n = 2) were detected. No extramedullary disease was detected. Overall, 81 FLs were detected with PET/CT with underlying bone destruction on CT images (n = 72; 89%) or fractures (n = 8; 10%; vertebra n = 5; rib n = 3) and one FL (1%) detected with [^{18}F]NaF/[^{18}F]FDG PET in the femur did not show any abnormality on CT images. Overall, the detection rate of [^{18}F]FPRGD$_2$ PET was lower than [^{18}F]NaF/[^{18}F]FDG PET, whatever the FL location, and the mean uptake (SUV_{max}) of [^{18}F]FPRGD$_2$ was overall lower than [^{18}F]NaF/[^{18}F]FDG (Table 2). Out of the 72 osteolytic FLs detected with the CT of the PET, only 50% (36/72) showed [^{18}F]FPRGD$_2$ uptake (Figure 1). Nonetheless, in one patient with newly diagnosed MM (Figure 1: patient #1), five

Table 2: Focal lesions detected with CT and PET and lesions' characteristics.

	Whole-body CT	$[^{18}F]FPRGD_2$ PET	$[^{18}F]NaF/[^{18}F]FDG$ PET
Number of osteolytic lesions ($n = 72$)	$n = 72$ (89%)	$n = 36$ (44%)	$n = 47$ (64%)††
Mean ± SD SUV_{max}		*2.5 ± 0.8*	*8.5 ± 4.3*
Number of fractures ($n = 8$)	$n = 8$ (10%)	$n = 8$ (10%)	$n = 8$ (10%)
Mean ± SD SUV_{max}		*3.3 ± 1.2*	*9.4 ± 2.3*
Number of FLs without any abnormality on CT images	$n = 0$	$n = 0$	$n = 1$ (1%)
Total number of FLs ($n = 81$)†	$n = 80$ (99%)	$n = 44$ (54%)	$n = 56$ (69%)

†Number of FLs regardless of the presence of bone abnormality on low dose CT images, or hypoactive FLs with underlying bone destruction on CT images were considered PET FLs. ††Two out of 47 were hypoactive FLs; they were not considered in the measurement of SUV.

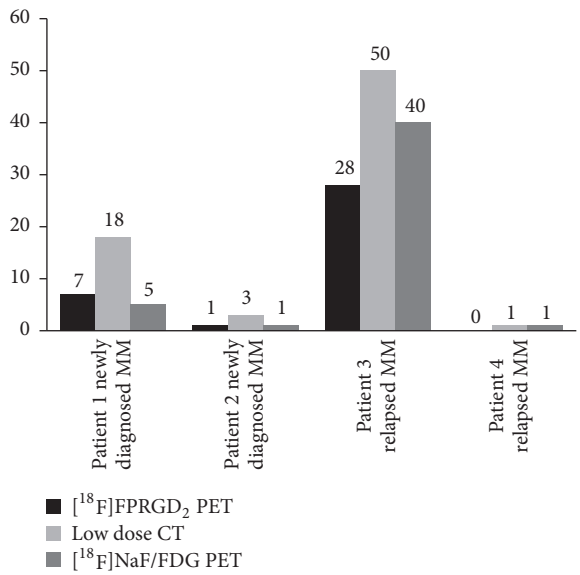

Figure 1: Detection rate of osteolytic FLs of CT, $[^{18}F]NaF/FDG$ PET/CT, and $[^{18}F]FPRGD_2$ PET/CT per patient ($n = 4$) and overall.

FLs showed $[^{18}F]FPRGD_2$ uptake but no $[^{18}F]NaF/[^{18}F]FDG$ uptake (Figure 2). In patient # 2 (Figure 1), both $[^{18}F]FPRGD_2$ and $[^{18}F]NaF/[^{18}F]FDG$ PET/CT detected one rib osteolytic FL, while 2 additional osteolytic FLs were detected with CT. In patient #3 (Figure 1), the detection rate of $[^{18}F]FPRGD_2$ PET was much lower than $[^{18}F]NaF/[^{18}F]FDG$ PET (Figure 3). In patient #4 (Figure 1), $[^{18}F]FPRGD_2$ PET/CT overlooked one 5 mm osteolytic FL of the cortical bone of a femur that was detected with $[^{18}F]NaF/[^{18}F]FDG$ PET/CT. In the contingency Table 3, the obtained results in patients with newly diagnosed disease are compared to those of patients with relapsing disease. $[^{18}F]FPRGD_2$ positive lesions without concomitant $[^{18}F]NaF/[^{18}F]FDG$ uptake were observed in one patient with newly diagnosed disease, while patient #3 (with a disease relapse) showed $[^{18}F]NaF/[^{18}F]FDG$ positive lesions without $[^{18}F]FPRGD_2$ uptake.

4. Discussion

Our purpose was to explore the detection capabilities of $[^{18}F]FPRGD_2$ PET/CT and to assess its feasibility in MM disease. In the studied patients, the detection rate of $[^{18}F]FPRGD_2$ PET was lower than the detection rate of low dose CT alone (Figure 1). Every FL showing $[^{18}F]FPRGD_2$ uptake corresponded to an osteolytic lesion or a fracture on low dose CT images. Although the integrin $\alpha_v\beta_3$ is expressed by multiple cells in tumor microenvironment such as MM tumor cells, osteoclasts, and activated endothelial cells during angiogenesis, our clinical observation suggests that $[^{18}F]FPRGD_2$ PET/CT does not allow a higher detection rate of MM bone lesions than low dose CT alone. The detection rate of $[^{18}F]FPRGD_2$ PET was overall lower than $[^{18}F]NaF/[^{18}F]FDG$ PET (patient #3; Figures 1 and 3) but in one patient, more lesions were visible on the $[^{18}F]FPRGD_2$ scan (patient #1; Figures 1 and 2). The prognostic value of $[^{18}F]FPRGD_2$ positive lesions and the value of $[^{18}F]FPRGD_2$ PET/CT in patients with asymptomatic disease (and thus without bone lesions) were not studied and could be of interest. On the other hand, the high bone marrow background activity related to $[^{18}F]NaF$ uptake may explain why some of the FLs detected with $[^{18}F]FPRGD_2$ PET/CT were not seen with $[^{18}F]NaF/[^{18}F]FDG$. Diffuse bone marrow infiltration was not reliably estimated with $[^{18}F]NaF/[^{18}F]FDG$ PET due to high $[^{18}F]NaF$ bone uptake while it was suspected with $[^{18}F]FPRGD_2$ PET/CT in 2 of the 4 patients (Figure 4).

Our report included 2 patients with relapsed MM and thus with possible long-lasting healed lesions. In one of these patients (patient #3; Figure 3), some of the osteolytic lesions did not show uptake of $[^{18}F]FPRGD_2$ while $[^{18}F]NaF/[^{18}F]FDG$ PET showed tracer's uptake in all these lesions, indicating residual activity. However, whether the uptake was related to $[^{18}F]FDG$ in the presence of residual metabolically active tumor and/or whether it was related to $[^{18}F]NaF$ due to bone turnover in the long-lasting healing process of bone lesions after treatment is unknown [21]. Moreover, we excluded patients with a short treatment-free interval before inclusion to avoid PET-negativity induced by a recent chemotherapy.

As mentioned in the introduction, both imaging techniques highlight different biological aspects. $[^{18}F]FPRGD_2$ allows the estimation of integrin $\alpha_v\beta_3$ expression by endothelial cells (and thus neovascularization), tumor cells, and activated osteoclasts, while $[^{18}F]NaF/[^{18}F]FDG$ uptake reflects

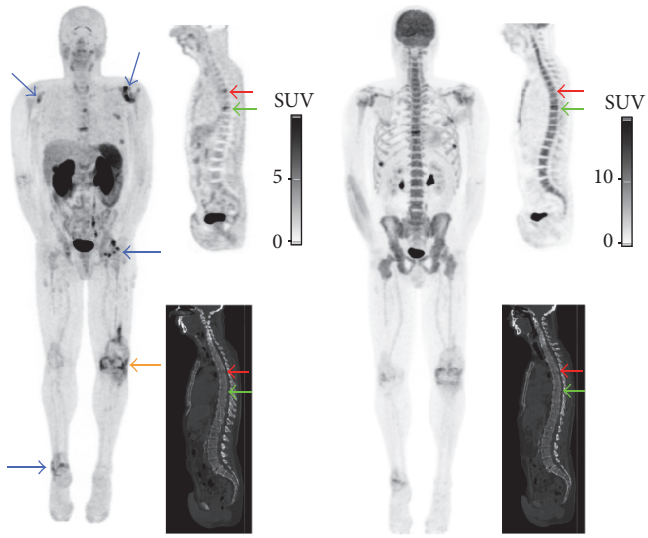

Figure 2: [^{18}F]FPRGD$_2$ and [^{18}F]NaF/[^{18}F]FDG PET/CT images of patient #1 with newly diagnosed MM. The [^{18}F]FPRGD$_2$ PET/CT images ((a) maximum intensity projection, MIP, and sagittal slices) show two spinal FLs with [^{18}F]FPRGD$_2$ uptake: one in the vertebral body of T5 corresponding to a mixed lesion on CT images ((a) red arrows) and a pathologic fracture of T8 ((a) green arrows). The [^{18}F]NaF/[^{18}F]FDG PET/CT images ((b) MIP and sagittal slices) show [^{18}F]NaF/[^{18}F]FDG uptake in T8 ((b) green arrows) but not in T5 ((b) red arrows). In addition, [^{18}F]FPRGD$_2$ uptake was also observed in glenohumeral, left hip, and right ankle joints ((a) blue arrows) as well as in the left total knee arthroplasty ((a) orange arrow). The observation of [^{18}F]FPRGD$_2$ uptake in musculoskeletal disorders has already been published [6].

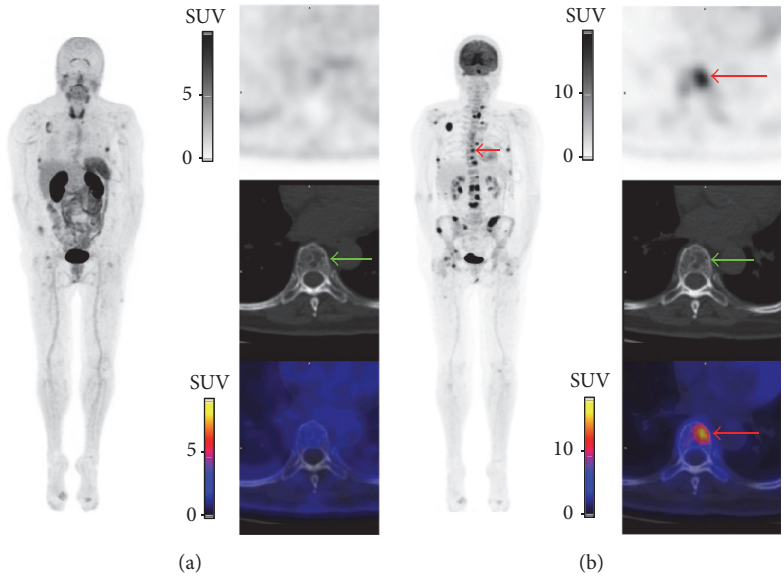

Figure 3: [^{18}F]FPRGD$_2$ PET/CT (a) and [^{18}F]NaF/[^{18}F]FDG PET/CT (b) images of patient #3 with MM at time of relapse, more than 4 years after diagnosis and end of treatment. The number of osteolytic FLs with [^{18}F]FPRGD$_2$ uptake (n = 28) was far lower than with [^{18}F]NaF/[^{18}F]FDG uptake (n = 40). The green arrows point at an osteolytic FL of T9 showing high [^{18}F]NaF/[^{18}F]FDG uptake ((b) red arrows; SUV$_{max}$ 10.2) but no focal [^{18}F]FPRGD$_2$ uptake ((a) SUV$_{max}$ 1.8).

tumor cell metabolism and/or bone formation. The heterogeneous uptake of [^{18}F]FPRGD$_2$ can be explained by biological phenomena and previously received treatments. The myeloma-induced angiogenesis appears after an "angiogenic switch" due to the release of angiogenic factors by subsets of myeloma cells or can be directly in proportion to the tumor infiltration inside the bone marrow [22]. This angiogenesis is counteracted by targeted treatments such as thalidomide and bortezomib which could explain reduced uptake in relapsing patients. Decreased uptake of [^{18}F]FDG was recently found to be associated with reduced expression of *hexokinase-2*, responsible for the first step of glycolysis [23].

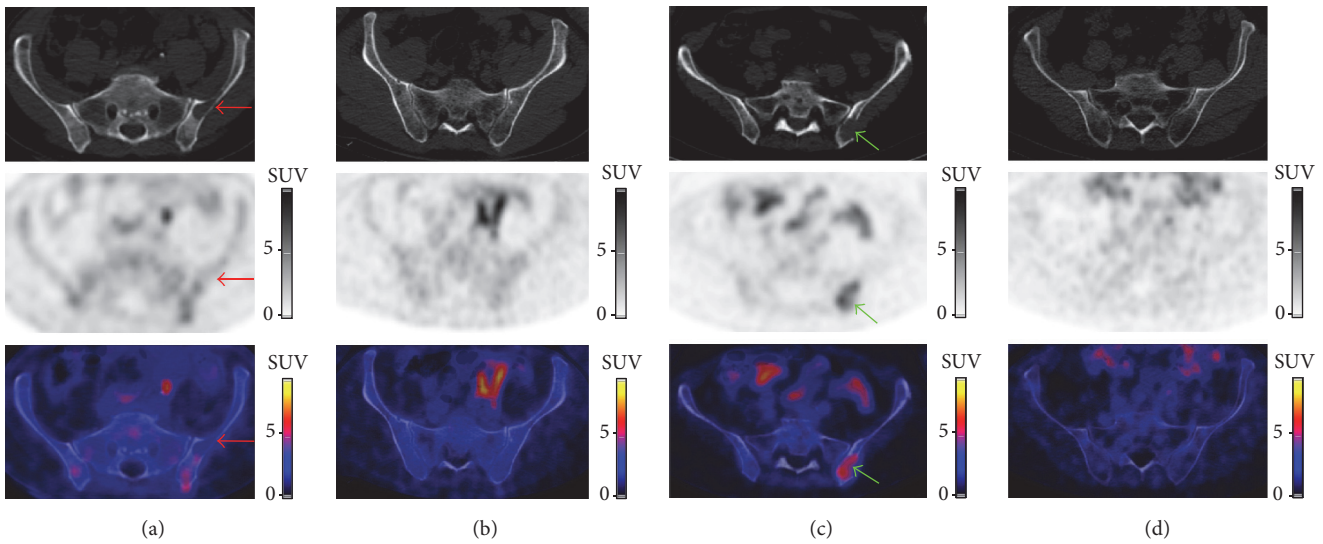

Figure 4: [^{18}F]FPRGD$_2$ PET/CT images of all patients. A diffuse bone marrow involvement was described based on CT images in patients #1 (a) and #2 (b); the [^{18}F]FPRGD$_2$ PET images also showed diffuse and heterogeneous bone marrow [^{18}F]FPRGD$_2$ uptake in patients #1 (a) and a mild diffuse bone marrow uptake in patient #2 (b). In contrast, no diffuse bone marrow [^{18}F]FPRGD$_2$ uptake was seen in patients #3 ((c) the green arrows point at a lytic FL with [^{18}F]FPRGD$_2$ uptake) and #4 ((d) no lesion shown). Note that, in patient #1 (a) with newly diagnosed MM, a large osteolytic FL in CT images did not show [^{18}F]FPRGD$_2$ uptake above the bone marrow background ((a) red arrows).

Table 3: Focal lesions detected per patient.

Patient	Newly diagnosed MM		Relapsed-MM		Total
	# 1	# 2	# 3	# 4	
Concordant results[†]	2	1	28	0	*31*
[^{18}F]FPRGD$_2$+ and [^{18}F]NaF/FDG−	5	0	0	0	*5*
[^{18}F]FPRGD$_2$− and [^{18}F]NaF/FDG+	3	0	12	1	*16*
[^{18}F]FPRGD$_2$ & CT− and [^{18}F]NaF/FDG+	0	0	1	0	*1*
CT− and [^{18}F]FPRGD$_2$+	0	0	0	0	*0*
CT+ and both PET−	8	2	10	0	*20*
Total malignant lesions	*18*	*3*	*51*	*1*	*73*
Fractures	3	3	1	1	8

[†]Osteolytic FLs showing both [^{18}F]FPRGD$_2$ and [^{18}F]NaF/FDG uptake.

Even though this case report suggests that [^{18}F]FPRGD$_2$ PET/CT might not be appropriate for detection of MM lesions, it may be of use in the assessment of integrin $\alpha_v\beta_3$ expression in MM lesions, especially in clinical trials evaluating inhibitors targeting $\alpha_v\beta_3$ integrins, as recently investigated by Tucci et al. [24]. In addition, our study focused on patients with symptomatic myeloma disease, while [^{18}F]FPRGD$_2$ PET/CT might be useful to detect bone marrow infiltration in precursor states of the disease (smoldering multiple myeloma or monoclonal gammopathy of undetermined significance).

5. Conclusions

In this case report, [^{18}F]FPRGD$_2$ PET/CT detected only 50% of the FLs detected by CT suggesting that the clinical utility of [^{18}F]FPRGD$_2$ PET/CT is rather limited for the detection of overt MM lesions. However, the clinical and possibly prognostic relevance of [^{18}F]FPRGD$_2$ positive MM lesions needs further investigation.

Abbreviations

PET: Positron emission tomography
CT: Computed tomography
[^{18}F]FDG: [^{18}F]Fluorodeoxyglucose
FL: Focal lesion
MM: Multiple myeloma
WB: Whole-body
IMWG: International Myeloma Working Group
SUV: Standardized uptake value
SD: Standard deviation.

Ethical Approval

All procedures performed in this report were in accordance with the ethical standards of the institutional research

committee and with the principles of the 1964 Declaration of Helsinki and its later amendments or comparable ethical standards. This Belgian monocentric prospective protocol (EudraCT 2013-004807-38) was approved by the Ethics Committee of the University Hospital of Liege and the Federal Agency for Medicines and Health Products (FAMHP).

Consent

Every enrolled patient signed specific informed consent.

Conflicts of Interest

The authors declare that they have no conflicts of interest.

Authors' Contributions

Nadia Withofs and Roland Hustinx supervised PET/CT image acquisition and analyzed the PET/CT images. François Cousin analyzed the CT images. Sanjiv S. Gambhir shared his expertise in [^{18}F]FPRGD$_2$ PET/CT. Jo Caers and Yves Beguin designed the study and recruited and informed patients. Bernard De Prijck and Christophe Bonnet informed and recruited patients. Every author contributed to the writing of the manuscript.

Acknowledgments

The authors thank Frederic Mievis, Fabrice Giacomelli, and Christine Mella (Cyclotron Research Centre, University of Liege, Belgium) for the syntheses of [^{18}F]FPRGD$_2$ and [^{18}F]NaF. This work has been supported by grants from the Foundation against Cancer, Fonds de la Recherche Scientifique Médicale, FIRS Research Fund (CHU de Liège), the Fonds National de la Recherche Scientifique (FNRS, Belgium), and the Fonds Spéciaux de la Recherche (University of Liege).

References

[1] S. V. Rajkumar, M. A. Dimopoulos, and A. Palumbo, "International Myeloma Working Group updated criteria for the diagnosis of multiple myeloma," *The Lancet Oncology*, vol. 15, no. 12, pp. e538–e548, 2014.

[2] J. Caers, C. F. De Larrea, X. Leleu et al., "The changing landscape of smoldering multiple myeloma: a european perspective," *Oncologist*, vol. 21, no. 3, pp. 333–342, 2016.

[3] M. Cavo, E. Terpos, C. Nanni et al., "Role of ^{18}F-FDG PET/CT in the diagnosis and management of multiple myeloma and other plasma cell disorders: a consensus statement by the International Myeloma Working Group," *The Lancet Oncology*, vol. 18, no. 4, pp. e206–e217, 2017.

[4] Z. Wu, Z.-B. Li, W. Cai et al., "^{18}F-labeled mini-PEG spacered RGD dimer (^{18}F-FPRGD$_2$): synthesis and microPET imaging of $\alpha_v\beta_3$ integrin expression," *European Journal of Nuclear Medicine and Molecular Imaging*, vol. 34, no. 11, pp. 1823–1831, 2007.

[5] D. Thonon, D. Goblet, E. Goukens et al., "Fully automated preparation and conjugation of N-succinimidyl 4-[^{18}F]fluorobenzoate ([^{18}F]SFB) with RGD peptide using a GE FASTlab synthesizer," *Molecular Imaging and Biology*, vol. 13, no. 6, pp. 1088–1095, 2011.

[6] N. Withofs, E. Charlier, P. Simoni et al., "^{18}F-FPRGD$_2$ PET/CT imaging of musculoskeletal disorders," *Annals of Nuclear Medicine*, vol. 29, no. 10, pp. 839–847, 2015.

[7] N. Withofs, N. Signolle, J. Somja et al., " ^{18}F-FPRGD$_2$ PET/CT imaging of integrin $\alpha_v\beta_3$ in renal carcinomas: correlation with histopathology," *Journal of Nuclear Medicine*, vol. 56, no. 3, pp. 361–364, 2015.

[8] N. Withofs, P. Martinive, J. Vanderick et al., "[^{18}F]FPRGD$_2$ PET/CT imaging of integrin $\alpha_v\beta_3$ levels in patients with locally advanced rectal carcinoma," *European Journal of Nuclear Medicine and Molecular Imaging*, vol. 43, no. 4, pp. 654–662, 2016.

[9] R. Haubner, HJ. Wester, U. Reuning, R. Senekowitsch-Schmidtke, B. Diefenbach, and H. Kessler, "Radiolabeled $\alpha_v\beta_3$ integrin antagonists: a new class of tracers for tumor targeting," *Journal of Nuclear Medicine*, pp. 40–1061, 1999.

[10] S. M. Weis and D. A. Cheresh, "α_v integrins in angiogenesis and cancer," *Cold Spring Harbor perspectives in medicine*, vol. 1, no. 1, p. a006478, 2011.

[11] F. C. Gaertner, H. Kessler, H.-J. Wester, M. Schwaiger, and A. J. Beer, "Radiolabelled RGD peptides for imaging and therapy," *European Journal of Nuclear Medicine and Molecular Imaging*, vol. 39, no. 1, pp. S126–S138, 2012.

[12] L. Seguin, J. S. Desgrosellier, S. M. Weis, and D. A. Cheresh, "Integrins and cancer: regulators of cancer stemness, metastasis, and drug resistance," *Trends in Cell Biology*, vol. 25, no. 4, pp. 234–240, 2015.

[13] T. J. Wadas, H. Deng, J. E. Sprague, A. Zheleznyak, K. N. Weilbaecher, and C. J. Anderson, "Targeting the $\alpha_v\beta_3$ integrin for small-animal PET/CT of osteolytic bone metastases," *Journal of Nuclear Medicine*, vol. 50, no. 11, pp. 1873–1880, 2009.

[14] K. Cohen, N. Flint, S. Shalev et al., "Thyroid hormone regulates adhesion, migration and matrix metalloproteinase 9 activity via $\alpha_v\beta_3$ integrin in myeloma cells," *Oncotarget*, vol. 5, no. 15, pp. 6312–6322, 2014.

[15] S. Stucci, M. Tucci, A. Passarelli, and F. Silvestris, "$\alpha_v\beta_3$ integrin: Pathogenetic role in osteotropic tumors," *Critical Reviews in Oncology/Hematology*, vol. 96, no. 1, pp. 183–193, 2015.

[16] J. G. Schneider, S. R. Amend, and K. N. Weilbaecher, "Integrins and bone metastasis: Integrating tumor cell and stromal cell interactions," *Bone*, vol. 48, no. 1, pp. 54–65, 2011.

[17] J. Caers, U. Günthert, H. De Raeve et al., "The involvement of osteopontin and its receptors in multiple myeloma cell survival, migration and invasion in the murine 5T33MM model," *British Journal of Haematology*, vol. 132, no. 4, pp. 469–477, 2006.

[18] A. Iagaru, E. Mittra, S. S. Yaghoubi et al., "Novel strategy for a cocktail ^{18}F-fluoride and ^{18}F-FDG PET/CT scan for evaluation of malignancy: results of the pilot-phase study," *Journal of Nuclear Medicine*, vol. 50, no. 4, pp. 501–505, 2009.

[19] S. C. Sampath, S. C. Sampath, C. Mosci et al., "Detection of osseous metastasis by ^{18}F-NaF/^{18}F-FDG PET/CT versus CT alone," *Clinical Nuclear Medicine*, vol. 40, no. 3, pp. e173–e177, 2015.

[20] N. Withofs, F. Cousin, T. Tancredi, Simoni P., De Prijck B., Hafraoui K. et al., "Comparison of combined whole-body [^{18}F]NaF and [^{18}F]FDG PET/CT versus MRI for the detection of myeloma lesions," *Journal of Nuclear Medicine*, vol. 57, supplement 2, article 606, 2016.

[21] C. Sachpekidis, J. Hillengass, H. Goldschmidt et al., "Treatment response evaluation with ^{18}F-FDG PET/CT and ^{18}F-NaF PET/CT in multiple myeloma patients undergoing high-dose chemotherapy and autologous stem cell transplantation," *European Journal of Nuclear Medicine and Molecular Imaging*, vol. 44, no. 1, pp. 50–62, 2017.

[22] E. Otjacques, M. Binsfeld, A. Noel, Y. Beguin, D. Cataldo, and J. Caers, "Biological aspects of angiogenesis in multiple myeloma," *International Journal of Hematology*, vol. 94, no. 6, pp. 505–518, 2011.

[23] L. Rasche, E. Angtuaco, J. E. McDonald et al., "Low expression of hexokinase-2 is associated with false-negative FDG–positron emission tomography in multiple myeloma," *Blood*, vol. 130, no. 1, pp. 30–34, 2017.

[24] M. Tucci, S. Stucci, C. Felici et al., "Cilengitide restrains the osteoclast-like bone resorbing activity of myeloma plasma cells," *British Journal of Haematology*, vol. 173, no. 1, pp. 59–69, 2016.

Hindawi
Contrast Media & Molecular Imaging
Volume 2017, Article ID 2709547, 14 pages
https://doi.org/10.1155/2017/2709547

Review Article

CD44v6-Targeted Imaging of Head and Neck Squamous Cell Carcinoma: Antibody-Based Approaches

Diana Spiegelberg[1] and Johan Nilvebrant[2]

[1]*Department of Immunology, Genetics and Pathology, Uppsala University, Uppsala, Sweden*
[2]*Division of Protein Technology, School of Biotechnology, Royal Institute of Technology, Stockholm, Sweden*

Correspondence should be addressed to Diana Spiegelberg; diana.spiegelberg@igp.uu.se
and Johan Nilvebrant; johan.nilvebrant@biotech.kth.se

Received 24 February 2017; Revised 23 April 2017; Accepted 21 May 2017; Published 20 June 2017

Academic Editor: Shasha Li

Head and neck squamous cell carcinoma (HNSCC) is a common and severe cancer with low survival rate in advanced stages. Noninvasive imaging of prognostic and therapeutic biomarkers could provide valuable information for planning and monitoring of the different therapy options. Thus, there is a major interest in development of new tracers towards cancer-specific molecular targets to improve diagnostic imaging and treatment. CD44v6, an oncogenic variant of the cell surface molecule CD44, is a promising molecular target since it exhibits a unique expression pattern in HNSCC and is associated with drug- and radio-resistance. In this review we summarize results from preclinical and clinical investigations of radiolabeled anti-CD44v6 antibody-based tracers: full-length antibodies, Fab, $F(ab')_2$ fragments, and scFvs with particular focus on the engineering of various antibody formats and choice of radiolabel for the use as molecular imaging agents in HNSCC. We conclude that the current evidence points to CD44v6 imaging being a promising approach for providing more specific and sensitive diagnostic tools, leading to customized treatment decisions and functional diagnosis. Improved imaging tools hold promise to enable more effective treatment for head and neck cancer patients.

1. Introduction

1.1. Head and Neck Cancer. The term head and neck cancer summarizes malignancies of diverse origins, such as oral cavity, sinonasal cavity, salivary glands, pharynx, larynx, and lymph nodes in the head and neck. In spite of this diversity, the majority (about 95%) of head and neck cancers are squamous cell carcinomas (HNSCC) that arise from epithelial cells. HNSCC represents the sixth leading cause of cancer worldwide and results in approximately 0.5 million new diagnoses and approximately 0.3 million deaths annually [1]. Thus, HNSCC is a common cancer with low survival rate in advanced stages.

Important risk factors for head and neck cancers in Western countries include use of tobacco or alcohol and poor dietary intake. In many Asian countries, parts of East Africa, and the tropical Pacific, chewing areca or betel nuts and smoking bidis are contributing factors [2]. Moreover, exposure to Epstein-Barr virus (EBV) has been implicated in nasopharyngeal and hypopharyngeal carcinoma and infections with human papillomavirus (HPV), a causative agent of genital and anal cancers, can be a risk factor in developing oropharyngeal HNSCC [3, 4]. HPV-related HNSCCs are more frequent in young male adults and are generally associated with better outcome. In recent years, the incidence rate of HPV-associated HNSCC has increased rapidly while that of tobacco-associated HNSCC has declined, the latter of which is probably correlated to a general trend of fewer heavy smokers [3, 4].

The current multiple-modality treatment options with surgery, radiation, and chemotherapy are effective in early-stage disease and often curative. However, considering the delicate areas of face, head, and neck, treatment is associated with severe adverse outcomes, for example, on appearance and facial expression or on speech and swallowing function, which can substantially lower the quality of life. Moreover,

a majority of HNSCC patients present with high-grade histology and with metastases located primarily in regional lymph nodes in the neck area. Despite recent advances in the use of chemotherapy with radiation and the use of hyperfractionated radiotherapy, advanced-stage HNSCC is still difficult to cure and the overall five-year survival rate is below 40–50% [4]. The low survival rate has been linked to high local recurrence rates, emergence of second primary disease, and development of distant metastases [9]. Earlier and more precise diagnosis could improve these numbers dramatically. Thus, there is a high demand for improved functional and molecular diagnostic tools such as radioimmunotargeting techniques against HNSCC-specific biomarkers. This review focuses on antibody-based imaging probes targeting CD44v6, a cancer-related cell surface variant of CD44, which exhibits unique expression patterns in HNSCC and is a promising target for radioimmunotargeting.

1.2. Radioimmunodiagnostics. Today, TNM staging of malignant tumors (TNM refers to size of primary tumor, number of regional lymph nodes, and distant metastases involved) is the fundamental basis for diagnosis, treatment planning, and recovery as well as posttreatment assessment. Physical and intraoperative examination, X-ray tomography, and pathological assessment are commonly employed for staging [10]. However, molecular and functional studies of biological processes in real time as well as biomarker visualization and evaluation may provide important information that is unattainable with traditional techniques. Noninvasive nuclear medical imaging, magnetic resonance imaging and spectroscopy (MRI and MRS, resp.), optical imaging by, for example, near-infrared fluorescence, and ultrasound might improve the accuracy of tumor detection. These procedures are useful for a wide range of applications including diagnostics, drug discovery and development, theranostics, and personalized medicine. Traditionally, evaluation of disease has to a large extent been based on anatomical data without connection to the underlying biology. For instance, changes in tumor size are used as an indicator for treatment response according to response evaluation criteria in solid tumors (RECIST) [11]. However, this can be misleading in many ways, for example, when the main bulk of the tumor consists of nontumorigenic cells that are more easily killed or in assessment of drugs that stabilize disease. Therefore, alternative indicators for treatment response are needed, such as the precise measurement of expression level of therapeutic targets or biomarkers. This type of detailed information on a per-patient basis is a prerequisite for effective targeted cancer therapy. Moreover, it enables monitoring of the treatment response of the targeted molecular therapy since it allows for repetitive noninvasive assessments. Here, molecular and functional imaging techniques have many advantages because they permit the investigation of the whole tumor burden in the body, thereby allowing assessment of biomarker expression and heterogeneity of the disease.

Radioimmunodiagnostic imaging techniques, including positron emission tomography (PET) and single-photon emission computer tomography (SPECT), are most useful in combination with computerized tomography (CT) or MRI scans, often referred to as multimodality imaging, which enable morphological evaluation and colocalization of the tracer at a precise anatomical position [14, 15]. Important properties of a selection of radionuclides that can be used for nuclear imaging and therapy are summarized in Table 1. SPECT imaging uses targeting vectors labeled with radionuclides that emit gamma ray photons or high-energy X-ray photons (e.g., ^{99m}Tc, ^{111}In, and ^{177}Lu), with an energy range of 100–300 keV [16]. One photon is detected at a time by a single or a set of collimated radiation detectors. In PET imaging, radioisotopes that undergo positron emission decay can be used including ^{11}C, ^{18}F, ^{64}Cu, ^{68}Ga, ^{89}Zr, and ^{124}I [17–19]. Here, two oppositely directed (180°) 511 keV photons are emitted that can be registered by a circular scanner via coincident detection. By tracking the photons, computer simulations reconstruct 3D-images of the source of the annihilation. PET imaging has many advantages compared with SPECT, in particular a higher sensitivity and spatial resolution.

Today, ^{18}F is the most commonly used isotope for PET imaging and ^{18}F-fluorodeoxyglucose (^{18}F-FDG) has become the golden standard PET-tracer in nuclear medicine and molecular imaging. It is used to measure increased glucose uptake (metabolism) and is measured as a standardized uptake value (SUV). A high SUV indicates an area of highly proliferating tissues. ^{18}F-FDG PET/CT and PET/MRI are increasingly used in imaging of the head and neck area in order to add diagnostic information beyond pure anatomical data. Several clinical studies have compared the diagnostic performance of ^{18}F-FDG PET/CT with that of PET/MRI since the superb soft-tissue resolution of MRI was expected to be of particular benefit for evaluating head and neck cancer [20]. However, the sensitivity of PET/CT in this application was comparable to that of PET/MRI. More recently, molecular and functional imaging techniques have improved dramatically, and several direct alternatives to imaging by ^{18}F-FDG have been developed. One example is diffusion-weighted MRI, which can provide functional information based on direct measurement of the Brownian (random) motion of extracellular water molecules. This motion is restricted in hypercellular tumor tissue and quantified by a decrease in apparent diffusion coefficient. Changes in apparent diffusion coefficient values have also been linked with cell proliferation [10, 11] and to local tumor necrosis [21]. Another example is diffusion tensor imaging (DT MRI), which can be used to localize nerve bundles connected to malignant tissues and thereby potentially help guide surgery to better maintain the facial expression and communication abilities of the patient.

Although the diagnostic ability of PET/CT can be comparable to that of CT or MRI, depending on cancer type, ^{18}F-FDG PET/CT can more effectively be used in staging of nodal disease and finding distant metastases or a second primary tumor. Such findings can significantly alter therapy decision-making. However, increased ^{18}F-FDG uptake can also occur in nonmalignant areas due to posttreatment reactions, lymphadenitis, inflammation, and brown adipose tissue activation [22, 23]. Inflammation resulting from primary tumor

Table 1: *Properties of selected diagnostic and therapeutic radionuclides.* Some low abundance emissions have been omitted for clarity. β+: positron emission, γ: gamma ray emission, PET: positron emission tomography, and SPECT: single-photon emission computed tomography.

Radionuclide	Half-life	Decay mode	Energy (keV)	Max range in tissue	Major application
^{18}F	1.83 h	β+ (97%)	633		PET
^{11}C	20.4 min	β+ (99.8%)	960		PET
^{68}Ga	1.1 h	β+ (88%)	1899		PET
^{89}Zr	3.3 d	β+ (23%)	897		PET
^{64}Cu	12.7 h	β+ (17.8%)	653		PET
^{124}I	4.17 d	β+ (25%)	2138, 1534		PET
^{111}In	2.8 d	γ (90.6%), γ (94.1%)	171, 245		SPECT
^{99m}Tc	6.0 h	γ (89%)	140.5		SPECT
^{211}At	7.2 d	α (42%), γ (21%)	5868	0.8 mm	SPECT, radionuclide therapy
^{177}Lu	6.7 d	β– (78.6%), γ (11%), γ (6%)	498, 208, 113	1.6 mm	SPECT, radionuclide therapy
^{131}I	8.0 d	β– (89.9%), γ (81.7%)	606, 364	4 mm	SPECT, radionuclide therapy
^{225}Ac	9.9 d	α (50.7%)	5830	0.9 mm	Radionuclide therapy
^{90}Y	2.7 d	β– (99.9%)	2280	11 mm	Radionuclide therapy
^{89}Sr	50.5 d	β– (100%)	1491	7 mm	Radionuclide therapy
^{153}Sm	1.9 d	β– (44%), β– (34%)	702, 632	3.3 mm	Radionuclide therapy

ulceration or a recent biopsy can increase FDG uptake in lymph nodes and result in false-positive or equivocal activity. Similar problems occur at postsurgical sites, which are prone to inflammation especially after irradiation. Therefore it is important to find the right time frame for ^{18}F-FDG PET after radiation treatment (about 8–12 weeks after radiotherapy) to reduce false-positive results associated with inflammation [23].

Taken together, these problems highlight the need of novel diagnostic methods with the high sensitivity of ^{18}F-FDG-PET and increased tumor specificity. In HNSCC, targeted therapy or antibody-mediated diagnostic methods hold particular promise to improve early detection [24] and to treat minimal residual disease [25, 26].

1.3. Antibody-Based Molecular Imaging and Therapy. Therapeutic antibodies have been approved for several cancers. Cetuximab (Erbitux®), which is a monoclonal antibody (mAb) targeting epidermal growth factor receptor 1 (EGFR), was approved by the US Food and Drug Administration (USFDA) for treatment of local or regionally advanced HNSCC in 2006. When used in combination with radiation therapy, it was shown to exhibit a survival benefit over radiation therapy alone. In 2011 cetuximab was also approved together with chemotherapy for recurrent or metastatic HNSCC. More recently (in 2016) pembrolizumab (Keytruda®), an immune checkpoint inhibitor, was granted accelerated approval for recurrent and metastatic HNSCC. Promising initial results have also been obtained using another checkpoint inhibitor, nivolumab (Opdivo®), which was approved to treat patients with head and neck cancer a few months later. Bevacizumab (Avastin®), an antibody that blocks angiogenesis by binding to vascular endothelial growth factor A (VEGF-A), is being evaluated for use in locally advanced HNSCC [27].

Furthermore, antibody-based molecular imaging or immuno-PET is a promising strategy [28, 29]. This approach allows the combination of high sensitivity and high resolution of, for example, a PET-scanner with the tumor specificity of a tumor targeting antibody. Further advantages of radioimmunotargeting include the capability for monitoring therapy response, dosimetric calculations, and therapy [30].

Full-length antibodies (~150 kDa) or smaller antibody derivatives are the most studied molecules for nuclear imaging and radioimmunotherapy, and there are several advantages to their use as radioimmunotargeting agents. The primary factors are economical and relatively simple production techniques together with high affinity. One early problem in this field was severe immune reactions from, for example, murine monoclonal antibodies, which has now been overcome by use of humanization techniques or de novo generation of human antibodies via, for example, in vitro selection. The comparatively large size of antibodies results in long duration in the circulation during the targeting phase of the tumor and a slow clearance from the bloodstream, which is beneficial for radioimmunotherapy. In contrast, these properties may be suboptimal for radioimmunodiagnostics where smaller molecules with fast biodistribution are generally preferred. When choosing radionuclide species to couple to the mAb, the choice is highly dependent on the antibody used, properties of its antigen, and what targeting concept is intended. The most important factors are decay half-life, availability, cost, and chemical nuclide properties for compatibility with the targeting vehicle (Table 1). Especially for targeted radioimmunotherapy, the radiation type, conjugate properties, and target tumor size must be taken into consideration. Generally, the most used radionuclides in targeted radioimmunotherapy are β-emitters, but α-emitters and Auger electron-emitting radionuclides can be used as well.

A recent review lists about 30 ongoing clinical trials evaluating the utility of antibody-based PET tracers using USFDA-approved and/or experimental antibodies in various cancer types, including glioblastoma, esophagogastric, breast, prostate, and colorectal cancer [28]. These probes target VEGF-A (bevacizumab), PGF (RO5323441), HER2 (trastuzumab), PSMA (Df-IAB2M, HuJ591), STEAP1 (MSTP2109A), MSLN (MMOT0530A), or EGFR (cetuximab) among others. Generally, cell surface receptors that are exclusively expressed by tumor cells are suitable targets for radioimmunodiagnostics. There are several promising receptors for radioimmunodiagnostics in head and neck cancer such as EGFR or isoforms of CD44. EGFR is one of the most ubiquitously overexpressed receptors with an increased expression level in more than 80% of cases. Molecular imaging using radiolabeled anti-EGFR antibody-based probes is therefore highly interesting and currently under clinical and preclinical investigation [31, 32]. However, clinical visualization of EGFR has not been very successful due to EGFR expression in nontumor tissues. For example ^{99m}Tc-EC cetuximab (C225) or ^{89}Zr-cetuximab showed a rather high uptake in liver as well as uneven distribution within the patient without an evident specific uptake of the tracer within the tumor [33, 34]. Although the incidence of distant metastases in HNSCC is relatively small in comparison to other cancer types, one of the major metastatic sites of HNSCC is the liver [35], which therefore complicates imaging with EGFR targeting probes.

Another promising target for radioimmunodiagnostics of HNSCC is CD44v6, an oncogenic splice variant of the cell surface receptor CD44. CD44v6 is currently the most established tumor antigen among the CD44 splice variants, with a large expression difference between healthy and malignant tissue, which is a key advantage for molecular imaging. In contrast to EGFR expression, CD44v6 expression in organs for distant metastases of HNSCC, such as the liver, is negligible.

1.4. CD44 and CD44v6. CD44 is one of the major receptors for the glycosaminoglycan hyaluronan, which is an abundant component of the extracellular matrix. However, CD44 also interacts with collagen, laminin, fibronectin, and cytokines and has been suggested to function as a coreceptor for numerous transmembrane proteins, for example, growth factor receptors [36, 37]. Additionally, CD44 expression has been linked to stem cell-like properties as well as tumor progression, cell migration, invasion, metastasis, and poor response to chemo- and radiotherapy [38–43].

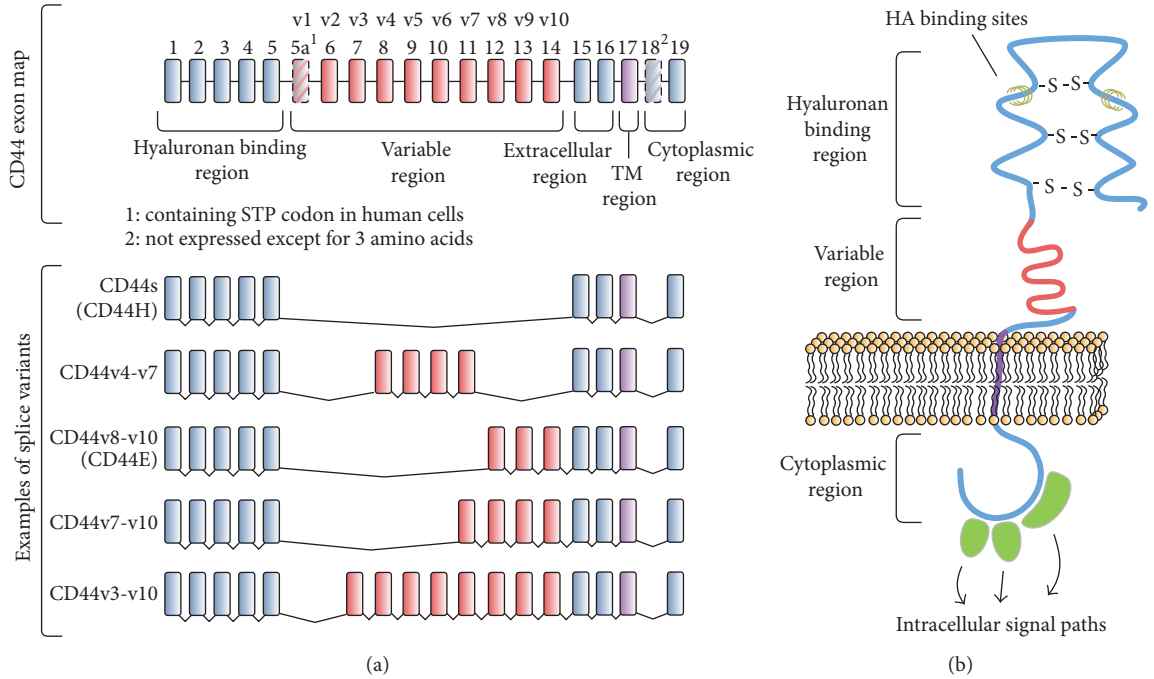

Figure 1: *CD44*. (a) Gene map of CD44. Standard CD44 (CD44s) does not contain variable exons. Exons v1–v10 are alternatively spliced. (b) Schematic overview of CD44. CD44 is a transmembrane protein, which consists of a cytoplasmic and extracellular region with hyaluronan binding sites and a variable region. HA: hyaluronic acid; TM: transmembrane region.

A single gene on chromosome 11p13 encodes CD44, which consists of 20 exons. Differential expression can give rise to a large number of CD44 isoforms. The standard form, referred to as CD44s (or CD44H, due to localization in hematopoietic cells), is the smallest and most abundant member of this large and heterogeneous family of multifunctional glycoproteins and is encoded by exons 1–5 and 15–20. The ten variably expressed exons that are lacking in CD44s are referred to as CD44v1-10 or exons 5a-15 in standard nomenclature [39] (Figures 1(a) and 1(b)). In humans, exon v1 contains a stop codon and no isoform containing this exon has been observed. Single exons or combinations of exon v2 to v10 can be inserted into the mRNA via alternative splicing translating into variations within the extracellular domain, which results in numerous protein variants. Furthermore, a multitude of posttranslational modifications, such as N- and O-glycosylation or palmitoylation, can further increase the diversity of CD44 gene products [44].

In humans, 19 different splice variants, the roles of which are not fully understood, have been identified at various expression levels in different tissues [45]. One example is CD44v7-v10 (CD44E), which is associated with normal epithelial cells. Several studies have associated certain CD44 splice variants with tumor cell invasion, metastasis, and disease progression, in particular isoforms containing CD44 exon variant 6 (CD44v6). Further studies have demonstrated high CD44v6 expression in several cancers, including breast, gastrointestinal, hepatocellular, and colorectal cancer and HNSCC [36, 42, 46, 47].

Overexpression of CD44v6 has been shown in squamous cell carcinomas, for example, in head and neck, lung, skin, esophagus, and cervix cancer [46]. However, CD44v6 expression frequencies vary throughout literature due to different detection methods (on RNA or protein level), different scoring systems, and the use of inapplicable antibodies [46]. However, overexpression of CD44v6 has been observed in over 90% of primary and metastatic HNSCC [44, 48]. Since CD44v6 is involved in progression of the disease and associated with radio-resistance, it is also an attractive therapeutic target [25]. Identifying differentially expressed diagnostic targets that are also involved in disease progression opens for theranostic applications, which combine diagnostic imaging with therapy by delivering therapeutic drugs and imaging vectors simultaneously [40]. Thus, monitoring of the disease can be followed by personalized treatment utilizing the same agent. Therapeutic radionuclides that can be used for molecular imaging, for example, ^{177}Lu, are of particular interest in this approach [49, 50].

1.5. Antibody-Based Targeting of CD44v6. Due to the high and homogenous expression of CD44v6 in HNSCC, antibodies recognizing this antigen have considerable potential for diagnosis and therapy [26]. In early studies, coinjection of a CD44v6-specific antibody together with metastatic cells was shown to retard or block metastatic spread in vivo [51, 52], which prompted the generation of antibodies specific for human CD44v6 [46]. U36 and BIWA 1 represent broadly used anti-CD44v6 mAbs and their encouraging targeting

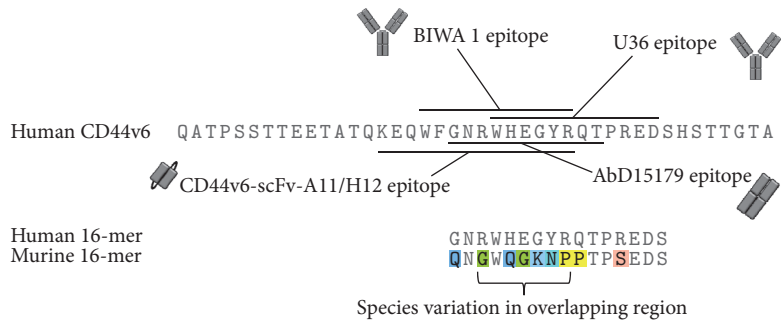

Figure 2: *Amino acid sequence of the human CD44v6 exon and antibody epitopes*. Antibodies U36 and BIWA 1 target overlapping epitopes in the v6 region [5, 6]. Recombinant Fab-fragment AbD15179 was generated using a peptide that overlaps with the epitopes of U36 and BIWA 1 [7]. CD44v6-specific scFvs recognize an epitope in the same region (Haylock et al. [8]). It is noticeable that murine CD44v6 has a low homology with the human sequence in the region where common antibody epitopes overlap, which is indicated in the alignment of a 14-residue region from the two species.

abilities have inspired more recent antibody engineering efforts.

mAb U36 was selected from a panel of antibodies generated by immunization of mice with human HNSCC cells followed by generation of hybridoma clones [53]. Based on immunohistochemical staining of HNSCC tumors, U36 appeared to be the most promising antibody for targeting of CD44v6 with a stronger and more specific staining pattern relative to the best currently available mAb (E48) [54]. U36 recognizes a linear epitope in the v6 region of CD44v6 positive isoforms without cross-reactivity to murine CD44v6 [6, 53, 55], which has a low sequence homology in the targeted region (Figure 2). Radiolabeled U36 was shown to have high potential for in vivo targeting of HNSCC xenografts in mice as well as in human patients (Figure 3) [53, 56]. These promising data inspired a radioimmunotherapy (RIT) trial for the treatment of minimal residual disease in patients with head and neck cancer using ^{186}Re-labeled chimeric (cmAb) U36 [13], in which the variable domains were transferred to a human IgG1 framework by previously developed strategies used for mAb E48 [57]. Radiolabeled cmAb U36 was well tolerated and displayed excellent targeting of tumor lesions. Moreover, stable disease and reduced tumor size were observed in some patients. However, the chimeric antibody still induced human antibody responses, which is an important consideration when repeated dosing is required for, for example, scouting studies prior to therapy.

Depending on the type of radionuclide chosen and the properties of the antibody-based targeting molecule, direct and indirect radiolabeling methods can be applied. Radioiodination with ^{123}I, ^{131}I, or ^{124}I as well as, for example, radiolabeling of ^{11}C compounds can be prepared by isotopic substitution, a direct exchange of stable atoms with radioisotopes of the same element. However, a majority of radiopharmaceuticals are prepared by introduction of a foreign element, as, for instance, for ^{18}F-FDG where an ^{18}F atom is introduced into the deoxyglucose molecule. Antibody-based targeting molecules can also be labeled with radiometals, for example, with ^{99m}Tc or ^{111}In, using the metal chelation method. For some probes a bifunctional chelate has to be introduced prior chelation of the radiometal. In this case, the radiometal is not directly incorporated into the molecule.

A large number of studies have demonstrated successful direct and indirect radiolabeling and use of mAb U36, its chimeric derivative, or smaller U36-derived antibody fragments in vitro and in vivo using, for example, ^{88}Y [58], ^{89}Zr [59], ^{99m}Tc [56], ^{111}In [60], ^{124}I [61], ^{125}I [62, 63], ^{131}I [61], ^{177}Lu [60], or ^{211}At [64]. Thus, a diversity of labeling strategies and nuclides is available to fine-tune labeling, half-life, and dosimetry (e.g., estimation of radiation dose delivery to tumor and normal tissue) for applications in imaging or therapy. HNSCC is intrinsically radiosensitive, which may favor radioimmunotherapy. ^{186}Re has been suggested to be better suited than ^{131}I for RIT due to its lower gamma emission and higher conjugate stability. Labeling with ^{186}Re using S-benzoyl mercaptoacetyltriglycide on lysine residues of the antibody [65] has been systematically evaluated. Adding too many payloads per antibody (>8) compromised immunoreactivity and resulted in faster clearance [66]. These results were later confirmed in a clinical study [67].

mAb BIWA 1, which was initially called VFF18, was generated by immunization of mice with recombinant CD44v3–v10 protein [5]. ELISA screening of hybridoma supernatants was used to identify CD44v6-specific mAbs and BIWA 1 was selected based on high affinity and specificity for human tumor cells in immunohistochemistry. Synthetic peptides were used to map the BIWA 1 epitope to a sequence that partially overlaps with the U36 epitope (Figure 2). In analogy with U36, binding was specific for human CD44v6 over its murine ortholog [5]. BIWA 1 was used for comprehensive immunohistochemical screening of tumor tissues, which demonstrated high and homogenous CD44v6 expression in a majority of analyzed tumors derived from squamous epithelium [5]. The same study demonstrated feasibility of targeting of CD44v6-expressing xenografts in mice using radiolabeled BIWA 1. Importantly, reactivity with normal human tissues was observed only on a subset of epithelial tissues but not on nonepithelial tissues [68]. As a first step towards human therapy, the safety, biodistribution,

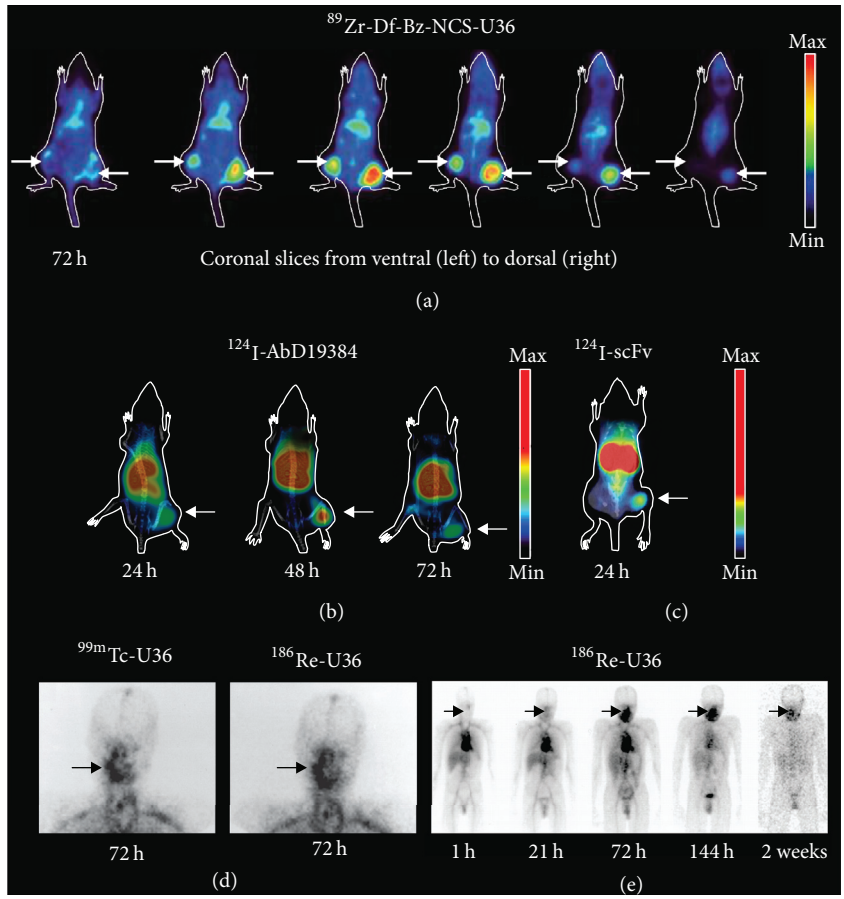

Figure 3: *Preclinical (a–c) and clinical (d–e) images of CD44v6 radionuclide targeting.* (a) Representative small animal PET images of a nude mouse bearing two head and neck cancer FaDu xenografts, obtained at 72 h after i.v. injection of the antibody conjugate ^{89}Zr–Df–Bz–NCS–cmAb U36 (reprinted and modified from Vosjan et al.) [12]. (b) Representative small animal PET/CT images of nude mice bearing a squamous cell carcinoma A431 xenograft, obtained at 24 h, 48 h, and 72 h after i.v. injection of the human bivalent antibody fragment ^{124}I-AbD19384. (c) Representative small animal PET/CT image of a nude mice bearing a squamous cell carcinoma A431 xenograft, obtained at 24 h after i.v. injection of an anti-CD44v6 targeting scFv fragment. (d) Planar imaging of head and neck region of a HNSCC patient 21 h after i.v. injection of the antibody conjugates ^{99m}Tc-cmAb U36 (left) and ^{186}Re-cmAb U36 (right) (reprinted and modified from Colnot et al. J. Nucl. Med. 2000) [13]. (e) Whole-body scans of a HNSCC patient 1 h, 21 h, 72 h, 144 h, and 2 weeks after i.v. injection of the antibody conjugate ^{186}Re-cmAb U36 (reprinted and modified from Colnot et al. J. Nucl. Med. 2000) [13].

and tumor targeting potential of ^{99m}Tc-labeled BIWA 1 were evaluated in HNSCC patients [69]. The results indicated that this antibody could be safely administered and achieve high and specific uptake in tumors, which enabled visualization already at time points before optimal tumor to nontumor ratios could be achieved. Similar tumor uptake at a higher and lower dose indicated that the high affinity of BIWA 1 might restrict tumor distribution as a result of saturation at a binding site barrier. In contrast, U36 displayed more homogenous distribution within the tumor at higher doses [56], which may be attributed to the ca. 35-fold lower affinity of U36 compared to BIWA 1 [48, 69].

1.6. Humanization and Evaluation of Drug Conjugated Antibodies. Immunogenicity of the murine BIWA 1, which is linked to rapid clearance and allergic reactions, spurred the development of a humanized variant called BIWA 4 for further studies. Moreover, the high affinity mAb BIWA 1 showed complex formation with soluble CD44v6 in the blood and heterogeneous tumor uptake, which suggested that a lower affinity might be beneficial. Interestingly, a comparison of U36, BIWA 1, a chimeric antibody and two humanized variants of BIWA 1 designated BIWA 2, BIWA 4, and BIW 8, respectively, revealed that lower affinity mAbs displayed superior tumor targeting capacities in mouse xenograft models [48]. Thus, the intermediate affinity, humanized mAb BIWA 4 (bivatuzumab), was selected for further clinical development over the higher affinity variant BIWA 8. In a following study on HNSCC patients, administration of ^{99m}Tc-labeled BIWA 4 was well tolerated and no human anti-human antibody [35] responses were observed [70], which can be compared to a HAMA response in ca. 90% of patients treated with the parental murine BIWA 1. An intermediate dose level of 50 mg gave the highest tumor uptake and tumor to nontumor ratios. The lack of immunogenicity of BIWA 4 supported multiple administrations for radioimmunotherapy,

which was evaluated in dose escalation studies using ^{186}Re-labeled BIWA 4 on patients with advanced HNSCC [71, 72] as well as in patients with early-stage breast cancer [73]. Although radiolabeled BIWA 4 could be safely administered in all studies with tolerable side effects and only a few reported HAHA-responses, the results showed that uptake ratios were unfavorable in the breast cancer study. Thus, HNSCC remained the indication in focus for bivatuzumab due to a more favorable biodistribution likely resulting from higher and more specific expression of CD44v6 in HNSCC.

Although it was not the primary study objective, phase I RIT studies using ^{186}Re-labeled cmAb U36 or BIWA 4 showed promising antitumor effects with consistent stable disease at higher dose levels [74]. At the time the first antibody-drug conjugate (ADC), gemtuzumab ozogamicin (Mylotarg®) that targets CD33, had already been approved for the treatment of amyloid myeloid leukemia. An ADC combines the targeting capability of an antibody with a cytotoxic payload with cancer-killing ability. Hence, it was envisioned that coupling of BIWA 4 to a cytotoxic drug instead of a radionuclide might provide a more effective immunoconjugate for adjuvant therapy of HNSCC. Mertansine (also called DM1) is a derivative of the antimicrotubule agent maytansine with more than 100-fold higher cytotoxic activity compared to other clinically used anticancer drugs such as anthracyclines or taxanes [75]. The antibody-drug conjugate was designed to release and activate the cytotoxic, disulfide-linked, part upon cellular internalization. Initial preclinical evaluation in animals demonstrated dose-dependent efficacy with long-lasting tumor regression of mertansine conjugated to bivatuzumab (BIWI 1 or bivatuzumab mertansine) whereas no effects were seen on tumor growth for the unconjugated antibody [74, 76]. However, in spite of promising results in several studies, death of one patient from drug related toxic epidermal necrolysis during a phase I dose-escalating study led to premature termination of the study [74, 76]. Arguably, expression of CD44v6 is not sufficiently selective for tumor cells to allow systematic administration of antibody conjugates containing highly toxic agents like mertansine or the linker was not sufficiently stable to prevent exposure to nontumor tissue [76]. Interestingly, bivatuzumab mertansine improved local tumor control with acceptable systemic toxicity in a murine model when administered at a lower dose in combination with fractionated irradiation [77]. Furthermore, one of only two currently approved ADCs, for example, trastuzumab emtansine (Kadcyla®), utilizes the same toxin with a noncleavable linker. It is also noteworthy that gemtuzumab ozogamicin, the first ADC to be approved, was withdrawn from market in 2010 when a large study failed to demonstrate that it extended survival over conventional therapy and was associated with a high rate of fatal toxicity (USFDA). Taken together, this illustrates that while the concept of ADCs is relatively straightforward, the design of a functional and effective antibody-drug conjugate is very challenging.

In spite of advances in therapeutic intervention, the early detection of cancers is still important to improve the clinical outcome for cancer patients. Diagnostic use of radiolabeled antibodies can tolerate expression of the target antigen in normal tissues, especially in an area outside of the anatomical region of interest or in normal tissue that is poorly accessible to antibodies [25]. Several radioimmunoconjugates have been approved for cancer diagnosis, for example, arcitumomab (CEA-scan®), a ^{99m}Tc-labeled antibody fragment used for imaging of colorectal cancer, and capromab pendetide (ProstaScint®), an ^{111}In-labeled mAb directed against prostate specific membrane antigen (PSMA) [78]. In the case of CD44v6-targeting in HNSCC, selection of an appropriate radioimmunoconjugate may also help overcoming treatment-related skin toxicity [26]. The promises of radioimmunodiagnostics and recent advances in antibody engineering have inspired the development of a new generation of antibodies targeting CD44v6.

1.7. Recombinant Antibodies and Antibody Engineering. The high immunogenicity and weak interaction with human complement and Fcγ receptors of murine antibodies generally translate into a low success rate in medical development [79]. Using recombinant DNA technology, chimeric antibodies, which consist of human constant domains with murine variable regions (e.g., rituximab, Rituxan®; 2006) and humanized antibodies, where mainly the complementarity determining regions (CDRs) are of nonhuman origin (e.g., daclizumab, Zinbryta®; 2003), can be generated. However, these hybrid antibodies still carry foreign sequence in their antigen-binding loops, which may lead to immunogenicity as exemplified by the HAHA-responses observed in two patients in a phase I therapy study using ^{186}Re-labeled BIWA 4 [71]. Moreover, humanized antibodies frequently loose binding affinity in the process of loop grafting or framework engineering. Human mAbs are defined as having variable domains that are entirely derived from human antibody repertoires. Adalimumab (Humira®) was the first fully human antibody to be approved for human therapy in 2002. It was generated by in vitro display without animal immunization or hybridoma technology. Display methods physically link an antibody fragment to its encoding DNA and thereby enable screening of libraries containing billions of variants in vitro (Figure 4). Rounds of selection and amplification are employed to enrich antigen-binding clones with desired properties. The sequences of promising variants are immediately available, which facilitates further engineering of antibody properties including affinity, valency, and stability. In vitro selection has several advantages over traditional immunization-based antibody generation. It enables full control over the selection conditions and the epitopes that are targeted. For example, alternating selection on orthologs of relevance for future testing in animal models can be applied to isolate clones that display cross-species binding. In contrast, since antibodies that are reactive to self are eliminated, it is almost impossible to raise antibodies against epitopes that are highly conserved across species using immunization. Today, most antibodies that enter clinical trials are completely human and are derived from phage display technology or transgenic mice, which have been engineered to carry human antibody repertoires [80–82].

Antibody fragments are commonly used in the engineering of antibody properties and have an increasing clinical

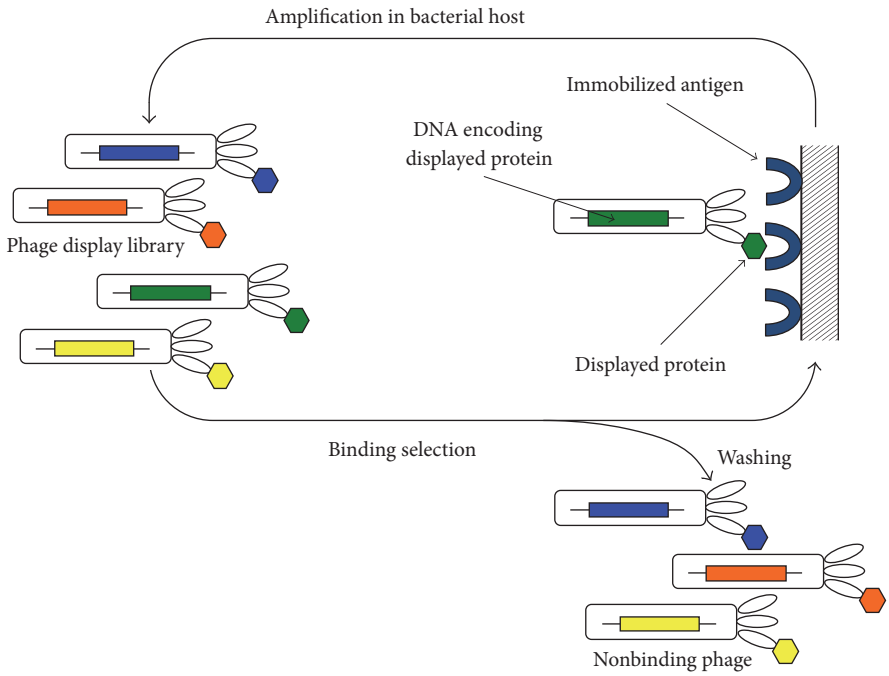

Figure 4: *Phage display selection from a protein library*. Protein libraries are displayed on phage particles as fusions to coat proteins. Each phage displays a unique protein and encapsulates the encoding DNA, which links the genotype and phenotype of the displayed protein. Protein variants (e.g., antibodies) that bind an immobilized antigen are isolated through rounds of binding selection and amplification. Nonbinding phages are removed by washing. Retained phages are recovered, amplified by bacterial infection, and cycled through additional rounds of selection. Compared to immunization-based methods, in vitro selection enables full control of library design and selection conditions. Binding clones are identified through sequencing of the encapsulated DNA.

importance [83]. The fragment antigen-binding (Fab) is a heterodimer consisting of the light chain and the variable and first constant domains of the heavy chain. A single chain fragment variable (scFv) consists of the light and heavy variable domains connected by a linker. Fabs are generally more stable than scFvs and activity is better retained upon conversion to full-length IgG. Single domain formats derived from variable [84, 85] or constant domains [86, 87] represent the smallest human antibody fragments. Building on the modular architecture of antibodies, many innovative formats with diverse valences and antigen-binding specificities have been constructed [88].

Using phage display we have isolated CD44v6-binding fully human Fab fragments that bind a defined peptide that overlaps with the epitopes of U36 and BIWA 1 [7] (Figure 2). Fab AbD15179 was selected as a lead candidate among eight clones derived from the HuCAL Platinum synthetic antibody library [89]. All selected antibodies displayed competition with U36, which indicated that the epitope-guided selection was successful. AbD15179 specifically recognized a CD44v6-positive isoform with low nanomolar affinity without measurable cross-reactivity to CD44v6-negative controls [7]. The in vivo targeting properties of radiolabeled AbD15179 were evaluated in tumor-bearing mice [90]. In general, Fab fragments exhibit shorter half-life, faster blood clearance, and better tumor to background ratios compared to full-length antibodies and are thus promising for tumor imaging applications. The human Fab had a favorable biodistribution and could discriminate between high and low CD44v6 expressing tumors in vivo. Notably, the labeling approach can influence the kinetic properties of the antibody conjugate. This was demonstrated for AbD15179 using different squamous cell carcinoma cell lines [91] and highlights the importance of functional assessment of the radioimmunoconjugate. Reformatting AbD15179 into a bivalent construct followed by radiolabeling resulted in a tracer (^{124}I-AbD19384) with slower target dissociation that displayed more favorable tumor imaging properties when compared to ^{18}F-FDG PET (Figure 3) [92]. Similar results speaking in favor of a smaller bivalent antibody fragment were obtained when a Fab, a bivalent F(ab′)$_2$, and a full-length version of mAb U36 were compared side by side in vitro and in mice carrying CD44v6-expressing xenografts [63].

More recently we have generated a panel of scFvs that target an epitope that overlaps with Fab AbD15179 (Haylock et al. [8], Figure 2). CD44v6-specific scFvs were selected by phage display with negative selection on a CD44v6-negative isoform of CD44, which represented more ubiquitously expressed CD44 isoforms. V_H domains from CD44v6-specific first generation clones were next combined with a naïve V_L repertoire followed by stringent selection of high affinity clones. Two top candidates denoted CD44v6-scFv-A11 and CD44v6-scFv-H12 demonstrated specific binding to CD44v6-expressing cells in vitro with subnanomolar affinity. Both variants were radiolabeled using ^{111}In or ^{125}I and their tumor targeting abilities evaluated in tumor-bearing

mice. Radiolabeled scFvs, in particular ^{125}I-labeled fragments, provided high tumor-to-blood ratios and kinetics suitable for molecular imaging. Compared to, for example, Fab fragments, smaller antibody fragments like scFvs are expected to provide better imaging contrast as a result of a faster biodistribution and enhanced tissue penetration [78]. Despite the improved penetration of smaller fragments, the total tumor uptake is generally lower compared to full-length antibodies due to the shorter time in circulation. However, faster clearance and shorter circulation times are beneficial for tumor to organ ratio and contrast in molecular imaging. The smaller size of scFvs versus, for example, $F(ab')_2$ combined with high affinity monovalent binding yielded advantageous tumor to organ ratios already at 24 h p.i. (Haylock et al. [8]), which is half the time required to reach similar ratios for the $F(ab')_2$ fragment [92]. For imaging, the contrast between tumor and surrounding tissue is more important than the total tumor uptake and a high affinity is generally advantageous for radioimmunodiagnostic applications [25].

Several recent studies have reported on CD44v6-targeting antibody reagents. For example, human scFvs recognizing CD44v6 were isolated by phage display from a synthetic antibody library [93]. Using a similar strategy, Chen et al. selected CD44v6-binding scFvs from a library constructed from lymphocytes from human blood donors [94]. Interestingly, the single CD44v6-binding clone that was identified in this study was lacking the variable light domain. Thus, it will need more characterization of its biophysical properties and binding characteristics before it can be employed for, for example, tumor imaging in vivo. By immunizing mice with a 43-amino-acid region derived from v6 conjugated to a carrier protein, murine antibodies have also been generated [95]. However, in contrast to the antibodies generated in vitro by phage display, the sequences of these CD44v6 binders are unknown. Compared to other available CD44v6-binding recombinant antibodies, our Fab and scFv clones are more thoroughly characterized and have a demonstrated potential for tumor detection in vivo.

Antibodies targeting a v6-epitope have been shown to possess antitumor effects in vitro and in vivo [96–99], which imply that binding per se may promote a desirable phenotype. Intriguingly, these effects have been mapped to a three-residue peptide (RWH) [100] that is localized in the center of the mapped BIWA 1 epitope and also present in the epitopes recognized by our lead Fab and scFv clones (Figure 2).

2. Conclusion

CD44v6-positive isoforms have been related to aggressive tumor behavior and are abundantly expressed particularly in squamous cell carcinoma of the head and neck. In spite of improvements in locoregional treatment, the rate of recurrence is still close to 40%, whereas ca. 25% of these patients also develop distant metastases [74]. Autopsy studies have shown incidences of distant metastases in up to 57% of cases [25]. Thus, there is a demand for new tools for early-stage diagnosis to improve patient outcomes. In addition, advanced-stage HNSCC patients frequently harbor residual tumor cells after surgery and radiotherapy. The role of adjuvant chemotherapy for this group of patients is limited, and therefore the development of an effective adjuvant systemic treatment targeting distant micrometastases and minimal residual disease is another major challenge.

CD44v6-targeted antibody-mediated diagnosis and therapy hold promise to provide more tumor specific alternatives. Several antibodies have shown promise in CD44v6-targeting and promoted the development of bivatuzumab mertansine, an antibody-drug conjugate designed to kill CD44v6-expressing tumor cells. Although effective, a low antigen expression in normal epithelial cells combined with a highly toxic payload resulted in skin toxicity and termination of the development program. Nonetheless, the combination of high sensitivity and resolution of PET with the specificity and affinity of an anti-CD44v6 mAb makes immuno-PET an attractive tumor detection modality. To achieve optimal tumor to nontumor ratio, a labeling method and radionuclide with suitable half-life for adequate tumor accumulation and nonspecific clearance has to be selected. Combined with advances in antibody engineering that enable easier optimization of antibody format and targeting properties, this offers a promising approach to develop novel immunoconjugates. For example, affinity and specificity can be fine-tuned in vitro and antibodies can be engineered to tolerate labeling with minimal functional interference. Fully human antibodies, which are expected to be less immunogenic and better tolerated in repeated dosing, can be engineered without a need for unpredictable immunization-based methods.

Capitalizing on these technological developments, we have established a new generation of fully human antibody fragments against CD44v6 with promising tumor targeting properties in vivo. Several questions remain to be answered before these reagents can be employed for use in humans. For example, the lack of cross-reactivity with murine CD44v6 makes the transferability of preclinical findings in mouse models difficult to predict. Preclinical studies using monkeys, which have a higher sequence homology in the targeted region [68], may provide a more suitable animal model. Moreover, potential immunogenicity, particularly upon repeated administration, has to be evaluated more thoroughly.

Conflicts of Interest

The authors declare that there are no conflicts of interest regarding the publication of this paper.

Acknowledgments

The authors acknowledge Professor Guus van Dongen and Dr. Marika Nestor for generous guidance and advice.

References

[1] K. D. Miller, R. L. Siegel, C. C. Lin et al., "Cancer treatment and survivorship statistics, 2016," *CA Cancer Journal for Clinicians*, vol. 66, no. 4, pp. 271–289, 2016.

[2] S. Petti, "Lifestyle risk factors for oral cancer," *Oral Oncology*, vol. 45, no. 4-5, pp. 340–350, 2009.

[3] M. L. Gillison, G. D'Souza, W. Westra et al., "Distinct risk factor profiles for human papillomavirus type 16-positive and human papillomavirus type 16-negative head and neck cancers," *Journal of the National Cancer Institute*, vol. 100, no. 6, pp. 407–420, 2008.

[4] C. R. Leemans, B. J. Braakhuis, and R. H. Brakenhoff, "The molecular biology of head and neck cancer," *Nature Reviews Cancer*, vol. 11, no. 1, pp. 9–22, 2011.

[5] K.-H. Heider, M. Sproll, S. Susani et al., "Characterization of a high-affinity monoclonal antibody specific for CD44v6 as candidate for immunotherapy of squamous cell carcinomas," *Cancer Immunology Immunotherapy*, vol. 43, no. 4, pp. 245–253, 1996.

[6] N. L. Van Hal, G. A. Van Dongen, C. B. Ten Brink, J. N. Herron, G. B. Snow, and R. H. Brakenhoff, "Sequence variation in the monoclonal-antibody-U36-defined CD44v6 epitope," *Cancer Immunol Immunother*, vol. 45, no. 2, pp. 88–92, 1997.

[7] J. Nilvebrant, G. Kuku, H. Björkelund, and M. Nestor, "Selection and in vitro characterization of human CD44v6-binding antibody fragments," *Biotechnology and Applied Biochemistry*, vol. 59, no. 5, pp. 367–380, 2012.

[8] A.-K. Haylock, J. Nilvebrant, A. Mortensen, I. Velikyan, M. Nestor, and R. Falk, "Generation and evaluation of antibody agents for molecular imaging of CD44v6-expressing cancers," *Oncotarget*, 2017.

[9] A. Alvi and J. T. Johnson, "Development of distant metastasis after treatment of advanced-stage head and neck cancer," *Head Neck*, vol. 19, no. 6, pp. 500–505, 1997.

[10] S. G. Patel and J. P. Shah, "TNM staging of cancers of the head and neck: striving for uniformity among diversity," *CA: A Cancer Journal for Clinicians*, vol. 55, no. 4, pp. 242–258, 2005, quiz 261-242.

[11] M. Nishino, J. P. Jagannathan, N. H. Ramaiya, and A. D. Van Den Abbeele, "Revised RECIST guideline version 1.1: What oncologists want to know and what radiologists need to know," *American Journal of Roentgenology*, vol. 195, no. 2, pp. 281–289, 2010.

[12] M. J. Vosjan, L. R. Perk, G. W. Visser et al., "Conjugation and radiolabeling of monoclonal antibodies with zirconium-89 for PET imaging using the bifunctional chelate p-isothiocyanatobenzyl-desferrioxamine," *Nature Protocols*, vol. 5, no. 4, pp. 739–743, 2010.

[13] D. R. Colnot, J. J. Quak, J. C. Roos et al., "Phase I therapy study of 186Re-labeled chimeric monoclonal antibody U36 in patients with squamous cell carcinoma of the head and neck," *Journal of Nuclear Medicine*, vol. 41, no. 12, pp. 1999–2010, 2000.

[14] M. L. James and S. S. Gambhir, "A molecular imaging primer: modalities, imaging agents, and applications," *Physiological Reviews*, vol. 92, no. 2, pp. 897–965, 2012.

[15] R. Weissleder, "Molecular imaging in cancer," *Science*, vol. 312, no. 5777, pp. 1168–1171, 2006.

[16] E. B. Corcoran and R. N. Hanson, "Imaging EGFR and HER2 by PET and SPECT: A Review," *Medicinal Research Reviews*, vol. 34, no. 3, pp. 596–643, 2014.

[17] F. T. Lee and A. M. Scott, "Immuno-PET for tumor targeting," *Journal of Nuclear Medicine*, vol. 44, no. 8, pp. 1282-1283, 2003.

[18] T. K. Nayak and M. W. Brechbiel, "Radioimmunoimaging with longer-lived positron-emitting radionuclides: Potentials and challenges," *Bioconjugate Chemistry*, vol. 20, no. 5, pp. 825–841, 2009.

[19] Y. Zhang, H. Hong, and W. Cai, "PET tracers based on zirconium-89," *Current Radiopharmaceuticals*, vol. 4, no. 2, pp. 131–139, 2011.

[20] C. Spick, K. Herrmann, and J. Czernin, "18F-FDG PET/CT and PET/MRI perform equally well in cancer: Evidence from studies on more than 2,300 patients," *Journal of Nuclear Medicine*, vol. 57, no. 3, pp. 420–430, 2016.

[21] A. Varoquaux, O. Rager, K. O. Lovblad et al., "Functional imaging of head and neck squamous cell carcinoma with diffusion-weighted MRI and FDG PET/CT: quantitative analysis of ADC and SUV," *European Journal of Nuclear Medicine and Molecular Imaging*, vol. 40, no. 6, pp. 842–852, 2013.

[22] N. M. Long and C. S. Smith, "Causes and imaging features of false positives and false negatives on 18F-PET/CT in oncologic imaging," *Insights into Imaging*, vol. 2, no. 6, pp. 679–698, 2011.

[23] N. A. Plaxton, D. C. Brandon, A. S. Corey et al., "Characteristics and limitations of FDG PET/CT for imaging of squamous cell carcinoma of the head and neck: A comprehensive review of anatomy, metastatic pathways, and image findings," *American Journal of Roentgenology*, vol. 205, no. 5, pp. W519–W531, 2015.

[24] V. Radhakrishnan, M. S. Swanson, and U. K. Sinha, "Monoclonal antibodies as treatment modalities in head and neck cancers," *AIMS Medical Science*, vol. 2, no. 4, pp. 347–359, 2015.

[25] P. K. E. Börjesson, E. J. Postema, R. De Bree et al., "Radioimmunodetection and radioimmunotherapy of head and neck cancer," *Oral Oncology*, vol. 40, no. 8, pp. 761–772, 2004.

[26] M. V. Nestor, "Targeted radionuclide therapy in head and neck cancer," *Head and Neck*, vol. 32, no. 5, pp. 666–678, 2010.

[27] M. Yao, N. Galanopoulos, P. Lavertu et al., "Phase II study of bevacizumab in combination with docetaxel and radiation in locally advanced squamous cell carcinoma of the head and neck," *Head and Neck*, vol. 37, no. 11, pp. 1665–1671, 2015.

[28] J. M. Warram, E. De Boer, A. G. Sorace et al., "Antibody-based imaging strategies for cancer," *Cancer and Metastasis Reviews*, vol. 33, no. 2-3, pp. 809–822, 2014.

[29] J. Wedman, J. Pruim, J. L. N. Roodenburg et al., "Alternative PET tracers in head and neck cancer. A review," *European Archives of Oto-Rhino-Laryngology*, vol. 270, no. 10, pp. 2595–2601, 2013.

[30] P. Chames, M. van Regenmortel, E. Weiss, and D. Baty, "Therapeutic antibodies: successes, limitations and hopes for the future," *British Journal of Pharmacology*, vol. 157, no. 2, pp. 220–233, 2009.

[31] D. Spiegelberg, A. C. Mortensen, R. K. Selvaraju, O. Eriksson, B. Stenerlöw, and M. Nestor, "Molecular imaging of EGFR and CD44v6 for prediction and response monitoring of HSP90 inhibition in an in vivo squamous cell carcinoma model," *European Journal of Nuclear Medicine and Molecular Imaging*, vol. 43, no. 5, pp. 974–982, 2016.

[32] L. K. Van Dijk, O. C. Boerman, J. H. A. M. Kaanders, and J. Bussink, "PET imaging in head and neck cancer patients to monitor treatment response: A future role for EGFR-targeted imaging," *Clinical Cancer Research*, vol. 21, no. 16, pp. 3602–3609, 2015.

[33] N. R. Schechter, R. E. Wendt III, D. J. Yang et al., "Radiation dosimetry of 99mTc-labeled C225 in patients with squamous cell carcinoma of the head and neck," *Journal of Nuclear Medicine*, vol. 45, no. 10, pp. 1683–1687, 2004.

[34] J. van Loon, A. J. G. Even, H. J. W. L. Aerts et al., "PET imaging of zirconium-89 labelled cetuximab: A phase I trial in patients with head and neck and lung cancer," *Radiotherapy and Oncology*, vol. 122, no. 2, pp. 267–273, 2017.

[35] A. Ferlito, A. R. Shaha, C. E. Silver, A. Rinaldo, and V. Mondin, "Incidence and sites of distant metastases from head and neck cancer," *ORL J Otorhinolaryngol Relat Spec*, vol. 63, no. 4, pp. 202–207, 2001.

[36] R. Marhaba and M. Zöller, "CD44 in cancer progression: Adhesion, migration and growth regulation," *Journal of Molecular Histology*, vol. 35, no. 3, pp. 211–231, 2004.

[37] A. Perez, D. M. Neskey, J. Wen et al., "CD44 interacts with EGFR and promotes head and neck squamous cell carcinoma initiation and progression," *Oral Oncology*, vol. 49, no. 4, pp. 306–313, 2013.

[38] F. Bhaijee, D. J. Pepper, K. T. Pitman, and D. Bell, "Cancer stem cells in head and neck squamous cell carcinoma: a review of current knowledge and future applications," *Head & Neck*, vol. 34, no. 6, pp. 894–899, 2012.

[39] V. Orian-Rousseau and H. Ponta, "Perspectives of CD44 targeting therapies," *Archives of Toxicology*, vol. 89, no. 1, pp. 3–14, 2015.

[40] M. E. Prince, R. Sivanandan, A. Kaczorowski et al., "Identification of a subpopulation of cells with cancer stem cell properties in head and neck squamous cell carcinoma," *Proceedings of the National Academy of Sciences of the United States of America*, vol. 104, no. 3, pp. 973–978, 2007.

[41] S. H. Sahlberg, D. Spiegelberg, B. Glimelius, B. Stenerlöw, and M. Nestor, "Evaluation of cancer stem cell markers CD133, CD44, CD24: association with AKT isoforms and radiation resistance in colon cancer cells," *PLoS ONE*, vol. 9, no. 4, article e94621, 2014.

[42] D. Spiegelberg, G. Kuku, R. Selvaraju, and M. Nestor, "Characterization of CD44 variant expression in head and neck squamous cell carcinomas," *Tumor Biology*, vol. 35, no. 3, pp. 2053–2062, 2014.

[43] V. J. M. Wielenga, K.-H. Heider, G. J. A. Offerhaus et al., "Expression of CD44 variant proteins in human colorectal cancer is related to tumor progression," *Cancer Research*, vol. 53, no. 20, pp. 4754–4756, 1993.

[44] V. Orian-Rousseau, "CD44, a therapeutic target for metastasising tumours," *European Journal of Cancer*, vol. 46, no. 7, pp. 1271–1277, 2010.

[45] Uniprot Uniprot C., http://www.uniprot.org/uniprot/P16070.

[46] K.-H. Heider, H. Kuthan, G. Stehle, and G. Munzert, "CD44v6: a target for antibody-based cancer therapy," *Cancer Immunology, Immunotherapy*, vol. 53, no. 7, pp. 567–579, 2004.

[47] L. S. Monteiro, M. L. Delgado, S. Ricardo et al., "Prognostic significance of CD44v6, p63, podoplanin and MMP-9 in oral squamous cell carcinomas," *Oral Diseases*, vol. 22, no. 4, pp. 303–312, 2016.

[48] I. Verel, K.-H. Heider, M. Siegmund et al., "Tumor targeting properties of monoclonal antibodies with different affinity for target antigen CD44V6 in nude mice bearing head-and-neck cancer xenografts," *International Journal of Cancer*, vol. 99, no. 3, pp. 396–402, 2002.

[49] R. P. Baum and H. R. Kulkarni, "Theranostics: From molecular imaging using Ga-68 labeled tracers and PET/CT to personalized radionuclide therapy - the bad berka experience," *Theranostics*, vol. 2, no. 5, pp. 437–447, 2012.

[50] S. S. Kelkar and T. M. Reineke, "Theranostics: combining imaging and therapy," *Bioconjugate Chemistry*, vol. 22, no. 10, pp. 1879–1903, 2011.

[51] U. Günthert, M. Hofmann, W. Rudy et al., "A new variant of glycoprotein CD44 confers metastatic potential to rat carcinoma cells," *Cell*, vol. 65, no. 1, pp. 13–24, 1991 (Arabic).

[52] S. Seiter, R. Arch, S. Reber, D. Komitowski et al., "Prevention of tumor metastasis formation by anti-variant CD44," *Journal of Experimental Medicine*, vol. 177, no. 2, pp. 443–455, 1993.

[53] A. H. Schrijvers, J. J. Quak, A. M. Uyterlinde et al., "MAb U36, a novel monoclonal antibody successful in immunotargeting of squamous cell carcinoma of the head and neck," *Cancer Res*, vol. 53, no. 18, pp. 4383–4390, 1993.

[54] J. J. Quak, A. J. Balm, G. A. van Dongen et al., "A 22-kd surface antigen detected by monoclonal antibody E 48 is exclusively expressed in stratified squamous and transitional epithelia," *The American Journal of Pathology*, vol. 136, no. 1, pp. 191–197, 1990.

[55] NL. Van Hal, GA. Van Dongen, EM. Rood-Knippels, P. Van Der Valk, GB. Snow, and RH. Brakenhoff, "Monoclonal antibody U36, a suitable candidate for clinical immunotherapy of squamous-cell carcinoma, recognizes a CD44 isoform," *Int J Cancer*, vol. 68, no. 4, pp. 520–527, 1996.

[56] R. de Bree, J. C. Roos, J. J. Quak, W. den Hollander, G. B. Snow, and G. A. van Dongen, "Radioimmunoscintigraphy and biodistribution of technetium-99m-labeled monoclonal antibody U36 in patients with head and neck cancer," *Clinical Cancer Research*, vol. 1, no. 6, pp. 591–598, 1995.

[57] R. H. Brakenhoff, F. B. van Gog, J. E. Looney, M. van Walsum, G. B. Snow, and G. A. van Dongen, "Construction and characterization of the chimeric monoclonal antibody E48 for therapy of head and neck cancer," *Cancer Immunol Immunother*, vol. 40, no. 3, pp. 191–200, 1995.

[58] I. Verel, G. W. Visser, O. C. Boerman et al., "Long-lived positron emitters zirconium-89 and iodine-124 for scouting of therapeutic radioimmunoconjugates with PET," *Cancer Biother Radiopharm*, vol. 18, no. 4, Article ID 108497803322287745, pp. 655–661, 2003.

[59] I. Verel, G. W. Visser, R. Boellaard, M. Stigter-van Walsum, G. B. Snow, and G. A. van Dongen, "89Zr immuno-PET: comprehensive procedures for the production of 89Zr-labeled monoclonal antibodies," *J Nucl Med*, vol. 44, no. 8, pp. 1271–1281, 2003.

[60] M. Nestor, K. Andersson, and H. Lundqvist, "Characterization of 111In and 177Lu-labeled antibodies binding to CD44v6 using a novel automated radioimmunoassay," *Journal of Molecular Recognition*, vol. 21, no. 3, pp. 179–183, 2008.

[61] I. Verel, G. W. Visser, M. J. Vosjan, R. Finn, R. Boellaard, and G. A. van Dongen, "High-quality 124I-labelled monoclonal antibodies for use as PET scouting agents prior to 131I-radioimmunotherapy," *European Journal of Nuclear Medicine and Molecular Imaging*, vol. 31, no. 12, pp. 1645–1652, 2004.

[62] J. Cheng, M. Persson, V. Tolmachev et al., "Targeting of a head and neck squamous cell carcinoma xenograft model using the chimeric monoclonal antibody U36 radioiodinated with a closo-dodecaborate- containing linker," *Acta Oto-Laryngologica*, vol. 124, no. 9, pp. 1078–1085, 2004.

[63] K. Sandström, A. K. Haylock, D. Spiegelberg, F. Qvarnström, K. Wester, and M. Nestor, "A novel CD44v6 targeting antibody fragment with improved tumor-to-blood ratio," *International Journal of Oncology*, vol. 40, no. 5, pp. 1525–1532, 2012.

[64] M. Nestor, M. Persson, G. A. van Dongen et al., "In vitro evaluation of the astatinated chimeric monoclonal antibody U36, a potential candidate for treatment of head and neck squamous cell carcinoma," *Eur J Nucl Med Mol Imaging*, vol. 32, no. 11, pp. 1296–1304, 2005.

[65] G. W. Visser, M. Gerretsen, J. D. Herscheid, G. B. Snow, and G. van Dongen, "Labeling of monoclonal antibodies with rhenium-186 using the MAG3 chelate for radioimmunotherapy

of cancer: a technical protocol," *Journal of Nuclear Medicine*, vol. 34, no. 11, pp. 1953–1963, 1993.

[66] F. B. van Gog, G. W. Visser, R. Klok, R. van der Schors, G. B. Snow, and G. A. van Dongen, "Monoclonal antibodies labeled with rhenium-186 using the MAG3 chelate: relationship between the number of chelated groups and biodistribution characteristics," *Journal of Nuclear Medicine*, vol. 37, no. 2, pp. 352–362, 1996.

[67] F. B. van Gog, G. W. Visser, J. W. Stroomer, J. C. Roos, G. B. Snow, and G. A. van Dongen, "High dose rhenium-186-labeling of monoclonal antibodies for clinical application: pitfalls and solutions," *Cancer*, vol. 80, supplement 12, pp. 2360–2370, 1997.

[68] K.-H. Heider, J.-W. R. Mulder, E. Ostermann et al., "Splice variants of the cell surface glycoprotein CD44 associated with metastatic tumour cells are expressed in normal tissues of humans and cynomolgus monkeys," *European Journal of Cancer*, vol. 31, no. 13-14, pp. 2385–2391, 1995.

[69] J. W. Stroomer, J. C. Roos, M. Sproll et al., "Safety and biodistribution of 99mTechnetium-labeled anti-CD44v6 monoclonal antibody BIWA 1 in head and neck cancer patients," *Clinical Cancer Research*, vol. 6, no. 8, pp. 3046–3055, 2000.

[70] D. R. Colnot, J. C. Roos, R. de Bree et al., "Safety, biodistribution, pharmacokinetics, and immunogenicity of ^{99m}Tc-labeled humanized monoclonal antibody BIWA 4 (bivatuzumab) in patients with squamous cell carcinoma of the head and neck," *Cancer Immunology, Immunotherapy*, vol. 52, no. 9, pp. 576–582, 2003.

[71] P. K. Borjesson, E. J. Postema, J. C. Roos et al., "Phase I therapy study with (186)Re-labeled humanized monoclonal antibody BIWA 4 (bivatuzumab) in patients with head and neck squamous cell carcinoma," *Clinical Cancer Research*, vol. 9, no. 10, part 2, pp. 3961S–3972S, 2003.

[72] E. J. Postema, P. K. Borjesson, W. C. Buijs et al., "Dosimetric analysis of radioimmunotherapy with 186Re-labeled bivatuzumab in patients with head and neck cancer," *Journal of Nuclear Medicine*, vol. 44, no. 10, pp. 1690–1699, 2003.

[73] M. Koppe, F. van Schaijk, J. Roos et al., "Safety, pharmacokinetics, immunogenicity, and biodistribution of 186Re-labeled humanized monoclonal antibody BIWA 4 (Bivatuzumab) in patients with early-stage breast cancer," *Cancer Biotherapy and Radiopharmaceuticals*, vol. 19, no. 6, pp. 720–729, 2004.

[74] B. M. Tijink, J. Buter, R. de Bree et al., "A phase I dose escalation study with anti-CD44v6 bivatuzumab mertansine in patients with incurable squamous cell carcinoma of the head and neck or esophagus," *Clinical Cancer Research*, vol. 12, no. 20, part 1, pp. 6064–6072, 2006.

[75] A. Sauter, C. Kloft, S. Gronau, F. Bogeschdorfer et al., "Pharmacokinetics , immunogenicity and safety of bivatuzumab mertansine, a novel CD44v6-targeting immunoconjugate, in patients with squamous cell carcinoma of the head and neck," *International Journal of Oncology*, vol. 30, no. 4, pp. 927–935, 2007.

[76] H. Riechelmann, A. Sauter, W. Golze et al., "Phase I trial with the CD44v6-targeting immunoconjugate bivatuzumab mertansine in head and neck squamous cell carcinoma," *Oral Oncology*, vol. 44, no. 9, pp. 823–829, 2008.

[77] K. Gurtner, F. Hessel, W. Eicheler et al., "Combined treatment of the immunoconjugate bivatuzumab mertansine and fractionated irradiation improves local tumour control in vivo," *Radiotherapy and Oncology*, vol. 102, no. 3, pp. 444–449, 2012.

[78] C. A. Boswell and M. W. Brechbiel, "Development of radioimmunotherapeutic and diagnostic antibodies: an inside-out view," *Nuclear Medicine and Biology*, vol. 34, no. 7, pp. 757–778, 2007.

[79] P. J. Carter, "Potent antibody therapeutics by design," *Nature Reviews Immunology*, vol. 6, no. 5, pp. 343–357, 2006.

[80] A. Nelson, E. Dhimolea, and J. M. Reichert, "Development trends for human monoclonal antibody therapeutics," *Nature Reviews Drug Discovery*, vol. 9, no. 10, pp. 767–774, 2010.

[81] J. M. Reichert, "Antibodies to watch in 2017," *mAbs*, vol. 9, no. 2, pp. 167–181, 2016.

[82] J. M. Reichert, "Antibodies to watch in 2017," *mAbs*, vol. 9, no. 2, pp. 167–181, 2017.

[83] A. L. Nelson, "Antibody fragments: hope and hype," *mAbs*, vol. 2, no. 1, pp. 77–83, 2010.

[84] D. Y. Kim, G. Hussack, H. Kandalaft, and J. Tanha, "Mutational approaches to improve the biophysical properties of human single-domain antibodies," *Biochimica et Biophysica Acta—Proteins and Proteomics*, vol. 1844, no. 11, pp. 1983–2001, 2014.

[85] J. Nilvebrant, P. M. Tessier, and S. S. Sidhu, "Engineered autonomous human variable domains," *Current Pharmaceutical Design*, vol. 22, no. 43, pp. 6527–6537, 2016.

[86] T. Ying, R. Gong, T. W. Ju, P. Prabakaran, and D. S. Dimitrov, "Engineered Fc based antibody domains and fragments as novel scaffolds," *Biochimica et Biophysica Acta—Proteins and Proteomics*, vol. 1844, no. 11, pp. 1977–1982, 2014.

[87] T. Ying, Y. Wang, Y. Feng et al., "Engineered antibody domains with significantly increased transcytosis and half-life in macaques mediated by FcRn," *mAbs*, vol. 7, no. 5, pp. 922–930, 2015.

[88] C. Spiess, Q. Zhai, and P. J. Carter, "Alternative molecular formats and therapeutic applications for bispecific antibodies," *Molecular Immunology*, vol. 67, no. 2, part A, pp. 95–106, 2015.

[89] J. Prassler, S. Thiel, C. Pracht et al., "HuCAL PLATINUM, a synthetic fab library optimized for sequence diversity and superior performance in mammalian expression systems," *Journal of Molecular Biology*, vol. 413, no. 1, pp. 261–278, 2011.

[90] A.-K. Haylock, D. Spiegelberg, J. Nilvebrant, K. Sandström, and M. Nestor, "In vivo characterization of the novel CD44v6-targeting Fab fragment AbD15179 for molecular imaging of squamous cell carcinoma: A dual-isotope study," *EJNMMI Research*, vol. 4, no. 1, pp. 1–13, 2014.

[91] J. Stenberg, D. Spiegelberg, H. Karlsson, and M. Nestor, "Choice of labeling and cell line influences interactions between the Fab fragment AbD15179 and its target antigen CD44v6," *Nuclear Medicine and Biology*, vol. 41, no. 2, pp. 140–147, 2014.

[92] A.-K. Haylock, D. Spiegelberg, A. C. Mortensen et al., "Evaluation of a novel type of imaging probe based on a recombinant bivalent mini-antibody construct for detection of CD44v6-expressing squamous cell carcinoma," *International Journal of Oncology*, vol. 48, no. 2, pp. 461–470, 2016.

[93] M. H. Jeoung, T.-K. Kim, H. Shim, and S. Lee, "Development of a sandwich enzyme-linked immunosorbent assay for the detection of CD44v3 using exon v3- and v6-specific monoclonal antibody pairs," *Journal of Immunological Methods*, vol. 436, pp. 22–28, 2016.

[94] Y. Chen, K. Huang, X. Li, X. Lin, Z. Zhu, and Y. Wu, "Generation of a stable anti-human CD44v6 scFv and analysis of its cancer-targeting ability in vitro," *Cancer Immunology, Immunotherapy*, vol. 59, no. 6, pp. 933–942, 2010.

[95] S. Zarei, A. A. Bayat, R. Hadavi et al., "Production and Characterization of a Peptide-based Monoclonal Antibody Against

CD44 Variant 6," *Monoclonal Antibodies in Immunodiagnosis and Immunotherapy*, vol. 34, no. 1, pp. 36–43, 2015.

[96] I. Morath, T. N. Hartmann, and V. Orian-Rousseau, "CD44: More than a mere stem cell marker," *International Journal of Biochemistry and Cell Biology*, vol. 81, pp. 166–173, 2016.

[97] D. Naor, R. V. Sionov, and D. Ish-Shalom, "CD44: structure, function, and association with the malignant process," *Advances in Cancer Research*, vol. 71, pp. 241–319, 1997.

[98] V. Orian-Rousseau, L. Chen, J. P. Sleeman, P. Herrlich, and H. Ponta, "CD44 is required for two consecutive steps in HGF/c-Met signaling," *Genes and Development*, vol. 16, no. 23, pp. 3074–3086, 2002.

[99] H. Ponta and P. Herrlich, "The CD44 protein family: roles in embryogenesis and tumor progression," *Frontiers in Bioscience*, vol. 3, pp. 650–656, 1998.

[100] A. Matzke, P. Herrlich, H. Ponta, and V. Orian-Rousseau, "A five-amino-acid peptide blocks Met- and Ron-dependent cell migration," *Cancer Research*, vol. 65, no. 14, pp. 6105–6110, 2005.

Hindawi
Contrast Media & Molecular Imaging
Volume 2017, Article ID 8639731, 6 pages
https://doi.org/10.1155/2017/8639731

Research Article

Hepatic 18F-FDG Uptake Measurements on PET/MR: Impact of Volume of Interest Location on Repeatability

Liran Domachevsky,[1,2] Hanna Bernstine,[1,2] Meital Nidam,[1,2] Dan Stein,[1,2] Natalia Goldberg,[1,2] Dorit Stern,[1,2] Ifat Abadi-Korek,[1,2] and David Groshar[1,2]

[1]*Department of Nuclear Medicine, Assuta Medical Centers, Tel Aviv, Israel*
[2]*Sackler Faculty of Medicine, Tel Aviv University, Tel Aviv, Israel*

Correspondence should be addressed to Liran Domachevsky; liranura@gmail.com

Received 5 January 2017; Revised 9 April 2017; Accepted 26 April 2017; Published 30 May 2017

Academic Editor: Xuelei Ma

Background. To investigate same day 18F-FDG (Fluorodeoxyglucose) PET (Positron Emission Tomography)/MR (Magnetic Resonance) test-retest repeatability of Standardized Uptake Value measurements normalized for body weight (SUV) and lean body mass (SUL) in different locations in the liver. *Methods*. This prospective study was IRB approved with written informed consent obtained. 35 patients (20 women and 15 men, 61 ± 11.2 years) that performed a whole-body 18F-FDG PET/MR followed by liver-dedicated contrast-enhanced 18F-FDG PET/MR were included. SUV/L max, mean, and peak were measured inferior to, superior to, and at the right portal vein and in the left lobe of the liver. The coefficient of variation (CV) and intraclass correlation coefficient (ICC) were calculated and Bland-Altman plots were obtained. *Results*. The variability for SUV/L's measurements was lowest inferior to the portal vein (<9.2%) followed by measurements performed at the level of the portal vein (<14.6%). *Conclusion*. The area inferior to the portal vein is the most reliable location for hepatic 18F-FDG uptake measurements on PET/MR.

1. Introduction

Tumoral FDG (Fluorodeoxyglucose) uptake reflects the metabolic activity of the tumor and is mainly used to evaluate tumor aggressiveness on baseline studies and to assess the response to treatment and prognosis based on interval changes of FDG uptake during and after treatment.

FDG uptake can be assessed either semiquantitatively or qualitatively. Semiquantitative assessment uses the Standardized Uptake Value (SUV) variable that can be used as a standalone variable or as a tumor to background ratio. Qualitative assessment is based on visual comparison of tumor uptake with tissues having different levels of FDG uptake. With either method of FDG uptake evaluation, the assumption is that background FDG uptake is reliable which is important for sequential studies of a single patient and between different patient groups.

It is therefore crucial to know FDG uptake variability of normal tissues in order to recognize changes that reside within the variability range and to rule out systemic errors that might occur whenever outside the range differences in variability are found.

In clinical practice, mainly for lymphoma, blood pool (e.g., mediastinum) and liver SUV measurements are frequently used in PET (Positron Emission Tomography)/CT (Computed Tomography) as background since these tissues have adequate test-retest repeatability [1].

In addition, given their different mean SUV measurements, a graded visual scale has been developed with two reference points (i.e., mediastinum and liver) instead of one, better reflecting the continuous nature of FDG uptake resulting in better stratification of the response to treatment [2].

As of now, test-retest repeatability of FDG uptake in the liver has been evaluated only with PET/CT [3]. Several studies used one area to measure FDG uptake while others used different areas within the liver. To the best of our knowledge, at present, no study has investigated which area of the liver has the most reliable SUV measurements on PET/MR (Magnetic Resonance).

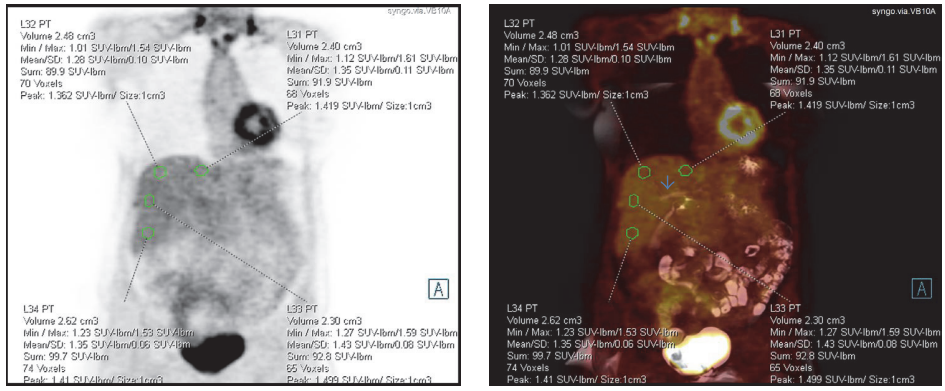

(a) (b)

Figure 1: (a) Coronal PET attenuation correction image with spheres located inferior to, superior to, and at the level of the portal vein as well as in the left lobe of the liver. (b) Coronal fused T2-weighted HASTE FS PET/MR image demonstrating the spheres related to the portal vein (arrow).

The purpose of the current study is therefore to evaluate the test-retest repeatability of different SUV measurements normalized for body weight (SUV) and lean body mass (SUL) in different locations in the liver using PET/MR.

2. Methods

2.1. Subjects. This prospective study has been approved by the institutional review board. All subjects signed an informed consent form. Between September 2015 and March 2017, consecutive patients who performed whole-body nonenhanced 18F-FDG PET/MR followed by contrast-enhanced 18F-FDG PET/MR centered at the liver were enrolled. All patients performed 18F-FDG PET/CT prior to the 18F-FDG PET/MR.

2.2. PET/MR Protocol. 18F-FDG PET/MR was performed from skull base to mid-thigh on the Biograph mMR (Siemens AG, healthcare sector, Erlangen, Germany) simultaneous PET/MR system. 18F-FDG injection dose was 5.18 MBq/kg.

Patients were positioned in a supine position and multistep/multibed scanning was performed in caudocranial direction with four bed positions. We used a 24-channel spine RF coil integrated within the MR bed and 3 surface body coils (6 channel each) to cover the thorax, abdomen, and pelvis. For the neck we used a 16-channel RF head/neck coil.

PET data was acquired in the list mode with the following reconstruction parameters: high definition PET +ordered subset expectation maximization (OSEM) iterative algorithm, three iterations and 21 subsets, and Gaussian filter: FWHM 4 mm; relative scattered correction.

For the nonenhanced scan each bed position was started with coronal Dixon-based sequences for MR attenuation correction (MRAC) (breath holding) (19 sec). This was followed by axial T2 HASTE (free breathing) (36 sec), coronal T2 HASTE with fat suppression (FS) (Inversion recovery-(IR-) based) (44 sec), and axial T1 VIBE Dixon (breath holding) (20 sec). PET data was acquired simultaneously with acquisition time of 5 minutes for each bed position.

These sequences were followed immediately by a liver-dedicated contrast-enhanced scan using Gadoteric acid (Dotarem®, Guerbet, France) (0.2 ml/kg, 0.1 mmol/kg at 1-2 ml/s, 20 ml saline flush) centered at the liver with the following parameters: Coronal Dixon-based sequences for MR attenuation correction (MRAC) (breath holding) (19 sec); nonenhanced Axial VIBE FS (breath holding) (18 sec) followed by three contrast-enhanced Axial VIBE FS (breath holding) each lasting 18 sec with 20 sec gap between scans. This was followed by a coronal 2D FLASH FS (breath holding) (18 sec) and late contrast-enhanced Axial VIBE FS (breath holding) (18 sec). PET data was again acquired simultaneously with acquisition time of 5 minutes.

SUV and SUL (mean, max, and peak) were measured using a sphere volume of interest (VOI) ranging between 2 and 3 ml (Figure 1). SUV/L max is a single-pixel value of the maximal SUV/L within the sphere, whereas SUV/L peak is the mean SUV/L within a predetermined volume of interest (VOI) of 1 ml around the voxel with the highest SUV/L in the sphere [4]. SUV/L mean is the average SUV/L value within the sphere.

Normalization for BW (body weight) was performed using the patient weight in kg, measured before 18F-FDG injection, and for LBM (lean body mass) using the following formula:

$$\begin{aligned} \text{LBM (female)} &= (1.07 \times \text{BW})\ (\text{kg}) \\ &\quad - 148\left[\frac{\text{BW (kg)}}{\text{body height (cm)}}\right]^2, \\ \text{LBM (male)} &= (1.1 \times \text{BW})\ (\text{kg}) \\ &\quad - 120\left[\frac{\text{BW (kg)}}{\text{body height (cm)}}\right]^2. \end{aligned} \tag{1}$$

2.3. Image Analysis. We used dedicated software for SUV/L calculations (Syngo.via; Siemens AG, healthcare sector, Erlangen, Germany). A sphere VOI was drawn in four areas

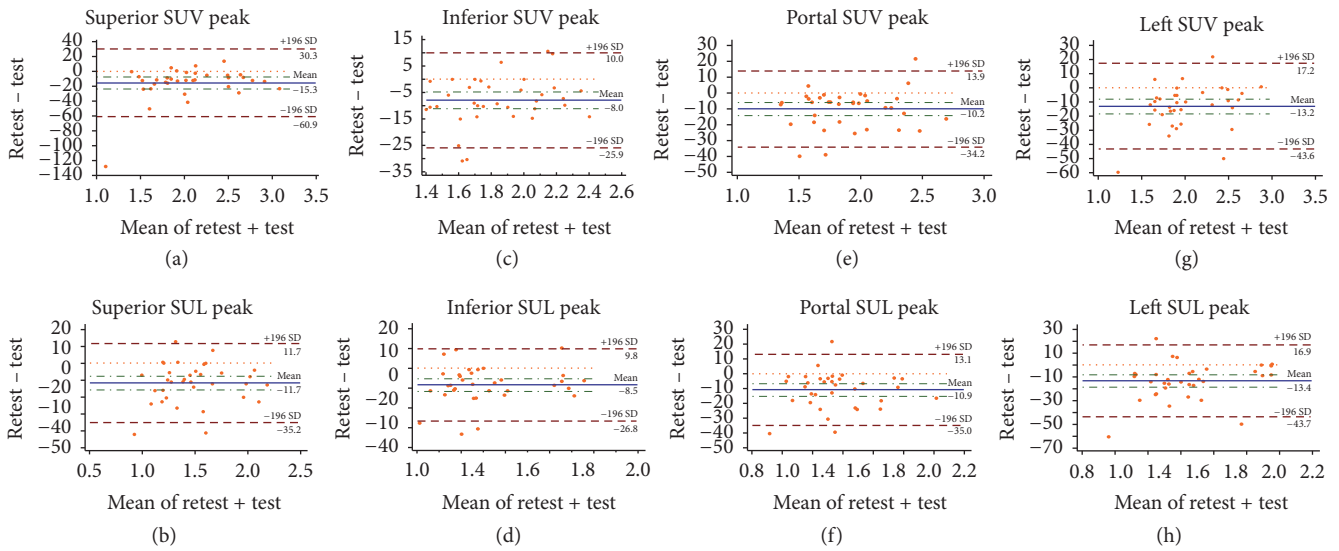

FIGURE 2: Bland-Altman plots of difference versus mean of SUV peak between retest and test in the superior (a, b), inferior (c, d), portal (e, f), and left (g, h) areas of the liver normalized to BW (a, c, e, g) and LBM (b, d, f, h). SUV: Standardized Uptake Value measurements normalized for body weight. SUL: Standardized Uptake Value measurements normalized for lean body mass.

in the liver parenchyma: superior to, inferior to, and at the level of the portal vein and in the left lobe of the liver. The sphere was located on PET attenuation correction images of the whole-body PET/MR scan and on the PET attenuation correction images of the liver-dedicated scan after verifying the corresponding exact location and the lack of abnormalities in this area on all MR sequences (Figure 1). All measurements were conducted by a dual board-certified in radiology and nuclear medicine physician (L. D., with 3 years of experience).

2.4. Statistics. MedCalc (16.2.0) was used for all statistical analyses. Mean differences of the various SUVs/Ls between test and retest were calculated.

The coefficient of variation (CV) was calculated using the following formula:

$$\text{CV } (\%) = 100 \times \frac{\text{SD}}{\text{mean}}, \quad (2)$$

where $\text{SD} = \sqrt{\sum (X_1 - X_2)^2 / 2N}$ (within-patient variation), X_1 and X_2 represent test and retest measurements, and N denotes the number of patients.

The intraclass correlation coefficient (ICC) was used to estimate the absolute agreement among measurements to compensate for systematic differences. ICC was interpreted as follows: 0–0.2 indicated poor agreement; 0.21–0.4 indicates fair agreement; 0.41–0.6 indicates moderate agreement; 0.61–0.80 indicates good agreement; and > 0.80 indicates very good agreement. Bland-Altman plots were obtained to assess the metrics differences between test and retest.

3. Results

35 patients (20 women and 15 men, 61 ± 11.2 years) with cancer (Gastrointestinal: 16, genitourinary: 6, breast: 9, lymphoma: 3, and melanoma: 1) without conspicuous liver metastases or steatosis on CT and on the MR part of the study were enrolled. The 18F-FDG uptake period was 83 ± 15 minutes.

Test-retest mean differences for the various SUV/L in the different regions of the liver are presented on Bland-Altman plots (Figure 2) and are shown in Table 1.

CV values of the various SUVs/Ls were always lower when measured inferior to the portal vein followed by measurements performed at the level of the portal vein. The highest CV's is seen superior to the portal vein and at the level of the left lobe of the liver (Table 2).

Very good agreement was found for SUV/L mean, SUV/L peak, and SUV max measured in the region inferior to the portal vein and for SUV/L mean and SUL peak in the region superior to the portal vein and in SUL mean in the region of the portal vein. Absolute agreement was always higher for SUV/L mean followed by SUV/L peak and SUV/L max. SUL measurements always had better agreement compared to SUV measurements except for the area inferior to the portal vein in which SUV max demonstrated very good agreement compared to good agreement in SUL max (Table 2).

4. Discussion

The present study demonstrates that the area inferior to the portal vein is the most reliable location in the liver and might be the best region to be used as background for the evaluation of tumor to liver background on PET/MR.

FDG uptake can be assessed either quantitatively or qualitatively. As absolute quantitation is cumbersome and not practical in clinics, semiquantitative methods expressed as a single numeric Standardized Uptake Value (SUV) have been increasingly used for evaluating cancer patients. Standardization of SUV is crucial as this value is affected by several

Table 1: SUV and SUL max, mean, and peak and paired difference with standard deviation measurements superior to, inferior to, and at the level of the portal vein and left lobe of the liver in first (test) and second (retest) scans.

	Superior	Inferior	Portal	Left
SUV max test	2.52 ± 0.53	2.1 ± 0.31	2.24 ± 0.44	2.47 ± 0.47
SUV max retest	2.21 ± 0.55	1.97 ± 0.38	1.99 ± 0.40	2.12 ± 0.51
Paired difference	0.31 ± 0.45	0.14 ± 0.21	0.26 ± 0.36	0.35 ± 0.48
SUV mean test	1.95 ± 0.41	1.76 ± 0.26	1.83 ± 0.33	1.92 ± 0.35
SUV mean retest	1.77 ± 0.46	1.62 ± 0.29	1.65 ± 0.32	1.7 ± 0.41
Paired difference	0.18 ± 0.26	0.14 ± 0.14	0.18 ± 0.2	0.21 ± 0.26
SUV peak test	2.19 ± 0.48	1.92 ± 0.28	1.99 ± 0.37	2.15 ± 0.4
SUV peak retest	1.9 ± 0.51	1.78 ± 0.3	1.8 ± 0.36	1.9 ± 0.42
Paired difference	0.28 ± 0.33	0.14 ± 0.16	0.19 ± 0.24	0.25 ± 0.3
SUL max test	1.79 ± 0.4	1.45 ± 0.23	1.6 ± 0.31	1.74 ± 0.32
SUL max retest	1.58 ± 0.34	1.34 ± 0.25	1.42 ± 0.27	1.5 ± 0.34
Paired difference	0.21 ± 0.33	0.10 ± 0.16	0.18 ± 0.23	0.24 ± 0.3
SUL mean test	1.4 ± 0.3	1.26 ± 0.2	1.3 ± 0.23	1.37 ± 0.25
SUL mean retest	1.26 ± 0.31	1.16 ± 0.21	1.18 ± 0.22	1.22 ± 0.29
Paired difference	0.14 ± 0.15	0.1 ± 0.1	0.19 ± 0.13	0.15 ± 0.17
SUL peak test	1.56 ± 0.35	1.37 ± 0.2	1.43 ± 0.26	1.54 ± 0.28
SUL peak retest	1.4 ± 0.32	1.26 ± 0.21	1.28 ± 0.24	1.35 ± 0. 3
Paired difference	0.17 ± 0.17	0.11 ± 0.12	0.15 ± 0.16	0.18 ± 0.21

Table 2: SUV and SUL: CV and ICC from duplicate measurements superior to, inferior to, and at the level of the portal vein and in the left lobe of the liver.

	SUV max		SUV peak		SUV mean		SUL max		SUL peak		SUL mean	
	ICC	CV%	ICC	CV%	ICC	CV%	ICC	CV%	ICC	CV%	ICC	CV%
Superior	0.59	17.1	0.78	14.6	0.82	11.9	0.63	16.4	0.87	11.4	0.89	10.8
Inferior	0.83	8.5	0.84	8.2	0.87	8.2	0.78	9.2	0.85	8.5	0.89	8.2
Portal	0.64	14.6	0.78	11.3	0.81	10.7	0.68	13.7	0.79	11.3	0.82	10.1
Left	0.52	18.3	0.73	13.5	0.77	12.8	0.59	16.3	0.74	13.5	0.79	12.4

factors and is usually performed with a tight control of the various factors that affect SUV measurements or by using a ratio of tumor to background FDG uptake. Normal liver and blood pool (e.g., mediastinum) SUV are usually used on FDG PET/CT studies as background tissues given their high degree of repeatability. Qualitative assessment is based on visual comparison of FDG uptake in tumors with that of a single or several background tissues.

A basic requisite to any of the aforementioned methods of FDG uptake assessment is the test-retest reliability and variability of background tissues. Whenever a test-retest variability range is defined, each follow-up scan is evaluated accordingly. If changes fall in the variability range, the scan is deemed adequate and any change in tumoral FDG uptake is considered a true change and needs to be further assessed to determine its clinical significance. On the contrary, if changes are above the defined range, a search for systematic errors has to be performed and the study interpretation has to be made in the light of and with the understanding of these factors.

Several studies have investigated 18F-FDG PET/CT test-retest variability of SUV/L measurements in the liver. Boktor et al. [5] have found that test-retest variation in liver mean SUV has a mean of 0.12 ± 0.5 with a reference range of −0.9 to 1.1. They used a two-dimensional region of interest (ROI) located in the right lobe of the liver "well away from diaphragmatic motion artifacts". Tahari et al. [3] found intrapatient variation in liver mean SUL in the range of −0.5 to 0.6. They found an average absolute test-retest difference of 0.03 ± 0.27 and ICC of 0.35–0.41, 0.37–0.38, and 0.38–0.44 superior to, at the level of, and inferior to the portal vein, respectively. Paquet et al. [6] revealed an absolute difference of 0.05 ± 0.2 and 0.05 ± 0.3 for SUL mean and SUV mean, respectively, and 0.08 ± 0.33 and 0.09 ± 0.48 for SUL max and SUV max, respectively. Only maximal SUL was statistically different between studies ($p < 0.05$). Absolute agreement (ICC) of 0.57, 0.65, 0.65, and 0.7 and CV (%) of 10.8, 12.4, 11, and 12.6 was found for mean and maximal SUL and SUV, respectively. In their study, ROI was placed in a central region in the right lobe of the liver.

To the best of our knowledge, this is the first study to investigate different SUVs and SULs measurements in different locations in the liver on 18F-FDG PET/MR. As a new modality 18F PET/MR test-retest reliability with regard to SUV/L measurements is needed. Principal factors that

differ between 18F-FDG PET/CT and 18F-FDG PET/MR that might affect reliability include Dixon-based attenuation correction maps, scanning time, and MR hardware that is located in proximity to PET detectors. This has led us to determine "inherent" variation range in liver FDG uptake between studies. For instance, using the average SUV peak inferior to the portal vein, the difference in SUV between studies is −0.14; therefore if we use the 95% CI an expected range between studies is +0.27 to −0.54. This range should be taken into consideration when interpreting serial 18F-FDG PET/MR studies.

Unlike 18F-FDG PET/CT repeatability studies that showed better repeatability with SULs [7, 8], we found that SUVs showed slightly less variability and similar agreement compared to SULs measurements in the area inferior to the portal vein (8.2% and 0.84 versus 8.5% and 0.85, resp.). A very good agreement was found for SUV/L mean, SUV/L peak, and SUV max in that region. Furthermore, in general, SUV/L mean had better agreement than SUV/L peak followed by SUV/L max. This is reasonable as averaging of SUV measurements is less prone to outliner values that influence correlation. With regard to absolute variation we found that the most consistent measurements are found inferior to the portal vein followed by the area at the level of the portal vein with the least repeatable measurements seen superior to the portal vein and in the left lobe. This distribution might be explained by breathing effect on measurements that are more pronounced closer to the diaphragm and were exacerbated by difference in breathing instructions between the first and second scan. We find this interesting in light of Viner et al. [9] study results with FDG PET/CT in which the area superior to the portal vein demonstrated the highest interreader agreement regarding SUL mean, a finding that was further supported by Tahari et al. [3]. Furthermore, the area superior to the portal vein is now recommended as the preferred area to measure liver FDG uptake on PET/CT [10]. However, both studies evaluated only interreader agreement for the same time study and not repeatability for sequential studies.

Our study has several limitations. First, the number of patients is relatively small. Second, the time interval between test and retest measurements does not reflect "reality" where the time interval is much longer usually in the range of several weeks to months. On the other hand, since a low variability on liver FDG uptake has been shown with PET/CT, this might be of benefit as it evaluates PET/MR scanner performance with basically zero to minimal effect of factors that are seen in longer interval that influence reliability like changes in body habitus, changes in liver texture as a result of therapy, and so forth. Third, because the second study has focused on the liver with the addition of contrast injection, breathing instructions differed accordingly with potential effect on SUV/L measurements. It could have been better to use the same breath holding technique to evaluate the test-retest repeatability. Even so, our variability results in the area inferior to the portal vein are similar to previous reports on repeatability of PET/CT FDG uptake in the liver [1] with a CV around 10%, supporting this area as the most reliable even with different breath instructions.

In conclusion, the least variability of SUV/L measurements in the liver was demonstrated inferior to the portal vein, suggesting that this location may serve as the preferred area for background comparison on follow-up studies. Further studies are warranted to validate whether the use of other areas, especially at the portal vein area, would make any relevant differences in clinical practice.

Disclosure

An earlier version of this work was presented as an abstract at RSNA 2016 meeting central.

Conflicts of Interest

The authors declare that they have no conflicts of interest.

Authors' Contributions

Liran Domachevsky and Hanna Bernstine equally contributed to the manuscript.

References

[1] G. Kuhnert, R. Boellaard, S. Sterzer et al., "Impact of PET/CT image reconstruction methods and liver uptake normalization strategies on quantitative image analysis," *European Journal of Nuclear Medicine and Molecular Imaging*, vol. 43, no. 2, pp. 249–258, 2016.

[2] J. M. Zijlstra, C. N. Burggraaff, M. J. Kersten, and S. F. Barrington, "FDG-PET as a biomarker for early response in diffuse large B-cell lymphoma as well as in Hodgkin lymphoma? Ready for implementation in clinical practice?" *Haematologica*, vol. 101, no. 11, pp. 1279–1283, 2016.

[3] A. K. Tahari, V. Paidpally, A. Chirindet, R. L. Wahl, and R. M. Subramaniam, "Two-time-point FDG PET/CT: liver SULmean repeatability," *American Journal of Roentgenology*, vol. 204, no. 2, pp. 402–407, 2015.

[4] A. Sher, F. Lacoeuille, P. Fosse et al., "For avid glucose tumors, the SUV peak is the most reliable parameter for [18F]FDG-PET/CT quantification, regardless of acquisition time," *EJNMMI Research*, vol. 6, no. 1, article 21, 2016.

[5] R. R. Boktor, G. Walker, R. Stacey, S. Gledhill, and A. G. Pitman, "Reference range for intrapatient variability in blood-pool and liver SUV for 18F-FDG PET," *Journal of Nuclear Medicine*, vol. 54, no. 5, pp. 677–682, 2013.

[6] N. Paquet, A. Albert, J. Foidart, and R. Hustinx, "Within-patient variability of 18F-FDG: Standardized uptake values in normal tissues," *Journal of Nuclear Medicine*, vol. 45, no. 5, pp. 784–788, 2004.

[7] R. L. Wahl, H. Jacene, Y. Kasamon, and M. A. Lodge, "From RECIST to PERCIST: evolving considerations for PET response criteria in solid tumors," *Journal of Nuclear Medicine*, vol. 50, no. 1, 2009.

[8] J. K. Park, S. K. Kim, I. H. Cho, and E. J. Kong, "Measurement of SUVs-maximum for normal region using voi in PET/MRI and PET/CT," *The Scientific World Journal*, vol. 2014, Article ID 194925, 2014.

[9] M. Viner, G. Mercier, F. Hao, A. Malladi, and R. M. Subramaniam, "Liver SULmean at FDG PET/CT: Interreader agreement

and impact of placement of volume of interest," *Radiology*, vol. 267, no. 2, pp. 596–601, 2013.

[10] R. Boellaard, R. Delgado-Bolton, W. J. G. Oyen et al., "FDG PET/CT: EANM procedure guidelines for tumour imaging," *European Journal of Nuclear Medicine and Molecular Imaging*, vol. 42, version 2.0, pp. 328–354, 2015.

Hindawi
Contrast Media & Molecular Imaging
Volume 2017, Article ID 5260305, 7 pages
https://doi.org/10.1155/2017/5260305

Review Article

Advanced Functional Tumor Imaging and Precision Nuclear Medicine Enabled by Digital PET Technologies

Chadwick L. Wright, Katherine Binzel, Jun Zhang, and Michael V. Knopp

Wright Center of Innovation in Biomedical Imaging, Department of Radiology, The Ohio State University Wexner Medical Center, 395 W. 12th Avenue, Rm. 430, Columbus, OH 43210, USA

Correspondence should be addressed to Michael V. Knopp; knopp.16@osu.edu

Received 25 February 2017; Accepted 11 April 2017; Published 16 May 2017

Academic Editor: Shasha Li

The purpose of this article is to provide a brief overview of the background, basic principles, technological evolution, clinical capabilities, and future directions for functional tumor imaging as PET evolves from the conventional photomultiplier tube-based platform into a fully digital detector acquisition platform. The recent introduction of solid-state digital photon counting PET detector is the latest evolution of clinical PET which enables faster time-of-flight timing resolution that leads to more precise localization of the annihilation events and further contributes to reduction in partial volume and thus makes high definition and ultrahigh definition PET imaging feasible with current standard acquisition procedures. The technological advances of digital PET can be further leveraged by optimizing many of the acquisition and reconstruction methodologies to achieve faster image acquisition to improve cancer patient throughput, lower patient dose in accordance with ALARA, and improved quantitative accuracy to enable biomarker capability. Digital PET technology will advance molecular imaging capabilities beyond oncology and enable Precision Nuclear Medicine.

1. Introduction

The purpose of this article is to briefly introduce the current technological evolution that is enabled by digital detector technology and discuss its applicability to clinical positron emission tomography/computed tomography (PET/CT). Although PET/CT utilization has been primarily oncologic, functional molecular imaging has the opportunity for expanded utilization in both oncologic and nononcologic applications and will demand reduced ionizing radiotracer doses and improved quantification. The paradigm of Precision Nuclear Medicine incorporates new strategies to advance functional molecular imaging with more detailed visualization and more robust quantification of disease burden. These aspects are essential both for diagnostic and for therapy management opportunities including the further evolution as validated biomarkers. Even today, there are considerable unmet clinical needs such as the frequently observed indeterminate PET lesion, detectability of subcentimeter lesions, and lack of biomarker validation for response assessment. While many technologies have been rapidly moving away from cathode-ray tubes and analog signal processing, nuclear medicine and PET are still predominantly using the analog photomultiplier tube acquisition technologies. The recent introduction of solid-state detectors is a transformative technology change for clinical nuclear medicine. As with many other technology changes, solid-state and digital acquisition technologies can be implemented in different ways. One major driving force to pursue the replacement of the photomultiplier tube technology was the goal of integrated PET/magnetic resonance imaging (MRI) and next-generation PET/CT systems. While the acquisition chain consists of multiple components, especially the crystal characteristics, this article highlights the clinical opportunities enabled by this change of the detector technology. The most recent technology advance for PET/CT has been the clinical demonstration of a solid-state system which also has the best clinical system time-of-flight timing capabilities. This article summarizes our initial experiences

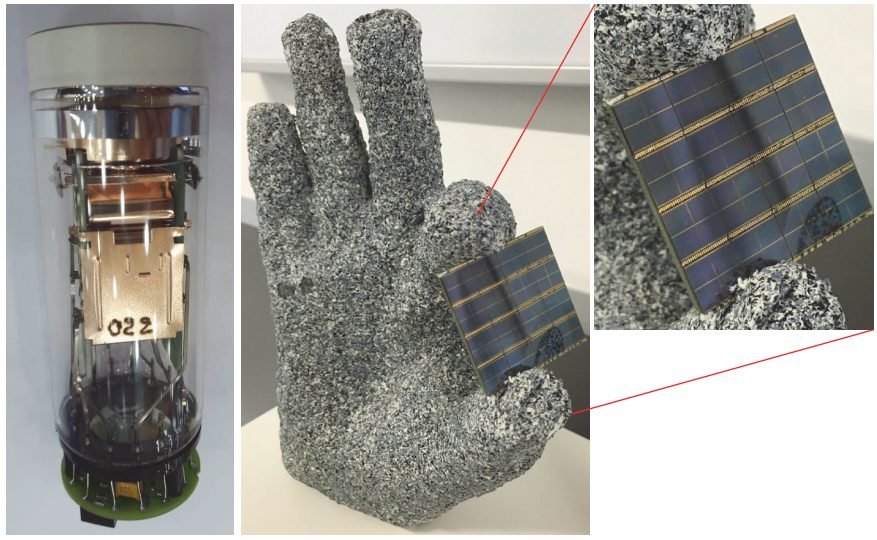

(a) (b) (c)

Figure 1: The photomultiplier tube detector unit from a cPET system (a) which has recently been replaced with a solid-state DPC PET detector unit (b) in the next-generation dPET/CT system. (c) A closer view of the DPC PET detector (Philips Healthcare, Cleveland, Ohio, USA). The DPC PET detector unit enables fully digital 1 : 1 coupling with the scintillation crystals within the dPET detector ring assembly.

with a focus on demonstrating the overall opportunities supported by next-generation digital PET technology.

2. Basic Principles of PET Detector Technology

Photomultiplier tube (PMT) detectors have been used since the early days of PET [1] and have not changed fundamentally except for manufacturing and timing improvements. As a PMT cannot operate within a strong magnetic field, solid-state avalanche photodiodes (APD) and silicon photomultipliers (SiPM) were developed to operate within such fields [2–4]. Initially, solid-state APD/SiPM detectors used analog signal processing approaches to translate photon detection into quantifiable annihilation events. The next leap in solid-state detectors was the introduction of digital photon counting (DPC) which eliminates any analog-to-digital conversion and thus enables preferential signal characteristics and speed [5]. Figure 1 shows a PMT unit from a conventional PET (cPET) system and the new DPC detector from digital PET (dPET) system. Combining these capabilities with direct one-to-one coupling to the unchanged detection crystals eliminates the need for Anger logic that was essential to estimate the localization of a photon event when the detector is significantly larger than the crystal to which it is coupled. Over the last 10 years, the timing resolution has become of increasing relevance as the benefits of time-of-flight (ToF) information for the more precise localization of the annihilation event in its linear trajectory led to improved lesion detectability [6]. While there are many other factors in the digital signal processing, this article will highlight the advancements of going from analog to solid-state digital processing and the potential applications for functional tumor imaging.

3. Clinical Evolution of PET Detector Technology

Whole-body PET became clinically feasible in the late 1980s and subsequently evolved from a 2D to a 3D multiring platform [1]. The next leap was the creation of a multimodal approach with the introduction of hybrid PET/CT systems around the change of the millennium. Later on in that decade, ToF became clinically available and further leveraged the 3D multiring platform [7]. Over the years, the z-axis coverage increased as a means of faster whole-body acquisition or larger organ coverage. While dynamic acquisitions were part of the early evolution of PET, it became unsupported during the focus of hybrid whole-body imaging but was rejuvenated in the last decade.

With the growth of MRI and the superb soft tissue contrast achievable, the vision of hybrid PET/MR systems rapidly evolved in the last decade [3, 4]. The facilitating technology for PET/MR was the availability of MRI-compatible APD/SiPM PET detectors which still relied upon Anger logic and analog signal processing just like the PMT-based systems that preceded it. One of the early limitations of this initial solid-state technology was the absence of ToF capability for clinical imaging. At present, current generation PET/MR systems support ToF timing resolution around 400 ps [8].

The initial lack of full digitization in the SiPM detectors led to the next technological leap with the introduction of digital photon counting (DPC) detector technology [5, 9–14]. Combining this with a direct one-to-one coupling streamlines the signal processing. This currently represents the most advanced dPET detector technology which has been introduced into the next-generation clinical dPET/CT [15–17] and preclinical dPET/MR [18, 19] systems.

4. Features of PET Systems

Here, we briefly present 7 features of clinical PET systems that are particularly relevant for understanding the clinical implications of new PET detector technologies [17].

4.1. Spatial Resolution. Spatial resolution of a PET scanner is an intrinsic feature of the detector chain which reflects the ability of the system to physically differentiate between two sources within the minimum distance between two points in a reconstructed image [1]. The physical size of the crystal element usually plays a dominant role in determining spatial resolution for PET. The fundamental limits for spatial resolution are also determined by contributions from positron range, noncollinearity, placement of detectors, decoding errors, systems noise, and reconstruction methodologies which may limit or degrade the effective resolution of the PET system [1, 20]. While these also apply to dPET systems, innovative designs such as one-to-one coupling significantly improved ToF timing resolution, and PSF-integrated reconstruction methodologies facilitate improvements [16]. In summary, dPET systems do not necessarily have improved physical spatial resolution, which is predominantly influenced by the crystal size; however, these systems contribute to improved clinical imaging characteristics due to the above advancements.

4.2. Sensitivity. Sensitivity of a PET system represents the ability to detect the true annihilation event rate. It is normally expressed in counts per unit time per unit of activity present in a source and depends on factors like solid angle, system photon detection efficiency, and dead time. Sensitivity in PET was substantially improved with the introduction of 3D acquisition; however, the sensitivity profile usually degrades from a peak in the center to both edges. In particular, 3D PET acquisitions have a rapid decrease in linear sensitivity due to poor counting statistics at the edges, thus requiring an overlap in longitudinal field of view between adjacent bed positions. Similarly, sensitivity decreases linearly within the axial field of view. An early observation and key advantage of the dPET detector technology is its virtually zero dead time, improving dPET system sensitivity [16]. This is particularly important for clinical studies which routinely administer radiotracer doses that generate count rates which exceed those used for typical PET scanner characterization (e.g., NEMA NU-2).

4.3. Noise Equivalent Count Rate (NECR). Image noise of a PET system is usually characterized by the NECR which is substantially improved with dPET systems [21]. In our initial experience with a precommercial release dPET/CT system, we observed 156% improvement at ~51 kBq/mL when compared with an existing PMT-based cPET system [17].

4.4. Image Acquisition. One goal to advance clinical nuclear medicine is to image faster and thus reduce patient motion, patient discomfort, table time, and the need for sedation/anesthesia [15]. One clinically relevant approach is to invest the gains of dPET detector sensitivity and precision into reducing the image acquisition time for static, whole-body, and dynamic dPET imaging. This potential for faster dPET image acquisition helps to minimize patient motion-based artifacts.

4.5. Image Reconstruction. Despite many technological advances in PET, today's clinical PET imaging reconstruction approaches utilize matrix sizes smaller than or equal to 200 and voxel lengths of 3-4 mm [22]. CT and MRI have increased their reconstruction matrix sizes due to improvements in signal generation which all led to advances in image quality. Therefore, dPET is poised to similarly embrace its ability to improve image reconstruction and visualization of more precisely detected annihilation events. This is a major area of opportunity to leverage dPET technology and therefore we have proposed refined nomenclature to characterize reconstructed PET images into *standard definition* (SD, matrix size $\leq$ 200), *high definition* (HD, matrix size > 200 but $\leq$ 400), and *ultrahigh definition* (UHD, matrix size > 400) [23]. Furthermore, HD and UHD image reconstruction utilizes PSF and Gaussian filtering as part of its overall optimization. These advances contribute to better visualization of the more precisely detected PET events [15, 17].

4.6. Time-of-Flight. The clinical benefit of ToF has been well recognized in the recent years [24]; however, the timing resolution of cPET systems was still limited to about 500 ps or greater [7, 25]. The dPET technologies facilitate substantially improved timing resolutions of 400 ps and better [8, 16, 17]. Ongoing clinical trials are evaluating whether this improvement in timing resolution may lead to improved lesion detectability and more precise quantification. The initial experience using a dPET/CT system with ToF capability of 325 ps indicates in phantoms that those expectations can be met and may lead to meaningful clinical improvements [15].

4.7. Radiotracer Dose. Another approach for better utilizing the higher sensitivity and precision of the dPET detector technology is to substantially reduce radiotracer dosing [15, 17, 21]. Radiation dose reduction is a key enabler to expand the clinical utilization of advanced functional molecular imaging methodologies like PET for clinical response assessment in patients undergoing therapeutic interventions as well as nononcologic clinical applications. This is another major area of opportunity to benefit from dPET technology and we have proposed refined nomenclature to characterize the PET dosing level for patients. Here is a proposed approach for ^{18}F-FDG oncologic whole-body PET imaging: *standard dose* (S_{DOSE}, ^{18}F-FDG $\geq$ 370 MBq but < 740 MBq), *low dose* (L_{DOSE}, ^{18}F-FDG $\geq$ 185 MBq but < 370 MBq), *ultralow dose* (UL_{DOSE}, ^{18}F-FDG $\geq$ 37 MBq but < 185 MBq), and *super-ultralow dose* (SUL_{DOSE}, ^{18}F-FDG < 37 MBq).

In summary, it has to be highlighted that the dPET technology enables the refinement of many different components that impact overall image quality, lesion detectability, and quantification.

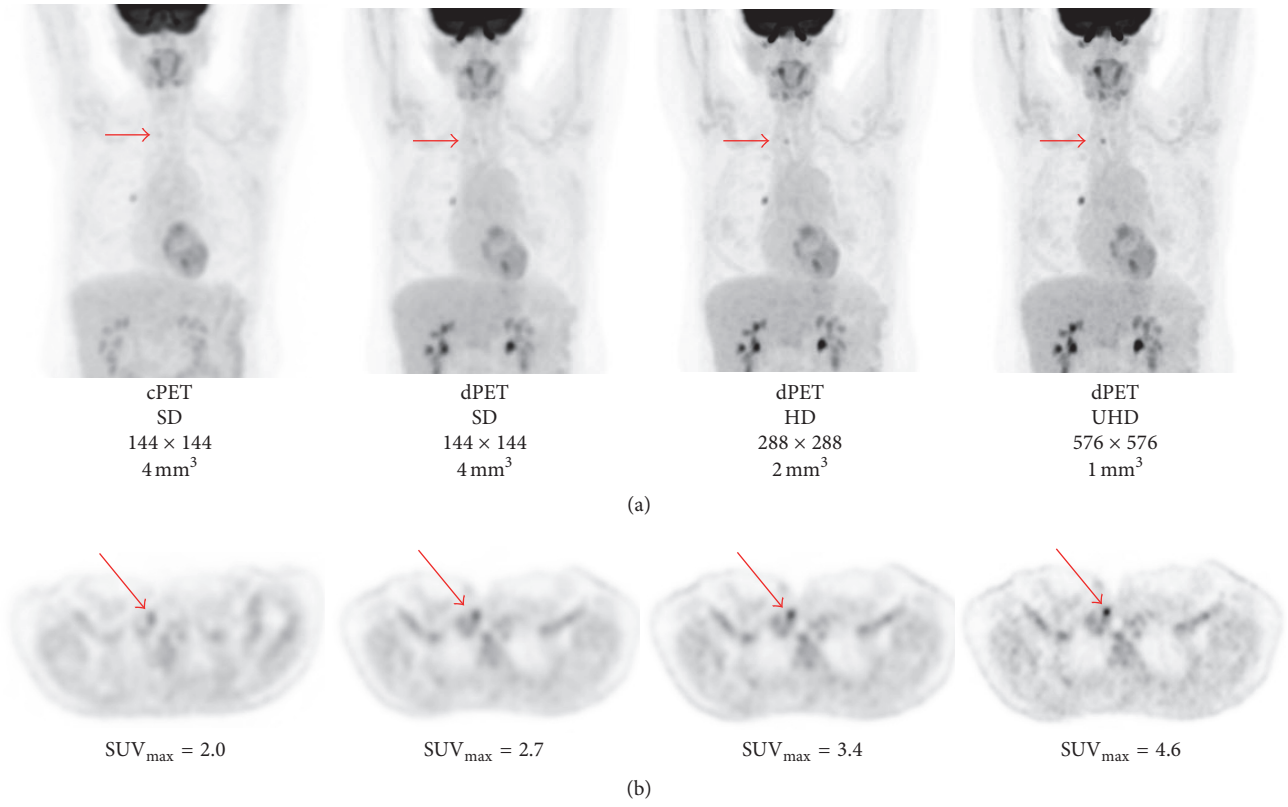

Figure 2: Intraindividual comparison in a patient scanned on the cPET/CT (Gemini 64 ToF, Philips Healthcare, Cleveland, Ohio, USA) system and a precommercial release dPET/CT (Vereos, Philips Healthcare, Cleveland, Ohio, USA) system using different reconstruction matrix/voxel volume sizes with a 3D line-of-response TOF blob-based algorithm [5, 17, 22, 23]. The patient was intravenously given a standard dose of 485 MBq of ^{18}F-FDG and then underwent imaging on the dPET/CT system at 50 min and the cPET/CT system at 76 min after injection. Both cPET and dPET emission scans were acquired with 90 s per bed position. Although there is a discrete ^{18}F-FDG-avid lesion noted in the right hilar region on both cPET and dPET images, there is a subcentimeter lesion in the right supraclavicular region which is only apparent on dPET images and becomes more conspicuous (and more suspicious) with higher definition image reconstructions. (a) Maximum intensity projection images from standard definition cPET (matrix size = 144 × 144, voxel volume = 4 mm^3), standard definition dPET (144 × 144, 4 mm^3), high definition dPET (288 × 288, 2 mm^3), and ultrahigh definition dPET (576 × 576, 1 mm^3). Point spread function and Gaussian filtering were applied to both high definition and ultrahigh definition dPET reconstructed images but not to standard definition dPET or cPET images. (b) Axial images from standard definition cPET, standard definition dPET, high definition dPET, and ultrahigh definition dPET taken at the level of the lesion in the right supraclavicular region. Region-of-interest analysis of the right supraclavicular lesion demonstrates FDG avidity similar to background on the cPET whereas the conspicuity and SUV_{max} values increase with higher definition dPET. This case illustrates the capability of dPET technology to substantially improve lesion detectability, lesion characterization, and diagnostic confidence.

5. Emerging Concepts for Functional Tumor Imaging Enabled by dPET

Our team has extensive experience performing more than 150 intraindividual comparison studies between dPET/CT and cPET/CT systems currently focusing on using standard of care, standard dose, and standard definition imaging [15]. The new dPET system technology has been performing well with consistent timing resolution better than 325 ps and excellent system stability for over 16 months [17].

5.1. Improved Lesion Detectability Enabled by Higher Definition Visualization. Digital PET has the ability to use larger reconstruction matrices with smaller voxel volumes which enables a more robust visualization of smaller metabolically active lesions. Currently, most cPET images are reconstructed using standard definition matrix sizes of 144–200. We anticipate that dPET imaging will routinely use high definition reconstruction with matrix sizes between 200 and 400 while using unchanged acquisition times. Initial results indicate that even ultrahigh definition imaging with matrix sizes greater than 400 can be readily accomplished for current whole-body imaging protocols leading to voxel volumes comparable to CT and/or MRI [15, 17]. Figure 2 illustrates the potential for improved lesion detectability enabled with dPET/CT using standard and higher definition reconstructions. Decreasing the voxel volume increases the visual conspicuity of lesions due to the substantially reduced partial volume and thus leads to higher definition image quality [22]. This improves lesion detectability without any apparent increase in background tissue uptake.

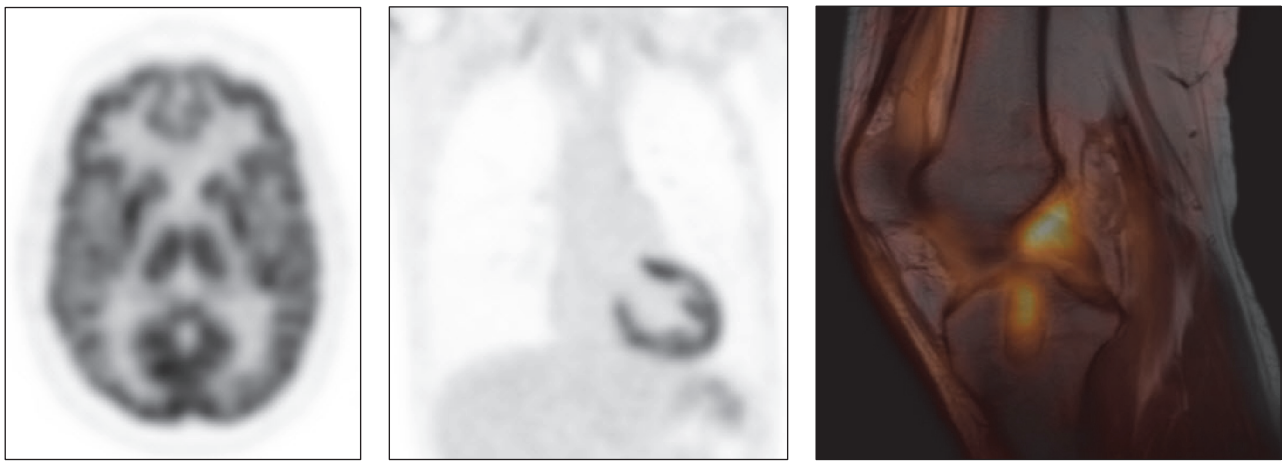

(a) (b) (c)

Figure 3: Nononcologic clinical opportunities for lower dose/higher definition imaging enabled by next-generation dPET include (a) neurologic, (b) cardiovascular, and (c) orthopedic/sports medicine indications. Digital PET cases demonstrated were imaged using standard ^{18}F-FDG doses of 448 MBq and 477 MBq for (a) and (b), respectively, and ultralow ^{18}F-FDG dose of 100 MBq for (c). The dPET acquisitions were obtained at 55 min after injection for (a), 53 min after injection for (b), and 60 min after injection for (c). The dPET emission scans were acquired with 90 s per bed position for (a) and (b) but (c) was a limited single bed acquisition for 15 min. Low dose CT attenuation scans were acquired using 120 kV and 50 mA with dose modulation and using iterative iDose^4 reconstruction.

5.2. Faster Image Acquisition and/or Lower Radiotracer Dose Imaging. Based on the improved sensitivity and precision of the dPET detector platform, there is potential for enabling faster whole-body PET image acquisitions [15]. With list-mode acquisition, the possibility exists for simulating shorter frame durations through data clipping. Our initial dPET observations indicate that a reduction of image acquisition times by more than 50% appears to be feasible without impacting image quality and/or quantification at current standard dosing levels for FDG. Alternatively, the capabilities of dPET can also be used to reduce radiotracer dose [21] while maintaining standard acquisition times. A combination which shortens acquisition time and reduces dose is also readily feasible, dependent upon individual imaging needs. In reality, dPET enables the opportunity to advance image quality, reduce acquisition time, and lower the dose compared to current standard-of-care PET approaches.

5.3. Improved Recovery Coefficient and Its Impact on Quantification. A well-established limitation of cPET is the deterioration of the recovery coefficient as lesion size decreases which weakens the quantitative precision for response assessment. This challenge not only affects small lesions but also affects quantitative precision when evaluating heterogeneous lesions. Although recovery coefficient and quantification are impacted by many components including detector characteristics, count density, timing resolution of ToF, and reconstruction approach, dPET technology has the potential to advance the quantitative precision for smaller and heterogeneous lesions in order to facilitate more consistency across multisite and multisystem clinical trials (e.g., EARL harmonization). It has been demonstrated that dPET has the highest overall system performance with consistently improved recovery coefficients when compared with cPET [17].

6. Future Directions

The current vision for the use of digital PET technology is either to implement it within hybrid MR systems or to improve the existing diagnostic/therapy management capabilities of PET/CT systems. It is our opinion that the DPC technology is truly the next generation in the evolution of PET imaging systems both as hybrid PET/CT and as PET/MR. The technological advances can be further leveraged by optimizing many of the PET acquisition and reconstruction methodologies to achieve disease-specific and organization-specific goals (e.g., faster image acquisition to improve patient throughput, lower patient dose in accordance with "as low as reasonably achievable" (ALARA), and improved quantitative accuracy to enable biomarker capability). PET image quality has not fundamentally changed over the last two decades and is poised to leap forward with high definition and even ultrahigh definition imaging. If we enable a substantial reduction in radiotracer dose, we have an opportunity to utilize PET more broadly in nononcologic applications (Figure 3) such as neuroscience, cardiovascular disease, sports medicine, and inflammation imaging. All of these benefits are very synergistic with the development of new PET radiotracers or new applications for existing radiotracers. The further evolution of clinical PET/MR will certainly benefit from the broader adoption of DPC detector technology as evidenced by the recent development of preclinical prototypes and our initial clinical evidence that dPET enables improved lesion detectability, lesion characterization, and diagnostic confidence.

7. Conclusion

This article highlights the fundamental technology innovations that led to the current development of next-generation digital PET systems. The wider clinical availability of dPET may be the inflection point to move clinical PET practice beyond oncology and into other nononcologic molecular imaging applications. In summary, digital PET is a transformative technology that will advance the paradigm of Precision Nuclear Medicine to address the unmet clinical needs for better tumor lesion detectability, improved lesion characterization especially for indeterminate lesions, more rapid biomarker validation for therapy response assessment, and radiotracer dose reduction in accordance with ALARA.

Abbreviations

^{18}F-FDG: Fluorine-18-fluorodeoxyglucose
ALARA: As low as reasonably achievable
APD: Avalanche photodiode
CT: Computed tomography
cPET: Conventional positron emission tomography
DPC: Digital photon counting
dPET: Digital positron emission tomography
FWHM: Full width half max
MR: Magnetic resonance
MRI: Magnetic resonance imaging
PET: Positron emission tomography
PMT: Photomultiplier tube
PSF: Point spread function
SiPM: Silicon photomultiplier.

Conflicts of Interest

The authors report no conflicts of interest regarding the publication of this paper.

Acknowledgments

Chadwick L. Wright is supported by (1) the American Cancer Society (Grant no. IRG-67-003-50) and (2) the National Institutes of Health (NIH)/National Cancer Institute (NCI), Clinical Loan Repayment Program. Chadwick L. Wright, Katherine Binzel, Jun Zhang, and Michael V. Knopp are also supported by the Wright Center of Innovation in Biomedical Imaging and Ohio ODSA TECH 09-028, TECH 10-012, and TECH 13-060 and the National Institutes of Health R01CA195513 and 5U24CA180803.

References

[1] A. M. J. Paans, "Positron emission tomography," *Acta Physica Polonica B*, vol. 30, no. 5, pp. 1619–1628, 1999.

[2] M. Ritzert, P. Fischer, V. Mlotok et al., "Compact SiPM based detector module for time-of-flight PET/MR," in *Proceedings of the 16th IEEE-NPSS Real Time Conference*, pp. 163–166, May 2009.

[3] M. S. Judenhofer, H. F. Wehrl, D. F. Newport et al., "Simultaneous PET-MRI: a new approach for functional and morphological imaging," *Nature Medicine*, vol. 14, no. 4, pp. 459–465, 2008.

[4] B. J. Pichler, M. S. Judenhofer, C. Catana et al., "Performance test of an LSO-APD detector in a 7-T MRI scanner for simultaneous PET/MRI," *Journal of Nuclear Medicine*, vol. 47, no. 4, pp. 639–647, 2006.

[5] T. Frach, G. Prescher, C. Degenhardt, R. De Gruyter, A. Schmitz, and R. Ballizany, "The digital silicon photomultiplier—principle of operation and intrinsic detector performance," in *Proceedings of the IEEE Nuclear Science Symposium Conference Record (NSS/MIC '09)*, pp. 1959–1965, October 2009.

[6] S. Surti and J. S. Karp, "Experimental evaluation of a simple lesion detection task with time-of-flight PET," *Physics in Medicine and Biology*, vol. 54, no. 2, pp. 373–384, 2009.

[7] S. Surti, A. Kuhn, M. E. Werner, A. E. Perkins, J. Kolthammer, and J. S. Karp, "Performance of Philips Gemini TF PET/CT scanner with special consideration for its time-of-flight imaging capabilities," *Journal of Nuclear Medicine*, vol. 48, no. 3, pp. 471–480, 2007.

[8] http://www3.gehealthcare.com/en/products/categories/magnetic_resonance_imaging/signa_pet-mr#tabs/tab2892C34FC72C-4A0497D37371F0D391EA.

[9] T. Frach and K. Fiedler, *Digital silicon photomultiplier for tof-pet*, U. S. P. a. T. Office, Koninklijke Philips Electronics N.V., Eindhoven, Netherlands, 2010.

[10] C. Degenhardt, G. Prescher, T. Frach et al., "The digital silicon photomultiplier—a novel sensor for the detection of scintillation light," in *Proceedings of the IEEE Nuclear Science Symposium Conference Record (NSS/MIC '09)*, pp. 2383–2386, October 2009.

[11] T. Frach, G. Prescher, C. Degenhardt, and B. Zwaans, "The digital silicon photomultiplier—system architecture and performance evaluation," in *Proceedings of the IEEE Nuclear Science Symposuim & Medical Imaging Conference (Nss/Mic '10)*, pp. 1722–1727, November 2010.

[12] C. Degenhardt, B. Zwaans, T. Frach, and R. De Gruyter, "Arrays of digital silicon photomultipliers—intrinsic performance and application to scintillator readout," in *Proceedings of the IEEE Nuclear Science Symposuim & Medical Imaging Conference (Nss/Mic '10)*, pp. 1954–1956, November 2010.

[13] C. Degenhardt, P. Rodrigues, A. Trindade et al., "Performance evaluation of a prototype Positron Emission Tomography scanner using digital photon counters (DPC)," in *Proceedings of the IEEE Nuclear Science Symposium and Medical Imaging Conference Record (NSS/MIC '12)*, pp. 2820–2824, November 2012.

[14] Y. Haemisch, T. Frach, C. Degenhardt, and A. Thon, "Fully digital arrays of silicon photomultipliers (dSiPM)—a scalable alternative to vacuum photomultiplier tubes (PMT)," in *Proceedings of the 2nd International Conference on Technology and Instrumentation in Particle Physics (Tipp '11)*, vol. 37, pp. 1546–1560, 2012.

[15] M. V. Knopp, K. Binzel, C. L. Wright et al., "Next generation digital detector PET/CT: what are the clinical opportunities?" in *Proceedings of the Radiological Society of North America Annual Meeting*, Chicago, Ill, USA, 2015.

[16] N. C. Nguyen, J. L. Vercher-Conejero, A. Sattar et al., "Image quality and diagnostic performance of a digital pet prototype in patients with oncologic diseases: initial experience and comparison with analog PET," *Journal of Nuclear Medicine*, vol. 56, no. 9, pp. 1378–1385, 2015.

[17] J. Zhang, K. Binzel, M. Miller et al., "Next generation digital detector PET/CT: the medical physics basis for the clinical applications," in *Proceedings of the Radiological Society of North America Annual Meeting*, Chicago, Ill, USA, 2015.

[18] B. Weissler, P. Gebhardt, P. M. Dueppenbecker et al., "A digital preclinical PET/MRI insert and initial results," *IEEE Transactions on Medical Imaging*, vol. 34, no. 11, pp. 2258–2270, 2015.

[19] D. Schug, J. Wehner, P. M. Dueppenbecker et al., "ToF performance evaluation of PET modules with digital silicon photomultiplier technology during MR operation," *IEEE Transactions on Nuclear Science*, vol. 62, no. 3, pp. 658–663, 2015.

[20] C. S. Levin and E. J. Hoffman, "Calculation of positron range and its effect on the fundamental limit of positron emission tomography system spatial resolution," *Physics in Medicine and Biology*, vol. 44, no. 3, pp. 781–799, 1999.

[21] M. A. Queiroz, G. Delso, S. Wollenweber et al., "Dose optimization in TOF-PET/MR compared to TOF-PET/CT," *PLoS ONE*, vol. 10, no. 7, Article ID e0128842, 2015.

[22] J. Zhang, K. Binzel, C. Wright et al., "Does reducing reconstruction voxel volume/increasing matrix size improve lesion detectability? a phantom and clinical feasibility demonstration using next generation digital PET/CT," *European Journal of Nuclear Medicine and Molecular Imaging*, vol. 42, pp. S51-S51, 2015.

[23] C. L. Wright, J. J. Maly, J. Zhang, and M. V. Knopp, "Advancing precision nuclear medicine and molecular imaging for lymphoma," *PET Clinics*, vol. 12, no. 1, pp. 63–82, 2017.

[24] G. El Fakhri, S. Surti, C. M. Trott, J. Scheuermann, and J. S. Karp, "Improvement in lesion detection with whole-body oncologic time-of-flight PET," *Journal of Nuclear Medicine*, vol. 52, no. 3, pp. 347–353, 2011.

[25] S. Surti and J. S. Karp, "Advances in time-of-flight PET," *Physica Medica*, vol. 32, no. 1, pp. 12–22, 2016.